STUDY OF ENGINEERED CEMENTITIOUS COMPOSITE USING MANUFACTURED SAND

Thesis Submitted for the Award of the Degree of

DOCTOR OF PHILOSOPHY
in
Civil Engineering

By

Sahil
Registration Number: 41800625

Supervised By

Dr. Pushpendra Kumar Sharma
(34640)

Professor, School of Civil Engineering

Lovely Professional University, Punjab

LOVELY PROFESSIONAL UNIVERSITY, PUNJAB
2026

DECLARATION

I, hereby declared that the presented work in the thesis entitled "**Study of Engineered Cementitious Composite Using Manufactured Sand"** in fulfilment of degree of **Doctor of Philosophy (Ph. D.)** is outcome of research work carried out by me under the supervision of Dr. Pushpendra Kumar Sharma working as Professor, in the School of Civil Engineering of Lovely Professional University, Punjab, India. In keeping with general practice of reporting scientific observations, due acknowledgements have been made whenever work described here has been based on findings of another investigator. This work has not been submitted in part or full to any other University or Institute for the award of any degree.

Sahil..

Sahil

Registration Number: 41800625,

School of Civil Engineering,

Lovely Professional University,

Punjab, India

CERTIFICATION

This is to certify that the work reported in the Ph. D. thesis entitled "**Study of Engineered Cementitious Composite (ECC) Using Manufactured Sand"** submitted in fulfillment of the requirement for the award of degree of **Doctor of Philosophy (Ph.D.)** in the School of Civil Engineering is a research work carried out by Sahil (41800625), is bonafide record of his/her original work carried out under my supervision and that no part of thesis has been submitted for any other degree, diploma or equivalent course.

Sharma

Dr. Pushpendra Kumar Sharma

Professor,

UID: 34640

School of Civil Engineering,

Lovely Professional University,

Punjab, India

ABSTRACT

The escalating demand for river sand in construction has led to excessive extraction, causing severe ecological disturbances and depletion of natural resources. In addition, the extensive use of cement raises CO_2 emissions worldwide, necessitating the development of sustainable substitutes as Engineered Cementitious Composites (ECC). which incorporate industrial by-products and reduce dependence on conventional materials while offering superior durability and mechanical performance. ECC is a type of fiber-reinforced cementitious materials that are distinguished by their remarkable tensile ductility and strain-hardening behavior. These properties are usually attained by incorporating tiny polymeric fibers, such as polyvinyl alcohol (PVA). Unlike conventional concrete, which fails in a brittle manner, ECC undergoes multiple microcracking with controlled crack widths, enabling it to sustain high deformation without significant loss in load-carrying capacity. This unique mechanical response, along with its enhanced durability and reduced material consumption, positions ECC as a viable material for sustainable and long-lasting infrastructure.

In response to challenges like excessive river sand dredging and high CO_2 emissions from cement production, this study explores the use of alternative construction materials such as manufactured sand (M-Sand), fly ash (FA), and sugarcane bagasse ash (SCBA) as sustainable substitutes in ECC. Through the gradual replacement of natural river sand with M-Sand in varied amounts of 0%, 20%, 40%, 60%, 80%, and 100%, this study aims to create an ECC mix that performs at its best. In an effort to further reduce the environmental impact, supplementary cementitious waste materials such as FA or SCBA were used as partial replacements for cement. Therefore, a total of 12 ECC mixes were prepared for this study, comprising two groups of six mixes each: the first group utilized fly ash while the second group incorporated sugarcane bagasse ash as partial cement replacements. Within each group, river sand was progressively replaced with manufactured sand at replacement levels of 0%, 20%, 40%, 60%, 80%, and 100%, respectively. To ensure

consistent workability across mixes, all ECC mixtures were created with a constant water-to-binder ratio of 0.27, a superplasticizer-to-binder ratio of 0.01 and a polyvinyl alcohol (PVA) fiber content of 2% by volume. The study evaluates key performance parameters including fresh properties (slump flow), mechanical strength (compressive strength, direct tensile strength and flexural strength), and durability characteristics (water absorption, sulphate attack, chloride attack, rapid chloride penetration and water permeability) to determine the most suitable combination of materials for structural applications.

The slump flow measurements showed that PVA fibers caused fresh properties to decrease from 25 mm in the control mix to 15 mm at 2% fiber addition. The water absorption capacity together with the high surface area of PVA fibers restricts the matrix's free flow behavior. The addition of superplasticizer (SP) minimized workability deterioration, but its efficacy became less prominent in the presence of fibers. The first group of six mixtures incorporating fly ash (FA) demonstrated superior mechanical performance compared to the mixtures containing sugarcane bagasse ash (SCBA), which can be attributed to the higher pozzolanic reactivity of FA. Among all 12 ECC mixes, the mix containing 40% river sand and 60% manufactured sand, FA-MS60, consistently demonstrated the highest mechanical performance in compressive strength, direct tensile strength, and four-point bending flexural strength. At 28 days, the mix FA-MS0 achieved a compressive strength of 36.42 MPa, whereas the mix FA-MS60 reached 43.98 MPa, reflecting an increase of approximately 20.75% in strength. Similarly, the FA-MS60 mix exhibited an increase of 17.59% in direct tensile strength and 31.11% in flexural strength at 28 days compared to the FA-based control mix containing 0% M-Sand. This superior performance was attributed to a balanced combination of particle characteristics: the rounded river sand particles improved workability and fiber dispersion, while the angular and rough-textured manufactured sand enhanced mechanical interlock and internal friction within the matrix.

In durability tests, water absorption in ECC mixes consistently decreased with increasing M-Sand content up to 60% for both fly ash and sugarcane bagasse ash blends,

with the lowest values observed at this level, indicating optimal pore refinement and densification. The same 60% M-Sand replacement also yielded superior performance in sulfate and chloride attack tests, with minimal weight loss 1.78% and 1.87% respectively after 180 days of exposure, reflecting enhanced chemical durability. Rapid Chloride Penetration Test (RCPT) results further supported these findings, showing a steady reduction in total charge passed up to 60% M-Sand replacement, signifying lower chloride ion penetrability, while a marginal increase was noted at 100% replacement. Water permeability also followed a similar trend, decreasing significantly up to 60% M-Sand content and increasing slightly beyond that point, affirming the 60% replacement level as the most effective for improving durability across all measured parameters.

To validate the optimum characteristics mechanical performance observed experimentally, a finite element analysis (FEA) was conducted using the ABAQUS software. The simulations focused on the best-performing mix (FA-MS60) under compressive and direct tensile loading conditions. The comparative analysis between the numerical and experimental results after 28 days showed a strong correlation, with the ABAQUS models successfully replicating the measured values. This indicates that the FEA approach was effective in capturing the mechanical behavior of the ECC mix, thereby confirming the reliability and robustness of the experimental findings.

Overall, the study establishes that replacing 60% of river sand with M-Sand in ECC, combined with FA as partial cement replacements, yields the most favorable balance between mechanical strength and durability. This mix, FA-MS60, demonstrated superior performance across all key parameters including compressive, direct tensile, and flexural strengths, along with resistance to water absorption, chemical attacks, chloride penetration, and water permeability confirming its potential as a sustainable and high-performance alternative for future structural applications.

Keywords: Engineered Cementitious Composites, Manufactured Sand, Sustainability, Mechanical Strength, Durability, Finite Element Method

GRAPHICAL ABSTRACT

STUDY OF ENGINEERED CEMENTITIOUS COMPOSITE USING MANUFACTURED SAND

Results

Workability

- ↓ Flow with ↑ PVA fibers percentage
- Flowability: ECC-FA > ECC-SCBA
- ↓ Flow with ↑ manufactured sand

Mechanical Properties

- The Optimum Mix in mechanical strength is FA-MS60.
- Highest Compressive, Direct Tensile and Flexural strength at 28 days: FA-MS60 i.e. 43.98 MPa, 7.14 MPa & 7.08 MPa respectively

Durability Properties

- Lowest density drop in FA-MS60.
- Lowest water absorption of 6.78% in FA-MS60.
- 40% RS + 60% M-Sand gave Maximum Compressive Strength against Chloride Attack & Sulphate Attack.

ACKNOWLEDGMENT

First and foremost, I bow in deep gratitude to Bhagwan **Mahadev**, my beloved God, whose divine blessings, guidance, and strength have been my constant support throughout this journey.

I extend my sincere thanks to my supervisor, **Dr. Pushpendra Kumar Sharma**, Professor, School of Civil Engineering, Lovely Professional University, for his unwavering guidance, valuable insights, and continuous encouragement at every stage of this research. His expertise and mentorship have played a crucial role in shaping this research work.

I am deeply grateful to my father, **Mr. Raman Kumar**, and mother, **Mrs. Rajni Jaggi**, for their unconditional love, prayers, sacrifices, and constant support. Their belief in me has been the foundation of all my achievements. A heartfelt thank you to my ex-wife, **Monica**, for her endless patience, understanding, and emotional support throughout this journey. I also thank my sibling, **Sagar Jaggi**, for always standing by me with love and motivation.

I would like to express my sincere appreciation to my mentors, **Dr. Geeta Mehta**, **Dr. Anshul Garg** and **Dr. Amit Kumar Dhir**, whose guidance and encouragement helped me stay focused and inspired throughout my academic journey.

Special thanks to my dear friends, **Dr. Tarunbir Singh**, **Mr. Akshat Mahajan**, **Dr. S. Ganesh**, and **Dr. Akash Aneja** for their constant support, stimulating discussions, and the many memorable moments we shared. Their friendship has been a source of strength and joy. This research has been a journey of learning, growth, and discovery, and I remain forever grateful to everyone who has contributed to its completion.

Sahil
Ph.D. Research Scholar
Lovely Professional University

CONTENTS

LIST OF ABBREVIATIONS

ABBREVIATIONS	MEANING
ECC	Engineered Cementitious Composites
HPFR	High-Performance Fiber Reinforced
FRC	Fiber Reinforced Concrete
FEM	Finite Element Method
FEA	Finite Element Analysis
FA	Fly Ash
SCBA	Sugarcane Bagasse Ash
RS	River Sand
M-Sand	Manufactured Sand
OPC	Ordinary Portland cement
SP	Superplasticizer
VMA	Viscosity-modifying admixture
PVA	Polyvinyl alcohol
PE	Polyethylene
PO	Polyolefin
PP	Polypropylene
SCMs	Supplementary cementitious materials
w/b	Water-to-Binder Ratio
SP/b	Superplasticizer to binder ratio
Cl-	Chloride ions
SO4 2-	Sulfate ions
NaCl	Sodium Chloride
Na_2SO_4	Sodium sulphate
NaOH	Sodium hydroxide
ITZ	Interfacial transition zone
µm	micrometer
kg/m^3	Kilogram per cubic meter
mm	millimeter
kN	kilo newton
°C	Celsius
MPa	Mega Pascal
K	water permeability coefficient
d	Days

LIST OF FIGURES

LIST OF TABLES

CHAPTER 1

INTRODUCTION

1.1 General Introduction

Concrete has traditionally served as the cornerstone of construction methods across the world because of its adaptability, durability, and mechanical strength as well as the accessibility of its component ingredients. [1], [2]. It forms the backbone of modern civil infrastructure, including buildings, bridges, pavements, and dams. However, despite its extensive use, conventional concrete possesses an inherent weakness: its brittle nature. This brittleness results in poor tensile strength, high shrinkage, and susceptibility to cracking under tensile stress or deformation. In structural applications, such cracking can lead to durability concerns, increased maintenance costs, and compromised safety, particularly under dynamic or seismic loading. For example, conventional concrete often fails under tensile loads or temperature variations, forming wide cracks that reduce service life and integrity.

To overcome these limitations, Fiber Reinforced Concrete (FRC) was introduced. By incorporating discrete fibers such as steel, glass, carbon, coconut, jute, and various polymer-based fibers into the concrete matrix [3], [4], FRC aims to bridge micro-cracks, improve post-cracking behavior, and enhance tensile strength and toughness [5]. However, while FRC does provide better crack resistance compared to plain concrete, it still exhibits quasi-brittle behavior and typically lacks the strain-hardening characteristics essential for high-performance, ductile materials [6].

1.2 Engineered Cementitious Composites

To address this gap, Engineered Cementitious Composites (ECC), commonly referred as bendable concrete, have been advanced as a new class of high-performance fiber-reinforced (HPFR) materials [7]. ECC is fundamentally different from conventional FRC as it exhibits tensile strain-hardening performance and forms numerous fine micro-cracks instead of few large cracks. Another difference is that ECC does not contain coarse aggregates, which enables better fiber dispersion again resulting in controlled crack width. These micro-cracks typically remain below 60 microns in width, significantly improving the durability, service life, and mechanical performance of structural elements [8], [9], [10]. In contrast to normal concrete, which typically fails at a tensile strain of 0.01%, ECC can sustain strains of 3–5%, making it 300 to 500 times more ductile than concrete [9].

ECC achieves this remarkable behavior using micromechanical design principles and a relatively low fiber volume content (typically up to 2%) [11], often using Polyvinyl Alcohol (PVA), polyethylene (PE), or other high-performance fibers [12], [13]. The synergy between the fiber properties and the cementitious matrix allows for controlled multiple cracking (see Figure 1.) [14] and strain hardening under tensile loads. Consequently, ECC combines the strength of concrete with the ductility and damage tolerance of metals.

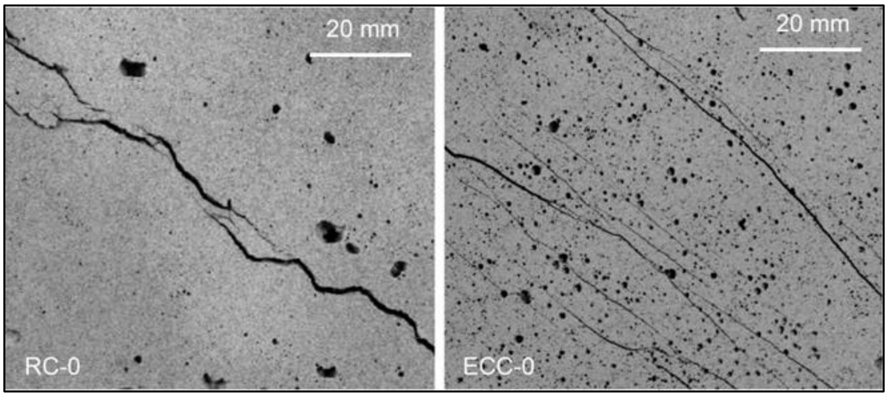

Figure 1: Crack Pattern difference between ordinary concrete and ECC [14]

In addition to its mechanical benefits, ECC enhances sustainability. Supplementary cementitious materials like Fly Ash (FA), Silica Fume (SF), and Granulated Blast Furnace Slag (GBFS) are used in ECC mixes to decrease cement content, thus lowering the emissions of carbon [15], [16], [17]. For instance, during the 2020-21 period in India, a total of 232.56 million tons of fly ash is produced. Despite its application in cement production and various other industries, as shown in Figure 2, 7.59% of the generated fly ash remained unutilized (Central Electricity Authority of India, 2021), highlighting its significant potential for use in ECC. This approach reduces carbon emissions and promotes resource efficiency while improving mechanical properties. However, optimizing ECC formulations with waste materials requires extensive research to assess their influence on performance, durability, and adaptability under varying conditions. By effectively incorporating such industrial by-products, ECC presents a viable pathway toward more sustainable and high-performance construction materials, further reinforcing its superiority over conventional concrete. Additionally, these materials not only improve the eco-efficiency of the composite but also contribute to better workability, reduced permeability, and improved resistance to aggressive environments.

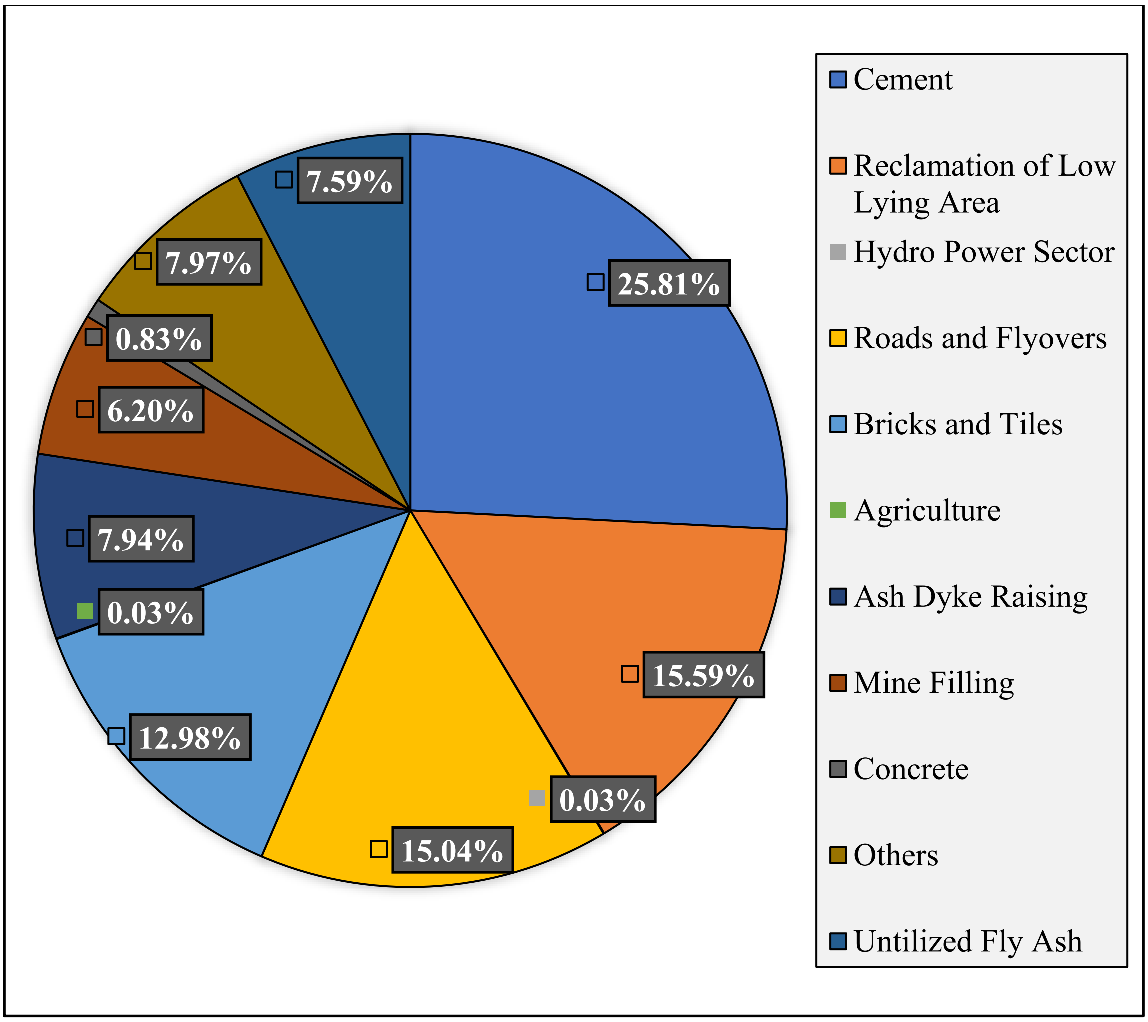

Figure 2: Fly Ash utilization in India in Year 2020-2021 (Central Electricity Authority of India, 2021)

The incorporation of supplementary cementitious materials (SCMs) in ECC necessitates a detailed understanding of the micromechanical behavior that governs their performance. The design philosophy of ECC relies heavily on the principles of micromechanics, particularly in tailoring the matrix and optimizing fiber-matrix interactions to achieve multiple micro-cracking and strain-hardening behavior. The subsequent section elaborates on these micromechanical foundations that underpin the distinctive properties of ECC.

1.3 Supplementary Cementitious Materials (SCMs) in ECC

Supplementary Cementitious Materials (SCMs) are widely incorporated in cement-based composites to improve mechanical performance, durability, and sustainability while reducing the consumption of ordinary Portland cement (OPC). SCMs generally consist of finely divided materials that exhibit pozzolanic or latent hydraulic properties, reacting with calcium hydroxide released during cement hydration to form additional calcium silicate hydrate (C–S–H) gel. This reaction leads to improved particle packing, refined pore structure, reduced permeability, and enhanced long-term strength and durability of cementitious systems.

Commonly used SCMs include fly ash (FA), ground granulated blast furnace slag (GGBS), silica fume, and metakaolin. These materials have been extensively studied in conventional concrete as well as in advanced cementitious composites due to their ability to enhance workability, mitigate heat of hydration, and improve resistance to aggressive environments. In the context of Engineered Cementitious Composites (ECC), SCMs play a particularly critical role, as ECC relies on a highly refined matrix to ensure controlled crack width, strain-hardening behavior, and effective fiber–matrix interaction. The selection and proportioning of SCMs therefore directly influence tensile ductility, crack propagation, and durability performance in ECC.

1.3.1 Fly Ash as an SCM in ECC

Fly ash, a by-product of coal-fired power plants, is one of the most widely used SCMs in ECC systems. Its fine particle size and predominantly spherical morphology enhance workability and flowability while reducing water demand. The pozzolanic reactivity of fly ash contributes to gradual strength development and improved matrix densification, which is essential for achieving stable multiple cracking and strain-hardening behavior in ECC. Owing to these advantages, fly ash has been extensively adopted in ECC formulations and is often regarded as a benchmark SCM for achieving high tensile ductility and durability.

1.3.2 Sugarcane Bagasse Ash as an Alternative SCM

Sugarcane bagasse ash (SCBA) is an agricultural waste material generated from the combustion of bagasse in sugar industries. With increasing emphasis on sustainable construction and waste utilization, SCBA has gained attention as a potential alternative SCM. When properly processed, SCBA contains reactive silica that can participate in pozzolanic reactions, contributing to strength development and microstructural refinement. However, compared to fly ash, SCBA typically exhibits coarser particle size, irregular morphology, and higher porosity, which can influence workability, matrix homogeneity, and fiber–matrix bonding in ECC. These characteristics make SCBA a more challenging but environmentally attractive SCM, warranting systematic investigation within ECC systems.

1.4 Micromechanics of ECC

Micromechanics is a field within materials science that focuses on understanding and predicting the mechanical behavior of composite materials by analyzing the interactions between their microstructural constituents such as fibers, matrix, and interfacial zones [18]. In the context of ECC, micromechanics serves as a foundational design approach to achieve desired strain-hardening behavior and tight crack width control under tensile loading [19]. Unlike conventional cement-based materials, ECC is engineered to exhibit a ductile failure mechanism characterized by multiple microcracking instead of brittle fracture [20]. This transformation in behavior is made possible through the careful manipulation of microstructural parameters, including fiber content, matrix toughness, fiber-matrix interface bond, and crack-bridging behavior [21]. By incorporating micromechanical principles, it becomes possible to quantitatively design ECC mixtures that not only possess adequate strength but also exhibit exceptional energy absorption and deformation capacity under tensile loads [22]. The micromechanical design framework for ECC is governed by two key interdependent criteria the Strength Criterion and the Energy Criterion both of which needs to be fulfilled simultaneously to achieve the characteristic strain-hardening behavior [18], [23], [24], [25].

The **Strength Criterion** ensures that once a crack initiates in the ECC matrix, the fiber bridging mechanism is capable of carrying the load across the crack without immediate failure [26]. It is expressed mathematically in Equation 1.

$$\sigma_0 \geq \sigma_{cr} \tag{1}$$

with σ_{cr} representing matrix cracking stress (the tensile stress at which the initial crack originates) and σ_0 representing the maximum bridging stress supplied by the fibers across the fracture plane.

This difference between σ_0 and σ_{cr} ensures that the peak stress the fibers can sustain during bridging is more than the stress at which the matrix fails in tension. If this criterion is satisfied, the applied load, once causing a matrix crack, is effectively transferred to the fibers that bridge the crack. Instead of a single wide crack propagating unstably, this load redistribution mechanism allows for the initiation of additional multiple micro cracks at other flaw sites in the matrix, leading to a stable and distributed microcracking process.

The fiber bridging law represents the constitutive connection between the crack opening displacement (δ) and the bridging stress (σ) that governs the fracture-bridging behaviour. This relationship is critical in defining the parameters such as the corresponding crack width δ_0 at peak stress σ_0 (see Figure 3)*[27]*. The peak stress is also denoted by steady-state bridging stress (σ_{ss}) at which the composite undergoes stable multiple microcracking.

While the strength criterion governs crack initiation and the ability to form multiple cracks, the **Energy Criterion** governs the stability of crack propagation. This criterion ensures that once a crack begins to propagate, it does not extend uncontrollably through the matrix [28]. The criteria is satisfied when the complementary energy provided by fiber bridging, denoted as J'_b, is greater than or equal to the crack tip toughness J_{tip}. The criterion is expressed in Equation 2 and 3.

$$J'_b \geq J_{tip} \tag{2}$$

Where J'_b is complementary energy from fiber bridging and J_{tip} is energy required to advance a crack tip. From the fiber bridging law, the complementary energy J'_b and the fracture energy at the crack tip J_{tip}, which are related to the composite's fracture toughness, may be calculated as follows:

$$J'_b \equiv \sigma_0\,\delta_0 - \int_0^{\delta 0} \sigma(\delta)d\delta \geq \sigma_{ss}\delta_{ss} - \int_0^{\delta ss} \sigma(\delta)d\delta = J_{tip} = K_{tip}^2 / E_C \cong K_m^2 / E_m \quad (3)$$

Here, σ_0 represents the peak bridging stress associated with the crack opening δ_0, while σ_{ss} denotes the steady-state bridging stress corresponding to the crack width δ_{ss}. The parameter K_{tip} signifies the fracture toughness at the crack tip, and E_c is the composite's Young's modulus. Ktip and Ec can be roughly represented as the matrix fracture toughness K_m and matrix modulus E_m, respectively, in ECC with a low fiber volume fraction (~2%).

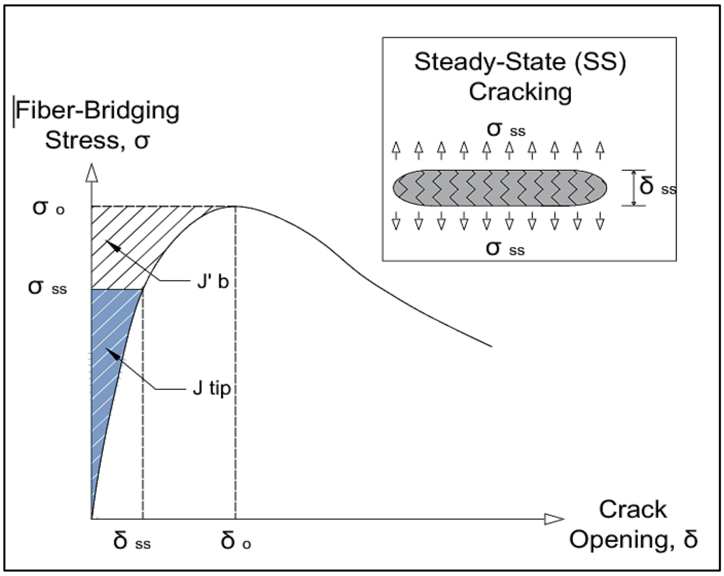

Figure 3: Stress (σ) and Strain (δ) diagram of ECC under tension [18], [27]

This approximation is valid for ECC where the fiber volume fraction is relatively low (typically 2% or less), allowing the composite's fracture toughness and stiffness to be considered nearly equal to that of the matrix. When the complementary energy J'_b exceeds the crack tip energy J_{tip} the crack growth becomes stable, promoting further microcrack formation rather than catastrophic failure *[27]*.

Satisfying both criteria is essential for ECC to exhibit strain-hardening behavior [29]. The Strength Criterion ensures that each matrix crack is successfully bridged and controlled by fibers, while the Energy Criterion guarantees that new cracks can form in a distributed manner without allowing existing cracks to propagate uncontrollably. Together, these criteria enable the development of numerous, fine cracks under tensile load each crack typically remaining less than 60 µm in width [30]. This helps the composite be more ductile and durable over time by preventing the entry of harmful chemicals like moisture and chlorides. [31].

In conclusion, micromechanics-based design provides a robust scientific framework for developing ECC with predictable and high-performance mechanical properties. It bridges the gap between material science and structural engineering, offering a rational methodology to design ductile, crack-resistant cementitious materials suitable for a variety of structural and repair uses.

While micromechanics offers a fundamental understanding of the internal mechanisms governing the behaviour of ECC at the material scale, it often relies on simplified assumptions. To further explore and predict the mechanical response of ECC under various loading conditions, Finite Element Analysis (FEA) serves as a complementary tool. FEA enables the simulation of complex stress strain behavior and crack propagation patterns by incorporating material properties into a numerical framework, thus bridging the gap between theoretical models and real-world structural performance.

1.5 Finite Element Method

The Finite Element Method (FEM) has emerged as a powerful computational means for simulating the complex mechanical behaviour of ECC. ECC exhibit strain-hardening and multiple microcracking characteristics, which are difficult to fully capture using conventional analytical methods. FEM facilitates the understanding of stress distribution, crack propagation, and failure mechanisms in ECC under various loading conditions by providing a virtual testing environment.

The use of FEM in ECC research serves three main purposes:

1. Prediction of mechanical performance: FEM helps in predicting tensile, compressive, and flexural responses of ECC under both monotonic and cyclic loads.

2. Parametric analysis: It supports virtual testing of material and structural parameters (e.g., fiber volume, matrix properties, notch size) without the need for exhaustive physical experimentation.

3. Validation of experimental findings: Simulation results are compared with laboratory test data to validate models and ensure realistic behavior is captured, aiding in design optimization.

In particular, FEM allows researchers to model ECC's heterogeneous structure at different scales from micro-scale fiber-matrix interactions to macro-scale structural elements making it possible to estimate properties like compressive strength, tensile strength, fracture energy, ductility, and stiffness. Software platforms such as ABAQUS, ANSYS, and COMSOL have been widely used to simulate ECC behaviour through constitutive models that incorporate damage plasticity, cohesive zone modelling, and user-defined material subroutines.

The comparison between experimental and FEM simulation results for ECC reveals a high degree of correlation and validation across various studies, demonstrating the effectiveness of FEM in predicting ECC behaviour. In the study by Yuan et al., the FEM model developed for ECC beams with Yellow River Sand (YRS) replacement was validated against experimental data, showing good agreement in predicting flexural strength and ductility, which is crucial for sustainable engineering application [32]. Similarly, Liu et al. demonstrated that FEM simulations accurately predicted the flexural ability of RC beams thru ECC layers, with the numerical outcomes closely matching experimental outcomes, particularly for beams with ECC layers at both the upper and lower, which showed significant improvements in bearing capacity and ductility [33]. Ren et al. further confirmed the accuracy of FEM in simulating the seismic performance of ECC-retrofitted structures, where the numerical models effectively captured the enhanced deformation capacity and load-bearing improvements post-retrofit, aligning well with experimental observations [34]. The study by Woo et al. focused on tensile strain hardening behaviour, where FEM simulations using a nonlinear program accurately replicated experimental tensile stress-strain curves, validating the model's capability in predicting ECC's strain hardening response [35], [36], [37]. Additionally, Maheswaran et al. and Arulanandam et al. both utilized FEM to explore the shear behaviour of ECC beams, with simulations accurately reflecting experimental results, particularly in relations of load-deflection behaviour and modes of failure, thus confirming the reliability of FEM in assessing ECC's structural performance under shear loads. These studies collectively underscore the robustness of FEM as a tool for simulating ECC behaviour, providing a reliable means to predict performance characteristics that are consistent with experimental findings across various structural applications.

In summary, FEM bridges the gap between theoretical models and experimental results, making it a vital tool for assessing the mechanical performance of ECC. Its application in early-stage research supports material optimization and paves the way for performance-based design in real-life structures.

1.6 Problem Statement

Despite its seeming abundance, sand is a limited and becoming more precious resource that is essential to preserving biodiversity, delivering ecological services, and supporting essential infrastructure for economic growth and community livelihoods. The excessive extraction of natural sand for construction purposes has led to severe environmental concerns, including riverbed degradation, biodiversity loss, and groundwater depletion. Sand is essential for sustaining ecological equilibrium, supplying livelihoods, promoting economic growth, and delivering ecosystem services. [38]. All 17 of the Sustainable Development Goals (SDGs) have some sort of direct or indirect connection to it. In spite of this, the use of natural sand is increasing.

Simultaneously, the cement industry remains one of the largest contributors to global carbon dioxide emissions, accounting for nearly 8% of total anthropogenic CO_2 output [39]. The widespread use of cement in engineered composites intensifies this impact. While industrial byproducts like fly ash have been extensively studied, other agro-waste materials such as sugarcane bagasse ash remain underexplored in the context of sustainable construction.

1.7 Research Gap

Despite the remarkable mechanical properties and crack control capabilities of Engineered Cementitious Composites (ECC), several critical research gaps persist that impede their widespread adoption in infrastructure applications.

1. Although Engineered Cementitious Composites (ECC) have been extensively studied with conventional fine aggregates such as natural river sand and micro-silica sand, limited attention has been given to the utilization of manufactured sand (M-Sand) as a partial or complete replacement. The impact of M-Sand on the fresh, mechanical, and especially durability properties of ECC remains inadequately explored. Most existing literature focuses on standard materials with well-established behavior, whereas the role of M-Sand, which differs in particle shape, texture, and grading, has not been comprehensively assessed in ECC matrices.
2. Furthermore, while fly ash is extensively utilized as a supplementary cementitious material (SCM) in ECC for enhancing ductility and durability, the potential of sugarcane bagasse ash (SCBA) remains underutilized. Despite its pozzolanic properties and environmental advantages, there is a notable lack of research exploring the incorporation of SCBA in ECC, especially in combination with other materials like M-Sand.

1.8 Hypothesis and Variables

A well-defined study framework is necessary in order to methodically examine the impact of using manufactured sand in place of river sand in Engineered Cementitious Composites (ECC). This includes identifying the independent and dependent variables, and formulating both the null and alternative hypotheses based on the expected impact of varying replacement levels on the fresh, mechanical, and durability characterization of ECC. The Table 1 outlines the structured hypothesis framework adopted for this study.

Table 1:Research Variables and Hypothesis Framework for M-Sand Replacement in ECC

Component	Description
Research Question	Does the partial replacement of river sand with manufactured sand effect the fresh, mechanical, and durability characteristics of Engineered Cementitious Composites (ECC)?
Independent Variable	Percentage substitute of river sand with manufactured sand (e.g., 0%, 20%, 40%, 60%, 80%, 100%)
Dependent Variables	*1. Fresh Properties*: Flowability *2. Mechanical Properties*: Compressive strength, direct tensile strength, flexural strength *3. Durability Properties*: Water absorption, dry density, sulphate resistance, chloride resistance, water permeability, rapid chloride ion penetration
Alternative Hypothesis (H_1)	The partial replacement of river sand with manufactured sand at varying percentages (0%, 20%, 40%, 60%, 80%, 100%) has a significant effect on the fresh, mechanical, and durability properties of ECC.
Null Hypothesis (H_0)	The partial replacement of river sand with manufactured sand has no significant effect on the fresh, mechanical, or durability properties of ECC.

1.9 Research Objectives

The primary goal of this study is to create an optimized Engineered Cementitious Composite with balanced workability, mechanical properties, and enhanced durability through optimum M-Sand content variation. The specific objectives are:

1. To arrive at optimum Mix based on literature and various trials.
2. To evaluate the mechanical and durability properties of Engineered Cementitious Composite (ECC).

3. To validate the obtained mechanical results of the study by using simulation software.

1.10 Scope of the study

This research encompasses:

1. Systematically replacing natural river sand with M-Sand at varying proportions of 0%, 20%, 40%, 60%, 80%, and 100% maintaining a constant cementitious material, water-to-binder ratio, and admixtures content across all mixtures.
2. Assessment of fresh properties, including slump flow and workability.
3. Comprehensive mechanical property characterization including compressive strength, direct tensile strength and flexural strength for 7, 28, and 90 days.
4. Durability evaluation through water absorption, water permeability, chloride resistance, and sulfate resistance, and rapid chloride permeability testing for 28, 90 and 180 days.

1.11 Thesis Structure Overview

This thesis is divided into the following five chapters:

Chapter 1: Introduction

An introduction to Engineered Cementitious Composites (ECC) is given in this chapter, with emphasis on the material's significance, micromechanical foundation, and modeling possibilities with the Finite Element Method (FEM). In addition, the chapter sets the research hypotheses, specifies the issue statement, identifies research gaps, and describes the goals and parameters of the study.

Chapter 2: Literature Review

This chapter offers an in-depth review of ECC, including its development, applications, and mix design methodologies. Additionally, it talks about ECC's mechanical, fresh, and durability characteristics in a variety of environmental settings, including heat, sulfate, chloride, and freeze-thaw cycles. Cementitious material durability issues and service life factors are also examined.

Chapter 3: Methodology

The methodology section highlights the ECC mixture proportioning scheme which defines all the used materials together with their individual weights. The preliminary mixing trials through Trial Mix to find optimal ECC formulation parameters. Specifies preparation techniques leading to ECC specimen casting. The experimental setups with corresponding tests. The tests measuring workability and flow are part of the assessment of the fresh properties of the material. Mechanical properties include evaluations of strength and ductility, while durability properties involve assessments of the material’s resistance to various environmental factors.

Chapter 4: Results and Discussions

The findings are presented and discussed in this chapter obtained from testing the fresh, mechanical, and durability properties of ECC with various levels of manufactured sand replacement. It includes performance analysis for compressive, tensile, and flexural strength, along with durability aspects like water permeability, sulphate and chloride resistance, and RCPT. The FEM simulation results are also included and validated against experimental findings.

Chapter 5: Conclusion and Recommendation

The last chapter emphasizes the contributions to current knowledge and summarizes the main study findings., and offers practical recommendations for the use of manufactured sand and supplementary cementitious materials in ECC. It also lists the present study's limitations and makes recommendations for future research avenues.

CHAPTER 2

LITERATURE REVIEW

2.1 Introduction of ECC

Engineered Cementitious Composites (ECC), first developed in the early 1990s by Li and colleagues at the University of Michigan as a solution to the brittleness and cracking issues associated with traditional concrete represent a revolutionary type of fiber-reinforced cementitious materials categorized by their superior ductility, tensile strain capacity, and damage tolerance [40]. Unlike conventional concrete, which exhibits brittle failure under tensile loading, ECC demonstrates strain-hardening behavior and can sustain tensile strain capacities of 3-5%, roughly 300-500 times that of normal concrete [41], [42]. This exceptional performance is achieved through micromechanical design principles that optimize the interaction between fibers, matrix, and fiber-matrix interfaces [41], [42].

The superior performance of ECC is attributed to its carefully tailored composition. The primary ingredients include a cementitious matrix, Ordinary Portland cement (OPC) or blended cement [43]. Fine aggregates, typically silica sand, eliminating the need for coarse aggregates to enhance fiber dispersion Polymeric fibers, commonly polyvinyl alcohol (PVA) or polyethylene (PE) fibers, which play a critical role in bridging microcracks Supplementary cementitious materials (SCMs), fly ash (FA), silica fume (SF), or slag to enhance workability and reduce environmental impact. Water-to-Binder Ratio (w/b) of ECC is typically low in the range of (0.25–0.35) to optimize strength and durability [44]. Chemical admixtures or high-range water reducers (superplasticizers) to enhance flowability and fiber distribution [45]. The absence of coarse aggregates allows for better crack control and fiber alignment, leading to a uniform strain distribution and high energy absorption capacity. The key mechanical properties that distinguish ECC from conventional concrete include, high tensile strain capacity (3–5% as instead of 0.01% for ordinary concrete), moderate tensile strength (4-6 MPa), self-controlled crack width (typically below 100 µm), Significant energy absorption capacity has been observed in studies, attributed to the careful control of fiber-matrix interactions, especially the chemical and mechanical bonding amid the fibers and the surrounding cementitious matrix [15]. The tailored interfacial properties ensure that fibers bridge cracks without rupturing, while allowing controlled pullout that distributes deformation across multiple microcracks rather than localizing in a single fracture plane.

Unlike traditional concrete, which forms large cracks under stress, ECC exhibits distributed microcracks (typically 50–100 μm wide) [46]. These microcracks enhance energy absorption and durability. The fibers act as load transfer agents, preventing crack propagation and enabling strain hardening. The cementitious matrix's connection with the fibers is meticulously designed. PVA fibers have a hydrophilic surface, which allows strong bonding but is controlled to prevent fiber rupture before pullout. A surface coating on the fibers is often used to optimize this balance. A well-balanced bond between the fibers and cementitious matrix ensures effective stress transfer without premature fiber rupture or pullout [47].

The development of ECC has addressed significant limitations in traditional concrete technology, particularly regarding crack width control and durability. While conventional fiber-reinforced concrete (FRC) typically contains 1-2% fiber volume fraction [48]. ECC achieves its remarkable properties with comparatively little fiber content (typically 2% or less by volume), making it both technically superior and potentially economically viable for wide-scale implementation [49]. The careful optimization of fiber type, geometry, distribution, and matrix composition enables ECC to maintain tight crack widths (typically below 100 μm) even under considerable deformation [50], [51],which is essential for long-term performance. As the microcracks when exposed to water and CO_2, anhydrate cementitious materials and calcium hydroxide react to form additional C-S-H gel, closing the cracks over time.

2.2 Applications of ECC

The exceptional mechanical characteristics of ECC, such as high ductility, multiple microcracking, and self-healing capability, have led to its successful implementation in various structural and infrastructure applications. This section presents a selection of practical applications and real-world projects where ECC has been employed to address critical engineering challenges.

The Mihara Bridge in Japan was the first large-scale ECC bridge project, replacing expansion joints with ECC link slabs. After 15+ years, the slabs show excellent durability against freeze-thaw cycles and heavy traffic as seen in Figure 4(a), 4(b) and 4(c) [18].

(a) Outline of the bridge

(b) Adopted plate-type dowels *(c) Placement of HPFRCC*

Figure 4: Overview of Mihara Bridge [18]

Similarly, the Grove Street Bridge in Michigan demonstrated ECC's ability to eliminate expansion joints, reducing maintenance costs and improving durability under extreme temperature fluctuations and truck loads [52]. The Mitaka Dam in Japan was retrofitted with a 20mm ECC overlay, enhancing watertightness and resistance to environmental damage. It has performed well for nearly two decades, proving ECC's longevity in harsh conditions [53]. ECC was also used for lining the Shimizu Tunnel and a Hokkaido water conveyance tunnel, providing exceptional crack control, waterproofing, and durability in aggressive underground environments [54].

A 27-story residential tower in Yokohama used ECC coupling beams in its core wall system to enhance earthquake resistance (see Figure 5). The material's strain-hardening and energy absorption capacity significantly improved seismic performance, demonstrating ECC's effectiveness in high-rise buildings [53].

(a) ECC coupling beams, (b) Omni mixer mixing the fresh ECC, (c)Casting of ECC coupling beam together with partial floor slab, and (d) ECC coupling at the building construction

Figure 5: ECC coupling beams in Core Wall Structure of s 27-story residential tower at Yokohama

The BART tunnel retrofit used ECC panels to increase earthquake resistance, ensuring durability in an underground environment [55]. ECC overlays (25-50mm thick) were applied to rehabilitate concrete pavements in Michigan, significantly reducing reflective cracking and freeze-thaw damage compared to conventional concrete [56]. High-early-strength ECC enabled rapid overnight repairs of airport runways, reopening to traffic within 4-6 hours while maintaining durability against jet fuel and aircraft loading [57]. This project involved the first field-cast ECC material in the United States, where ECC was used for link slabs. The implementation eliminated the need for conventional expansion joints, reducing future maintenance requirements. Post-construction monitoring has shown excellent performance with minimal cracking despite Michigan's harsh winter conditions [42]. ECC was used in Michigan’s water treatment tanks, offering self-healing properties and durability in chemically aggressive environments. It maintained water-tightness and structural integrity over time [57].

Precast ECC panels were also installed along Tomei Highway as sound barriers, providing impact resistance and long-term durability in roadside conditions as seen in Figure 6 [54].

(a) Before repair *(b) After repair*

Figure 6: Surface repair of the concrete retaining wall [54]

Aging infrastructure demands durable materials to minimize repair costs and environmental impact. ECC enhances sustainability by extending service life through superior crack control, reducing life-cycle costs, and promoting resilience [58], [59]. Balancing ECC’s fiber content is crucial for durability and workability. Excess fibers increase costs and reduce workability, while insufficient fibers weaken performance. Identifying optimal fiber thresholds ensures durability [60], [61], [62]. High fiber content in ECC reduces workability, complicating placement. Research on optimizing fiber dosage while maintaining fresh properties is essential for large-scale applications [11], [63], [64], [65]

2.3 Mix Design of ECC

ECC mixture consists of cement, fiber, cementitious material, water, fine aggregates, and admixtures [5], [66]. ECC does not include coarse aggregates, and in some cases, excludes fine aggregates altogether [67]. The particle size of all components in the ECC matrix must be carefully graded to ensure the attainment of self-consolidating properties in its fresh state [3], [68]. Furthermore, the surface coating of fibers with oil resulted in the most effective self-healing properties and minimized the crack width [69]. A high-range water reducer (HRWR) like polycarboxylate facilitates rapid precipitation of dry powder, while hydroxypropyl methylcellulose (HPMC) in powder form is introduced to regulate the viscosity and cohesion of the mix [70]. To achieve desirable properties in both fresh and hardened states of ECC, Polyvinyl Alcohol (PVA) fiber fraction by volume ranging from 0.015 to 0.017 alongside a Fly Ash (FA) content of 50% to 55% was found to be more effective [71].

Studies employed a cement-to-GGBS ratio spanning between 1:1 to 1:2.5, and silica fume measurements existed between 0.15 to 0.3 parts or as a 5–10% proportion relative to the binder content [72], [73], [74]. Researchers maintained low water-to-binder ratios between 0.22–0.30 to enhance strength results and lower porosity throughout the specimen[75]. PVA fiber dosage remained between 1.5% and 2% volume, which offered the best combination of material workability and crack control, and ductility [76].

Test results showed compressive strengths between 38 MPa and 90 MPa and these high values emerged when GGBS and silica fume percentages increased together with reduced W/B ratios. A mix containing two parts GGBS with 0.3 parts silica fume while maintaining 0.23 W/B ratio and using 2% PVA achieved compressive strength between 75-90 MPa [77]. The materials reached 9 MPa tensile strength levels along with 5% tensile strain levels [59], [77]. The combination of 2% PVA fiber with optimally used SCM leads ECC to show excellent ductile behavior. The flexural strength measurements spanned between 10 MPa to 18 MPa because silica fume improved performance by enabling both matrix densification and fiber bridging [78], [79].

Studies demonstrated a united finding about enhanced performance in crack control along with decreased shrinkage and self-healing functionality and chloride resistance, and frost protection. The combined use of GGBS with silica fume produced an exceptional synergy, which decreased permeability while enhancing long-term performance in hostile environments like sea exposure [59], [77]. Increased amounts of GGBS exceeding 70% contributed to significant greenhouse gas emission reductions, thereby making ECC suitable for sustainable construction applications [59], [77]. Optimizing the mixture proportions of GGBS with silica fume and PVA fibers in ECC creates strong and ductile sustainable material that demonstrates high durability.

Fly ash (FA) has been extensively investigated as a supplementary cementitious material in engineered cementitious composites due to its favorable physical and chemical characteristics. FA particles are typically fine and spherical, which improves particle packing, reduces water demand, and enhances workability in ECC systems [Ref]. From a mechanical perspective, the pozzolanic reaction between FA and calcium hydroxide leads to gradual formation of secondary C–S–H gel, resulting in improved matrix densification and long-term strength development [Ref]. In ECC, this refined matrix is critical for achieving stable strain-hardening behavior, as it facilitates uniform fiber dispersion and controlled microcrack formation under tensile loading [Ref].

Several studies have reported that FA-based ECC exhibits superior tensile ductility, reduced crack width, and improved durability compared to cement-rich matrices [Ref]. High-volume fly ash ECC systems have been shown to achieve tensile strain capacities exceeding 2–3%, while maintaining adequate compressive strength and enhanced resistance to chloride ingress and sulphate attack [Ref]. The use of FA also contributes to reduced heat of hydration and improved dimensional stability, making it a preferred SCM in ECC formulations [Ref]. Consequently, FA is widely regarded as a benchmark SCM for ECC research and practical applications.

In contrast, sugarcane bagasse ash (SCBA) has emerged as a potential alternative SCM, primarily driven by sustainability considerations and the need to utilize agricultural waste materials. SCBA is a by-product of bagasse combustion in sugar industries and is generally rich in amorphous silica, which can exhibit pozzolanic activity when properly processed [Ref]. Previous investigations on conventional concrete and mortar systems have shown that SCBA can contribute to strength development and pore structure refinement, particularly at moderate replacement levels [Ref]. However, the effectiveness of SCBA as an SCM is strongly influenced by its particle size, morphology, and carbon content, which vary depending on combustion and grinding processes [Ref].

Compared to fly ash, SCBA particles are typically coarser, more angular, and more porous, leading to increased water demand and reduced workability in cementitious systems [Ref]. These characteristics can adversely affect matrix homogeneity and fiber–matrix bonding in ECC, where uniform stress transfer and crack control are essential [Ref]. Limited studies have explored the use of SCBA in ECC, and those available indicate that while SCBA-based ECC can exhibit strain-hardening behavior, the tensile ductility and durability performance are generally lower than FA-based ECC due to higher porosity and reduced pozzolanic reactivity [Ref].

Despite these challenges, the use of SCBA in ECC presents significant opportunities for sustainable construction, particularly in regions with abundant sugar industry waste. Comparative investigations between FA- and SCBA-based ECC under identical mix proportions and aggregate replacement conditions remain scarce in the literature. Moreover, limited studies have examined the combined influence of alternative SCMs and manufactured sand on the mechanical, tensile, durability, and numerical performance of ECC [Ref].

2.4 Fresh Properties of ECC

Characteristics for both concrete and ECC in their fresh state have significant importance in workability concerning stress-strain behavior and durability [80]. The workability and flowability of ECC are among the fresh-state properties. The percentage of fibers in ECC mixes has a great impact on their workability and density [81], [82]. The workability of ECC is influenced by the fibers' aspect ratio, the fiber content present, and aggregates quantity and size [83]. Fibers reduce the water-cement ratio in ECC, which leads to low workability, but with the addition of plasticizers, can increase workability [84]. Observations showed that as the fiber content increased, workability decreased. Specifically, with a fiber percentage of more than 2%, there was an average decrease in workability of approximately 35%. As the percentage volume of the PVA fiber, the workability of the ECC mix decreased, likewise its density [81], whereas increased levels of FA replacement showed the opposite effect [71]. ECC with larger rubber particles generally exhibits greater workability and higher fresh density compared to mixtures containing smaller particles [85], [86], [87]. For hybrid fiber, ECC requires a superplasticizer to counterbalance the slump value reduction resulting from the addition of fiber content. It was also noted that an increase in limestone powder (LSP) content reduces the fluidity of fresh ECC [88]. A water-reducing admixture with a high-range capability, with a polycarboxylate composition, proves most efficient in preserving the desired fresh properties throughout the mixing and placing processes [82].

The rheological characteristics of Engineered Cementitious Composites (ECC) are significantly influenced by their constituent materials, with GGBS, SF, and PVA each playing distinct roles. Research by [89] demonstrated that GGBS replacement levels of 30-50% improved the flowability of ECC mixtures due to the spherical particle shape and lower water demand of GGBS, compared to silica fume typically reduces workability due to its high specific surface area and increased water demand, with significant effects observed above 10% replacement levels. Similarly, [25] demonstrated that PVA fiber addition generally reduces flowability, with more pronounced effects at higher fiber contents (>1.5% by volume), yield stress, and plastic viscosity with increasing PVA fiber content. Despite these workability challenges, silica fume offers benefits beyond strength development. It has been observed that increased cohesiveness and reduced segregation potential in ECC mixtures containing silica fume, which helps maintain fiber dispersion. This cohesiveness complements the findings of [15], who indicated improved resistance to bleeding and segregation with GGBS inclusion, attributed to enhanced particle packing density and microstructural homogeneity.

Further rheological insights revealed enhanced thixotropic properties in silica fume-modified ECC, with greater structural buildup at rest and improved breakdown under shear. These properties affect not only the fresh behavior but also the hardened microstructure; silica fume tends to reduce entrapped air content in fresh ECC mixtures, leading to denser microstructures upon hardening. Maintaining proper fiber dispersion has proven crucial, as evidenced by [61][49], who showed that fiber clumping leads to severe workability issues. The integrated effects of these materials have been extensively studied [88], reporting altered response to vibration in fiber-reinforced ECC mixtures and noting the potential for fiber segregation under excessive vibration energy. Recognizing the complex interactions between these components, GGBS can partially offset the negative workability impacts of silica fume and PVA fibers when used in appropriate proportions. increased water demand from silica fume and PVA fibers could be partially compensated by GGBS inclusion. Optimal combinations (40% GGBS, 5% silica fume, 2% PVA fiber) that balanced workability requirements with mechanical performance. However, mixtures containing all three components typically require higher superplasticizer dosages to maintain target workability levels, underscoring the need for careful mixture design and proportioning in ECC systems.

2.5 Mechanical Properties of ECC

Integrating fibers into the ECC mixes significantly improved compressive, tensile, and flexural strengths [90]. The diameter and aspect ratio of fibers contribute to ductility and tensile capacity of the concrete, whereas utilizing small-diameter (hair-like) fibers leads to more ductile and high-strength concrete compared to employing large-diameter (thick) fibers [81]. The mechanical properties of a PVA-ECC show a proportional increase with the volume percentage of fiber up to 1.5%. However, exceeding 1.5% volume of fiber led to a decrease in mechanical properties [81]. 3D printing-ECC specimens' compressive strength showed an increase as the curing ages progressed from 1 day to 28 days. Additionally, the tensile properties displayed minimal variation in size, attributed to the uniform fiber orientation [91]. The increase of PVA fiber content modestly improved compressive, flexural, and tensile strength within the range of 0.01 to 0.015. However, this trend changed after the fiber addition of more than 0.02 [92]. By integrating hybrid fibers into the ECC mix, the compressive strength, tensile and flexural strength, and ductility of ECC got better. [93].

Concerning the research, the mechanical behaviour of Engineered Cementitious Composites (ECC) can be significantly enhanced through the strategic incorporation of GGBS, SF, and polyvinyl alcohol PVA fibers [94]. Replacing 30-50% of cement with GGBS increased the compressive strength of ECC by 15-25% after 28 days of curing [60], while GGBS-ECC mixtures exhibited higher flexural strength (up to 12 MPa) compared to conventional ECC (8-10 MPa) [95]. This strength improvement coincides with enhanced ductility, as found that GGBS incorporation improved the tensile strain capacity of ECC from 3% to approximately 4.5%. The mechanisms behind these improvements were elucidated by [97], who demonstrated that GGBS enhances the matrix-fiber interface through pozzolanic reactions, improving fiber bridging capacity, and, [96] showed that GGBS reduces the calcium hydroxide content, resulting in a denser microstructure that improves fiber pullout resistance. Silica fume further contributes to strength development, with the combination of 5-10% SF increasing the compressive strength of ECC by 20-30% [97] and, observing that silica fume addition improved the tensile strength by up to 25% while maintaining strain capacity. The microstructural effects of silica fume were found to enhance the chemical bond between PVA fibers and the cementitious matrix, though excessive bonding can reduce strain capacity [74].

For optimized performance, the ideal silica fume content for balanced strength and ductility was 7-8% by weight of cement [98], while showed that silica fume creates a denser cementitious matrix, reducing the porosity by up to 30% [99]. The synergistic effect of combining materials was demonstrated in which ultrafine silica fume particles fill the gaps between cement and GGBS particles, creating a more compact microstructure [100]. The role of PVA fibers has been equally crucial, with establishing that fibers with a diameter of 39-43 μm and length of 8-12 mm exhibited optimal performance in ECC [101], and [83] determining that a fiber volume fraction of 2% provides the best balance between workability and mechanical performance [102]. The unique fiber-matrix interaction was explored by, who showed that the high chemical bond between PVA fibers and cementitious matrix necessitates interface tailoring through surface treatments or admixtures. The controlling this interfacial bond is crucial for gaining strain-hardening behavior [103]. The mechanics of this behavior was due to fiber bridging across cracks enables the composite to sustain increasing loads after first cracking [104]. The combined effects of all three components have shown remarkable synergy; GGBS and silica fume create multiple nucleation sites for cement hydration, accelerating strength development [105], while these findings culminated in practical applications documented by who found that ECC mixtures with 40% GGBS, 8% silica fume, and 2% PVA fibers by volume achieved compressive strengths exceeding 70 MPa and tensile strengths of 5-6 MPa. The significant improvement was quantified by, who reported that this combination increased flexural strength by 35% compared to mixtures with only one supplementary material, demonstrating the powerful synergistic effect of properly proportioned constituent materials in ECC [106].

2.6 Durability Properties

2.6.1 Salt Corrosion Resistance

Sulfate attack resistance is crucial for buildings that come into contact with soil, such as concrete piles and foundations. By restricting the concrete's water-to-cement ratio, demanding a minimum compressive strength, and utilizing Type II or Type V cement that has been carefully mixed for sulfate resistance, enough resistance to sulfate attack can be accomplished. [107]. Concrete exposed to a salt environment experiences corrosion, which is due to the infiltration of chloride ions (Cl^-) or sulfate ions (SO_4^{2-}) into its surroundings [108]. Chloride ions primarily target the internal steel reinforcements within the concrete, causing structural degradation. Meanwhile, sulfate ions react with silicate and aluminate phases in cement, leading to calcium vanadate formation. This action results in water absorption, expansion, cracking, and eventual destruction of the concrete [109], [110]. The problem of corrosion of steel in a chlorine environment, especially in the marine environment, has been resolved by integrating fiber-reinforced polymer [111]. This can be applied in wastewater treatment plants and pipes built with concrete, which are mainly exposed to violent chemicals and may lead to cracks [112]. An upsurge in fly ash-to-cement ratio lowers corrosion [112], [113]. It was also noted that the compressive and tensile strength of ECC under extended exposure time of 200 days to Na_2SO_4 and with NaCl solutions increased while tensile strain decreased, this is seen in Figure 7 [108].

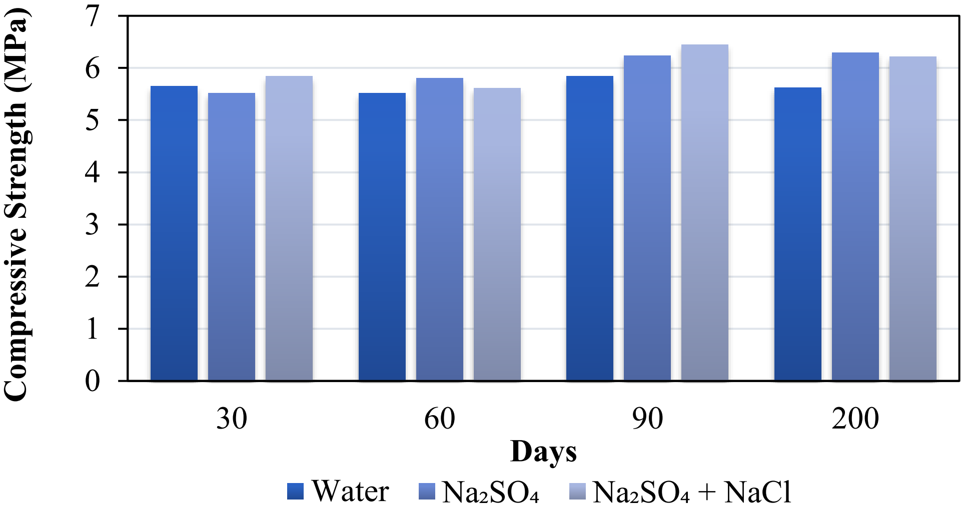

Figure 7:Compressive strength variation against different exposure [108]

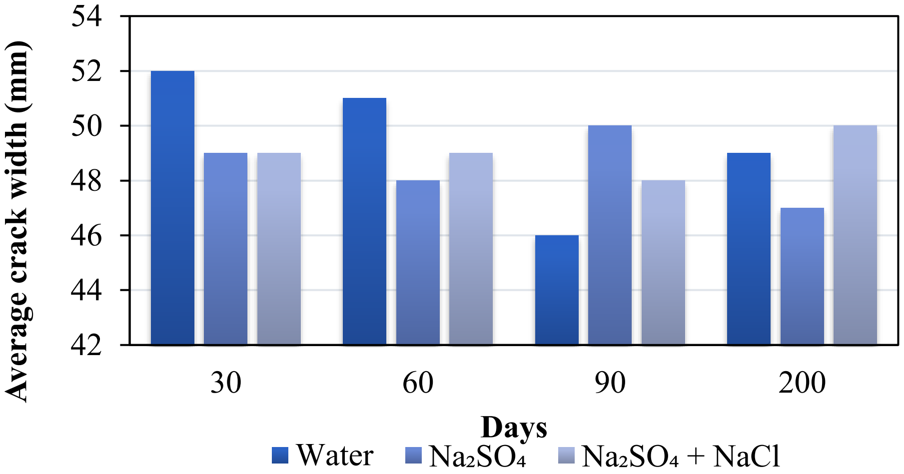

Figure 8: Variation of average crack width (mm) in different exposure conditions against exposure days [108]

In addition, also observed a small degree decrease in the number and width of cracks which seems to be a merit for sustaining durability performance, as it is seen in Figure 8 [108]. It was observed that ECC exhibited comparable self-repair capabilities in a high-chloride environment [114], [115].

Furthermore, it experienced a reduction in the initial crack and a reduction in the bond strength of fibers and the matrix interactions. This is because of the toughness of the matrix, the friction at the interface, and the chemical bonds degrade [116]. Unlike plain cement mortar, where the effective diffusion coefficient of chloride ions (Cl^-) increases exponentially with deformity, ECC shows a linear increase. Moreover, ECC consistently demonstrates a significantly lower diffusion coefficient of Cl^{-1} compared to normal mortar, regardless of pre-loaded deformation [115]. The durability of hybrid fiber ECC in salt conditions of sulfate and chloride has improved compressive strength compared to normal ECC [108].

2.6.2 High-Temperature Resistance

Concrete in extreme temperatures experiences a peeling effect of fragments from its surface, which is due to the release of internal tensile stress [116]. Elevated temperatures accelerate moisture and ion movement, expediting degradation, particularly in specimens under continuous loads However, when ECC is exposed to high temperatures, the fibers in its matrix play a great role in supporting and overcoming the vapor pressure formed during high temperatures, thus preventing spalling from occurring in the form of melting [117]. As temperature increases in ECC, the compressive strength and stiffness decrease. This occurs due to inert particles losing stiffness when temperatures elevate [118]. At a moderate temperature of below or equal to 100°C, high-volume fly ash (HVFA) -ECC exhibits tensile properties and retains good residual tensile ductility by maintaining its unique characteristics of multiple cracking and pseudo-strain hardening, but indicates a decrease after exposure to about 200°C [108]. At a temperature of 150°C SHCC appeared to be deformed with broken fibers multiple cracks and loss of ductility due to a decrease in fiber strength [119]. When PVA-ECC and Hybrid-ECC, incorporating both PVA and steel fibers, were examined, it was noted that ECC exhibited brittleness at elevated temperatures, while Hybrid-ECC displayed deflection and softening tendencies [120]. Between 200°C and 600°C, Hybrid ECCs generated less debris compared to ECCs under uniaxial compression [120]. In flexural tests, Hybrid-ECC demonstrated superior load-bearing capacity and deflection resistance up to 100°C in contrast to ECC [120]. In ECC with glass fiber-reinforced polymer (GFRP) bars (vinyl ester-based), tensile strengths were reduced to 0.889 (at room temperature) as well as to 0.873 (at 40 degrees Celsius) after 180 days without continuous loads [121]. In contrast, specimens under continuous loads experienced more pronounced decreases, with tensile strengths declining to 80.2% (at room temperature) and 67.5% (at 40 degrees Celsius) [121].

2.6.3 Frost Resistance

Low temperature is among the environmental elements that lead to influencing the behavior of concrete composite, whereas in regions with severe cold, composite structures often experience the combined impact of fatigue loading and cycles of freezing and thawing [122]. Internal pore distribution in concrete contributes to the capacity of concrete to withstand frost, where the increase in pore lowers the frost resistance [116]. In ECC, the pore fraction is contributed by fiber volume content, thus making the ECC have more pore fraction than the plain concrete [123]**.** ECC is capable of improving its frost resistance by producing micro-cracks that release internal water expansion stress [116]. It was observed that subjecting ECC to 200 circulations of freezing and thawing has minimum effects on the tensile strength [124]. The longevity of ECC was assessed by measuring weight loss after multiple freeze-thaw cycles. Results indicate a substantial increase in weight loss across all specimens with each additional cycle, highlighting the damaging impacts of salt freezing-thawing repetitions on ECC. PVA – ECC had less tensile strain capacity response when compared to PE-ECC after 200 cycles of freezing-thawing. Reinforced PP-ECC beams were exposed to freezing-thawing cycles and constant flexural load and observed that the failure mode remained consistent over various damage conditions, indicating good ductility. However, continuous freeze-thaw cycles led to increased beam damage, with more cracks, reduced cracking strength, and wider cracks [125]. Frost resistance was noted to be improved by adding silica fume and slag [17]. In a study to enhance the resistance of ECC against frost with high fly ash (FA) content by volume through the addition of silica fume (SF) and GBBS in ECC with 0.30 FA and 0.40 SF exhibited superior frost as proven by mass loss and toughness changes during freeze-thaw cycles. Additionally, ECC with 65% FA and 5% SF demonstrated greater frost resistance than ECC with 70% FA and suggested that an increase in the amount of FA contributes to the enhanced toughness of ECC [17]. It was also noted that ECC mixed with fly ash showed an increase of three times maximum deflection, and its toughness increased after 200 freeze-thaw cycles, demonstrating high deformability [17]. After 50 freeze-thaw cycles of ECC with a large amount of fly ash by volume deicing salt, it experienced less damage on its surface and mass loss as compared to an ordinary motor, and its tensile strain capacity of more than 0.03 was maintained. In addition, the pre-loaded strain of

0.02 was tested in 50 salt freezing cycles, it portrayed self-healing characteristics by restoring its stiffness [126]. The self-healing quality of ECC was observed when pre-loaded tensile stress was (0.005 to 0.01), with a full recovery of approximately 100%. But the pre-loading strain stress increases from 1.5% to 2% and higher than 2.5%, its recovery rate due to self-healing is not predictable. Therefore, the tensile property of ECC decreases as preloading increases [127]. The frost resistance of ECC as subjected to different solutions of sodium sulphate (Na_2SO_4), magnesium sulphate ($MgSO_4$), and water, revealed that its resistance in $MgSO_4$ solution is greater than in Na_2SO_4 solution, and also Na_2SO_4 solution is greater than in water [128].

2.6.4 Carbonization Resistance

Carbonization of cementitious material occurs when CO_2 penetrates its matrix, causing a decrease in pH and increasing the corrosion of the rebars [129]. The extent of this effect is characterized by the depth of penetration, which is associated with the presence of pores and how they are distributed within the ECC matrix [130]. Carbonization resistance in ECC was better in comparison to ordinary concrete [131] because the percentage of the pores is less, and it has a very dense and packed matrix structure [132]. Moreover, the inclusion of fibers for ECC in the tested specimen led to a sealed internal structure, enhancing its resistance to carbonation, which caused the specimen reinforced with steel fiber to exhibit the strongest resistance compared to all other samples [133]. The carbonation depth of ECC beyond 28 curing days in a 20 ± 3% CO_2 environment was shallow, measuring only 0.8 mm, significantly less than plain concrete [134]. As the carbonization curing time increased, ECC's direct tensile strength improved with a reduction in its tensile strain capacity [135]. Meanwhile, ECC cured without carbonization showed higher tensile strain capacity at 7 days compared to ECC cured in an accelerated carbonized environment [136]. This is also seen through Figure 9, as curing time increases, the carbonation depth decreases [137].

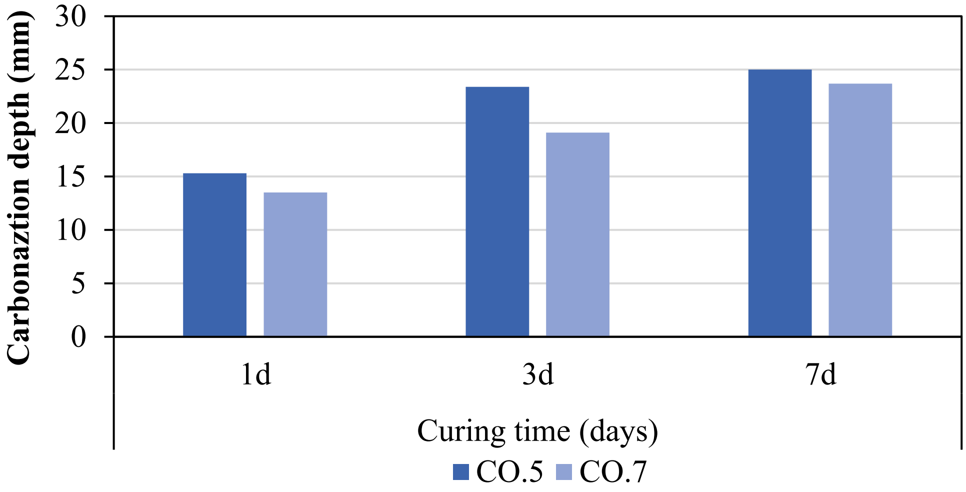

Figure 9: Carbonation depth against curing time (days) [137]

Additionally, PP-ECC containing 2 vol% was shown to have a carbonation depth of 0.8 mm on carbonation tests, which encapsulates a higher level of carbonation durability and provides a good shield for rebar in long-term use [90]. The carbonation resistance of the ECC increased exponentially, to started decreasing as it was observed in PVA fiber with 6mm length and 0.75% fiber content, and showed the strongest carbonation resistance by having very low carbonation depth [138]. Moreover, the average carbonation depth of PVA-ECC decreased degree was noted to be 9% to 20% in 3 days to 28 days [139]. ECC samples demonstrated resistance to carbonation with an increase in LPS as the amount of LPS increased in all ECC mix samples [130]. Furthermore, the value of the carbonation rate coefficient was determined by utilizing Equation 4 for carbonation prediction to gauge the pace at which carbonation advances.

$$C = A\sqrt{tc} \tag{4}$$

Cd =Carbonation depth (mm)

A = Carbonation coefficient rate,

tc = Elapsed carbonation time (days)

Figure 10 shows that the carbonation rate for sample spacemen proceeded at a slower pace, with less depth compared to the plain samples.

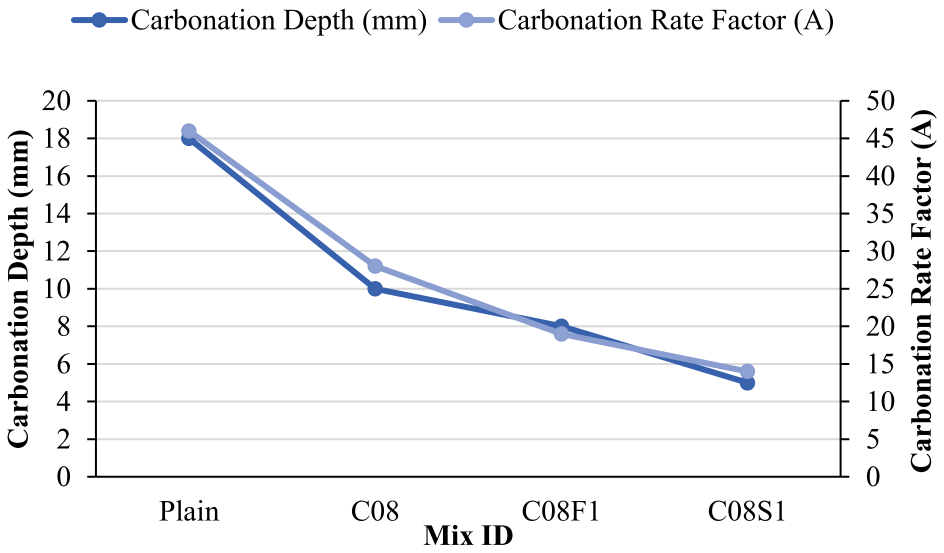

Figure 10: Acceleration Carbonation test results under varying fiber content [130]

2.6.5 Water Permeability

Deterioration in concrete has a close correlation with obstruction of the flow of substances, typically fluids, through it. The concrete permeability is driven by internal pore connectivity, crack depth, and crack width. The effect of permeability is little on concrete for the crack with a displacement of less than 50 microns under loading, while for the crack displacement of between 50 and 200 microns, permeability increases rapidly [140]. ECC with a tighter crack width is more desirable for its low permeability property and for enhancing the durability of its performance [141]. ECC has shown remarkable capability in externally controlling cracks, of less than 100 µm in width [22]. It takes 3 to 4 days for ECC to allow permeability to stabilize with a crack width of <60 mm, and for a crack width of more than 100 mm, it needs 7–10 days [142]. The ECC's relative water permeability was seen to decrease beyond 10 wetting-drying cycles to 0 in the water permeability test, as a result of self-healing of ECC in water [78]. ECC's self-healing effect led to the establishment of an exponential function that shows the variation in permeability [104], [143]. Crack pattern and crack width are vital in the discussion concerning the permeability of cracked ECC. The tighter crack width of CR-ECC showed a tremendously lower permeability compared to N-ECC when subjected when exposed to the same tensile strain, regardless of showing an elevated value of permeability when it is uncracked [104]. Permeability was observed to decrease when FA was used in green lightweight engineered cementitious composites (GLECC) [144].

2.6.6 Abrasion Resistance

The durability of ECC is often gauged by its resistance to abrasion. Coarse aggregates typically enhance abrasion resistance in regular concrete, while in ECC, this resistance primarily relies on the matrix's performance and the capacity of fibers to bind [116]. ECC’s hydro-abrasive resistance test with the PP and PVA fibers was conducted to improve abrasive resistance, and it indicated that with an increase in fiber content by volume from 0% to 2%, the abrasive resistance increased. Also, the experiment revealed that an increase in the curing time results in increased abrasion resistance [145]. Moreover, the abrasion resistance was seen to be affected by the angle at which the hydraulic factor causing abrasion takes place [145]. A study on ECC abrasion resistance with varying the PVA fiber content indicated that a 3% fiber content in volume provides the best abrasion resistance, but as the fiber content was increased, the abrasion resistance decreased [123]. Based on a 2% PVA mix, the impact of covering ordinary concrete, and the abstraction weight loss decreased with an increase in the curing age from 3 days to 28 days [146].

2.6.7 Fatigue Characteristics

Fatigue in concrete structures is part of durability characteristics, as it is experienced when subjected to a prolonged time in different loading conditions, creating cracks that reduce the lifetime of the concrete structure [147]. ECC’s fatigue life is longer than that of normal concrete in the same flexural stress due to random fiber orientation [148]. Longevity and fatigue properties are magnified mostly in geo-polymer concrete rather than ordinary concrete. Because fiber-based geopolymer concrete is likely to be subjected to unfavorable, recurrent, long-term loading conditions that include mechanical and temperature fluctuations. Likewise, a geopolymer concrete structure reinforced with fibers [149]. Homogenic in the matrix of geopolymer concrete mix makes it perform better in an increase of fatigue stress [150]. Also, steel fiber reinforced geopolymer concrete, when observed through an SEM fractography, demonstrated a strong adhesive connection between the aggregates and the cement matrix interfacial, indicating improved concrete fatigue performance. [149]. The study revealed that geopolymer concrete had less strain enhancement compared to ordinary Portland concrete when subjected to an equal amount of repeated axial compression load [151]. As fatigue stress increases, the strain hardening characteristic of ECC also increases, while its strain capacity decreases. The stress intensity factor $\Delta K_{\text{crak tip}}$ at the crack tip, which is calculated by taking into account external loading and fiber bridging stress, determines how quickly a flexural fracture grows.[152]. Fracture mechanics concerning a fiber matrix bond-slip model may be used to predict and compute the crack propagation of ECC under flexural fatigue and flexural fatigue limit. The following Equations 5 and 6 highlight the relationship that exists between the fatigue crack propagation rate and $\Delta K_{\text{crak tip}}$ [20].

$$\frac{D_a}{d_N} = C * \Delta K^{m}_{\text{crack tip}} \tag{5}$$

$$N_L = \int_{a_0}^{a_f+H} \left(\frac{1}{C + \Delta K^{m}_{\text{tip}}}\right) da \tag{6}$$

where N_L is the number of fatigue cycles, an is the fracture length, and c and m are always connected to the matrix's characteristics. A relationship was established between fatigue life against stress level through fatigue tests, and other researchers have also come up with different models, as seen in Table 2, where (S_L signifies stress level and N_L characterizes fatigue life) [153].

Table 2: Models for the connection between stress level and fatigue life

Model	**N_L Range**	**Reference**
Log $S_L = 0.0011 - 0.0165 \lg N_L$	$1 < N_L < 10^4$	[152]
Log $S_L = 0.1974 - 0.0654 \lg N_L$	$N_L \geq$10^4	[152]
$S_L = 1.000 - 0.0226 \lg N_L$	$1 \leq NL < 1x\ 10^4$	[157]
$S_L = 1.595 - 0.1750 \lg N_L$	$1 \times 10^4 \leq N_L \leq 2 \times 10^6$	[111]
$S_L = 1.000 - 0.0320 \lg N_L$	$1 < N_L < 3 \times 10^2$	[111]
$S_L = 1.157 - 0.0903 \lg N_L$	$3 \times 10^2 \leq NL < 2 \times 106$	[111]

The behavior of ECC in terms of its fatigue damage was studied when exposed to fatigue loading after self-healing, and it was observed that the damage level was low due to the rapid healing of ECC [154]. In addition, for load cycles of 600 to 1000, there was a decrease in crack bridging stress at high rates under fatigue loading [155], [156].

2.6.8 Acid Erosion Resistance

Concrete structures used in an environment that is exposed to acidic media like sewages pipes, chemical wastewater treatment plants, mining, and mineral processing production industries has to be able to withstand this kind both to possess the impermeability properties and acid resistance [116]. Acid attacks concrete by affecting the calcium compound which is the hydration product of cementitious materials concrete [116]. ECC's compressive strength sample with nanomaterial with a curing time of 14 days was observed to decrease to almost 8% to 10% when it was put in an acidic solution with a pH of 1 [158]. ECC was used to construct an anti-seepage wall at the mining site whereby in acidic mine drainage the original fracture strength was shown to have decreased by 23%. ultimate tensile strength also reduced to 17.8%, and lastly the tensile strain capacity was reduced to 36% [159]. Increase of lime powder was considered effective in reducing ECC's loss in mass after it was observed ECC sample loss in mass that exceeded 8% when immersed in 3% of the sulphate acid solution for 6 weeks [130].

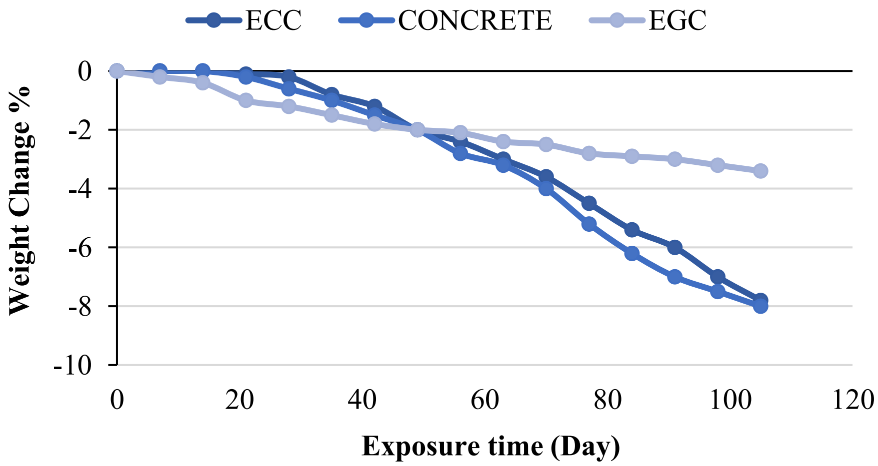

Figure 11: Weight loss variation in percentage for cement concrete, ECC, and EGC when exposed to sulphate acid [160]

Geopolymer matrix and PVA fiber interface (EGC) had less mass loss than the interface of cement matrix and PVA fiber when exposed to sulphate acid attack as it was oobserved the presence of more loose fibers and brushed off in ECC surface than that of EGC surface after the acidic exposure [160]. This is also seen through Figure 11.

2.6.9 Shrinkage Resistance

Concrete shrinkage is among the major causes of concrete structure cracking. Since shrinkage acts on the cementitious material, ECC is more prone to this attack compared to plain concrete because of its high content of cementitious material [116]. It was observed that when comparing the shrinkage strain, ECC and plain concrete after 28 days were 1200 $\mu\varepsilon$ to 1800 $\mu\varepsilon$, respectively [161]. At the high unit of water content, ECC was able to resist shrinkage compared to plain concrete due to coincidentally incorporating expansive agents and a shrinkage-reducing admixture [162]. ECC with less drying shrinkage was developed with a strain capacity of around 0.025 and a shrinkage strain of 109 $\mu\varepsilon$ to 242 $\mu\varepsilon$ over 28 days, which also had good performance in resisting cracks [161]. In a ring pressure test, the surface of low-drying shrinkage ECC was observed to have fewer noticeable cracks compared to traditional ECC, which had multiple cracks on its surface [12]. Admixture, fiber volume, cement content, sand-binder ratio(S/B), water-binder ratio(W/B), and use of zeolite were reported to be contributors to drying shrinkage of ECC, where excessive shrinkage leads to durability problems in the long term [163], [164], [165]. Also, use of fly ash in large quantities causes reduced free drying shrinkage, which is due to the densification of the matrix or the un-hydrated fly ash effects [166].

2.7 Durability Challenges in Cementitious Materials

Cementitious materials, including ECC, face numerous environmental challenges that can compromise their long-term performance. When deicing salts are utilized in maritime settings, chloride ions penetrate concrete and initiate reinforcement corrosion. ECC's tight crack control significantly reduces chloride penetration compared to conventional concrete [46]. Atmospheric CO_2 reacts with calcium hydroxide in the cement paste, reducing alkalinity and potentially compromising reinforcement passivation. Multiple microcracking in ECC can initially accelerate carbonation, though the overall depth remains limited due to the material's self-healing capabilities

[167]. Repeated freezing and thawing can cause progressive deterioration in conventional concrete. ECC exhibits superior freeze-thaw resistance due to its ability to accommodate expansion pressures through microcracking rather than material degradation. Exposure to sulfate-rich environments can lead to expansive reactions and deterioration. ECC formulations with appropriate supplementary cementitious materials show enhanced resistance to external sulfate attack [168].

Beyond environmental factors, mechanical loading presents additional durability challenges. Whereas cyclic loading, common in transportation infrastructure, can lead to progressive damage accumulation [169]. ECC has demonstrated superior fatigue life compared to conventional concrete, with reporting fatigue strain capacities up to 1.5% under appropriate loading conditions [170]. Impact loading, as sudden force application, can cause a brittle failure in conventional concrete. ECC's strain-hardening behavior provides significant impact resistance and energy absorption capacity [171]. The interaction between mechanical loading and environmental exposure often accelerates deterioration. Pre-cracked ECC specimens subjected to combined loading and chloride exposure showed minimal additional deterioration due to the material's tight crack control and self-healing capabilities [172].

2.8 Service Life Considerations

The ultimate measure of durability is service life performance [107]. ECC exhibits remarkable autogenously healing capabilities, with documenting complete healing of microcracks under proper exposure conditions [173]. This self-healing behavior contributes significantly to extended service life. The multiple microcracking behavior of ECC necessitates different inspection protocols compared to conventional concrete. Visual assessment of crack patterns rather than individual crack widths becomes more relevant [53]. A comprehensive evaluation of ECC's environmental impacts over its entire service life has been conducted and despite higher initial embodied energy, ECC's extended service life and reduced maintenance requirements often result in lower life-cycle environmental impacts compared to conventional concrete solutions.

2.9 Summary of the Chapter

This chapter presents a detailed literature review on Engineered Cementitious Composites (ECC), beginning with an overview of ECC and its significance in modern construction. The chapter explores a wide range of ECC applications, highlighting its use in structural repairs, infrastructure resilience, and high-performance buildings. Various approaches to ECC mix design are discussed, along with insights into its fresh properties, such as flowability and setting behaviour. The review further examines ECC's mechanical characteristics, emphasizing its tensile strain capacity and crack control. A major focus is placed on durability properties, including resistance to salt corrosion, high temperatures, frost, carbonation, water permeability, abrasion, fatigue, acid attack, and shrinkage. These properties are analysed through previous research findings to understand ECC's long-term performance under diverse environmental conditions. The chapter concludes with a critical discussion on the broader durability challenges in cementitious materials and outlines key considerations related to the service life and sustainability of ECC in aggressive environments.

CHAPTER 3

MATERIALS AND METHODOLOGY

3.1 General

This chapter outlines the properties of the materials used in the investigation, including cement, fine aggregates, fly ash, sugarcane bagasse ash, water, superplasticizer, and polyvinyl alcohol (PVA) fiber. It also details the mix proportions employed in the study. Furthermore, the chapter provides a comprehensive description of the experimental setup, including specimen preparation, adopted methodologies, and methods for assessing fresh, mechanical and durability properties such as mini slump, compressive strength, direct tensile strength, flexural strength, water absorption, water permeability, sulphate and chloride attack, Rapid Chloride Penetration Test and finally validated the best mechanical characteristic results with Finite Element Method using ABAQUS.

3.2 Materials

This section provides the physical and chemical properties of the materials utilized in the research, including Ordinary Portland Cement (OPC), Fly Ash (FA), Sugarcane Bagasse Ash (SCBA), River Sand (RS), Manufactured Sand (M-Sand), polyvinyl alcohol (PVA) fibers, water, and a high-range water-reducing (HRWR) admixture.

3.2.1 Cement

Cement serves as the primary binding agent in composites, holding together the solid constituents. In this study, OPC of 43 Grade, supplied by UltraTech Cement Ltd. and conforming to IS 8112:1989, was utilized.

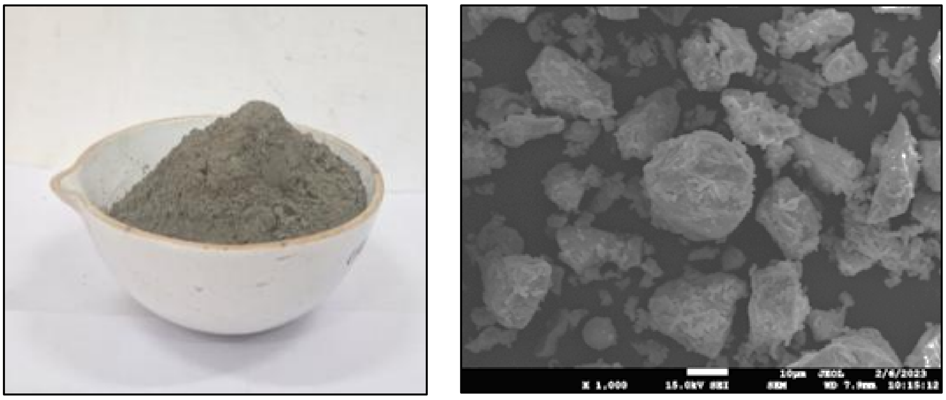

(a) Cement *(b) SEM Image of Cement*

Figure 12: Cement in Physical form and SEM Image of Cement

Figure 12 (a) depicts the cement in its raw form along and 12 (b) microstructure under a Scanning Electron Microscope (SEM). Figure 13 (a) shows Specific Gravity Test, and 3 (b) Consistency Test, 13 (c) Soundness Test, 13 (d) preparation of cement mortar specimens, 13 (e) curing in a water bath, and 13 (f) compression testing process,

(a) Specific Gravity Test *(b) Consistency Test*

(c) Soundness Test *(d) Cement Mortar Specimen*

(e) Curing of the Cement Mortar Specimens in water bath *(f) Compression Testing of Cement Mortar Specimen*

Figure 13:Tests of Cement

Cement particles exhibit an irregular shape with an average particle diameter of 20 ± 5 μm and a relatively smooth surface texture, as observed from SEM images. The physical properties and determined in accordance with IS 4031:1988 and Energy-dispersive X-ray spectroscopy (EDS) results for chemical composition are shown in Table 3 and Table 4, respectively.

Table 3: Physical Properties of the Cement

Physical Properties	**Cement**	**Limits as per 8112:1989**
Specific gravity	3.10	-
Fineness by Sieving (%)	6.75	10
Soundness (mm)	1.6	10 mm max.
Bulk Density (kg/m^3)	1440	-
Standard consistency (%)	33	-
Initial setting time (minute)	100	30 minutes min.
Final setting time (minute)	340	600 minutes max.
Soundness (mm)	2	10 mm max.
Compressive Strength (N/mm^2), 28 Days	46.32 N/mm^2	43 N/mm^2 min. 58 N/mm^2 max.

Table 4: Chemical Composition of the Cement

Chemical Composition	**Cement**
Aluminum oxide, Al_2O_3	4.11%
Silicon oxide, SiO_2	23.44%
Calcium oxide, CaO	62.12%
Ferric oxide, Fe_2O_3	3.92%
Magnesium oxide, MgO	3.42%
Titanium dioxide, TiO_2	0.62%
Potassium oxide, K_2O	0.54%
Sodium oxide, Na_2O	0.21%
Others	1.63%

3.2.2 River Sand and Manufactured Sand

Locally available river sand (RS) sourced from the Sutlej River was used in this study, while manufactured sand (M-Sand) was obtained from a crusher plant in Pathankot.

Both sands were sieved through a 4.75 mm sieve and retained on a 150-micron sieve. Figures 14 and 15 illustrate the physical appearance of RS and M-Sand, respectively. The fine aggregates were tested in accordance with IS: 2386 – 1963. Figure 16 presents the specific gravity test, and Figure 17 displays the sieve analysis test.

Figure 14: River Sand

Figure 15: Manufactured Sand

Figure 16: Specific Gravity Test

Figure 17: Sieve Analysis Test

Sieve analysis was conducted to determine the particle size distribution curves of RS and M-Sand, as given in Figure 18.

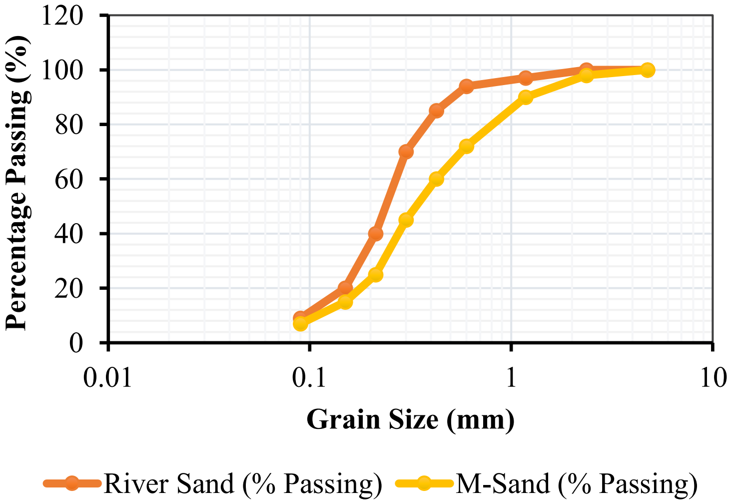

Figure 18: Particle Size Distribution of RS and M-Sand

Based on the results, RS falls under grading Zone 4, while M-Sand corresponds to grading Zone 2 as per IS: 383 – 1970. Zone IV RS was selected because its finer particle size distribution ensures better matrix homogeneity and uniform PVA fiber dispersion, which are essential for achieving strain-hardening behavior in Engineered Cementitious Composites. The physical properties of RS and M-Sand are summarized in Table 5.

Table 5: Physical Properties of RS and M-Sand

Physical Properties	**River Sand**	**Manufactured Sand**
Specific gravity	2.66	2.83
Bulk Density (kg/m^3)	1520.40	1740.70
Water Absorption (%)	1.8	2.3
Fineness Modulus	2.49	2.85

3.2.3 Fly Ash

Powdered fly ash was purchased from Nabha Power Limited (NPL), located near Rajpura, Punjab. Table 6 provides specifics on its chemical composition as determined by energy-dispersive X-ray spectroscopy (EDS).

Table 6: Chemical Composition of the Fly Ash

Chemical Composition	**Fly Ash**	**Limits as per IS 3812 (Part 1) :2003**
Aluminum oxide, Al_2O_3	21.23%	-
Silicon oxide, SiO_2	60.11%	35% minimum
Calcium oxide, CaO	3.06%	-
Ferric oxide, Fe_2O_3	4.54%	-
Magnesium oxide, MgO	3.87%	5% maximum
Titanium dioxide, TiO_2	0.89%	-
Potassium oxide, K_2O	0.98%	-
Sodium oxide, Na_2O	0.79%	1.5% maximum
Others LOI	4.33%	5% maximum

Based on the results, the fly ash meets the specifications for Grade I Siliceous Pulverized Fuel Ash as per IS 3812 (Part 1): 2003. The combined proportion of SiO_2, Al_2O_3, and Fe_2O_3 is 85.88%, which surpasses the minimum requirement of 70%.

Moreover, the SiO_2 content alone is 60.11%, exceeding the specified minimum of 35%, and the Loss on Ignition (LOI) is 4.33%, remaining within the allowable limit of 5%.

Figure 19 (a) illustrates the physical appearance of the fly ash and Figure 19 (b) shows Scanning Electron Microscope (SEM) image and it is observed from the SEM image that Fly ash particles are predominantly spherical in shape with a smooth surface texture and an average particle diameter of 10 ± 3 µm,. The specific gravity and bulk density were found to be 2.45 and 1280.80 kg/m³, respectively. The specific gravity test setup is depicted in Figure 20.

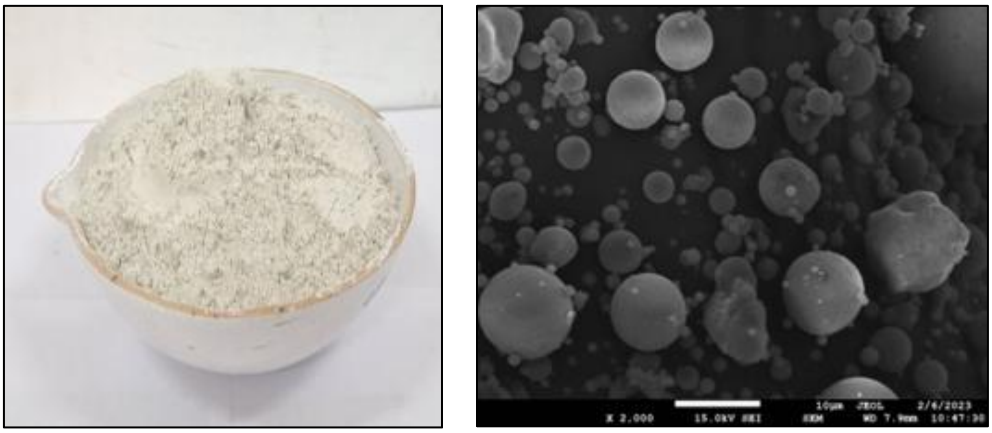

(a) Fly Ash

(b) SEM Image of Fly Ash

Figure 19: Fly Ash in Physical form and SEM Image of Fly Ash

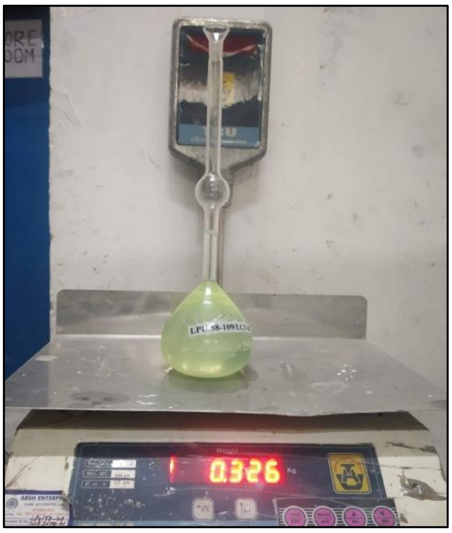

Figure 20: Specific Gravity Test of Fly Ash

3.2.4 Sugarcane Bagasse Ash

The SCBA was acquired in flake form from Golden Sandhar Sugars Limited, Phagwara, Punjab, and processed into a fine powder as shown in the Figure 21 [174].

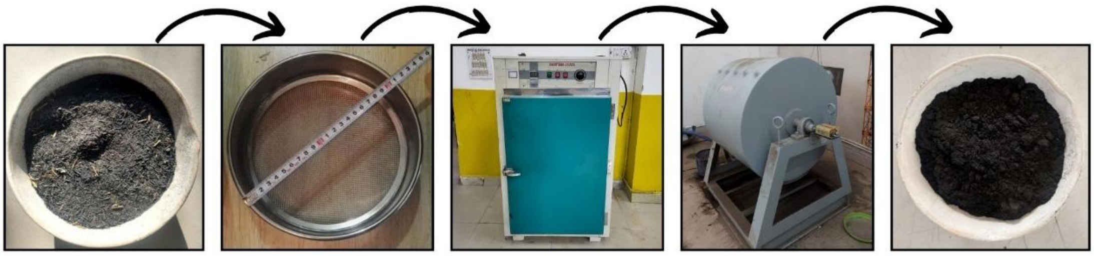

(a) Raw Flakes of Sugarcane Bagasse Ash *(b) Removing unwanted material by sieving* (c) *Oven-drying the sieved material at 120°C for 24 hours* *(d) Ball milling the dried Sugarcane Bagasse Ash for 6 hours* (e) *Treated Sugarcane Bagasse Ash*

Figure 21: Steps followed for the treatment of the Sugarcane Bagasse Ash

The treatment process of SCBA involves several steps to enhance its suitability for use in cementitious composites. Initially, raw SCBA in flaky form is collected and subjected to a sieving process to eliminate coarse, unwanted particles and organic matter. The sieved material is then oven-dried at a temperature of 120°C for 24 hours to remove any remaining moisture. Once dried, the SCBA is further refined by ball milling for a duration of six hours to achieve a finer and more uniform particle size.

This processed ash, now termed as treated SCBA, exhibits improved pozzolanic properties and is suitable for incorporation into cementitious materials. The sequence of this treatment ensures better reactivity, consistency, and compatibility when used as a supplementary cementitious material. Figure 22 is representing the treated SCBA and it’s SEM. Sugarcane bagasse ash particles exhibit an irregular shape with a rough surface texture and an average particle diameter of 50 ± 5 µm, as observed from SEM images.

(a) Sugarcane Bagasse ash *(b) SEM of Sugarcane Bagasse ash*

Figure 22: Sugarcane Bagasse Ash in Physical form and SEM Image of Sugarcane Bagasse Ash

The chemical composition of SCBA as measured by energy-dispersive X-ray spectroscopy (EDS) is shown in Table 7.

Table 7: Chemical composition of Sugarcane Bagasse Ash

Chemical Composition	Sugarcane Bagasse Ash
Aluminum oxide, Al_2O_3	15.88%
Silicon oxide, SiO_2	59.91%
Calcium oxide, CaO	3.09%
Ferric oxide, Fe_2O_3	11.87%
Magnesium oxide, MgO	3.04%
Titanium dioxide, TiO_2	1.87%
Potassium oxide, K_2O	2.69%
Sodium oxide, Na_2O	0.57%
Others LOI	1.08%

Due to the non-availability of particle size analysis facilities at the time of experimentation, quantitative particle size distribution of Fly Ash and Sugarcane Bagasse Ash could not be determined in this study. Instead, Scanning Electron Microscopy (SEM) was used to qualitatively assess particle morphology and relative fineness, which showed predominantly spherical FA particles and irregular, porous SCBA particles. These qualitative observations were supported by particle size distribution ranges reported in the literature for similar materials and were used to interpret the influence of FA and SCBA on the fresh and hardened properties of the ECC mixtures

3.2.5 Polyvinyl Alcohol Fiber

Polyvinyl Alcohol (PVA) fibers were procured from a Chennai-based trading firm, Fiber Region. Known for their excellent tensile ductility, PVA fibers with a length of 12 mm are considered optimal for high-performance ECC applications [27], [61]. Since the binder composition in this study is similar to that used in previous research, 12 mm fibers were selected to maintain consistency. Furthermore, the fibers were used in their original form without any surface pre-treatment to improve bonding characteristics. The physical properties of PVA fibers provided by the manufacturer Fiber Region are given in Table 8. Figure 23 (a) and Figure 23 (b) represents the PVA Fibers and SEM of PVA Fibers.

Table 8: Physical Properties of PVA Fibers

Properties	**Value**
Tensile Strength	1600 MPa
Diameter	40 µm
Fiber Length	12 mm
Aspect Ratio	300
Young’s Modulus	40 GPa
Elongation	5 %
Density	1300 kg/m^3

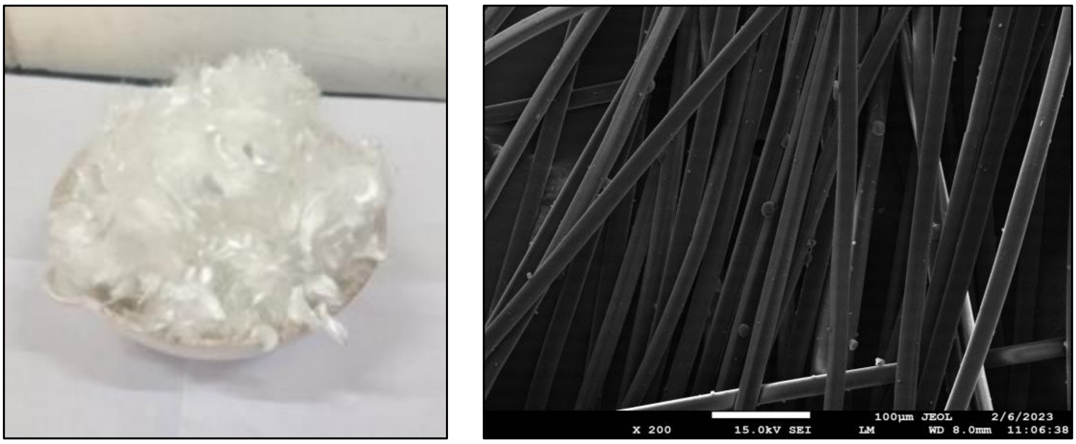

(a) PVA Fibers *(b) SEM of PVA Fibers*

Figure 23: PVA Fibers and SEM of PVA Fibers

3.2.6 Water

A basic ingredient in cementitious composites, water is essential to the hydration process and the synthesis of cement gel, both of which support the formation of strength. In this investigation, all mixing and preparation were done with potable water.

3.2.7 Superplasticizer

To ensure adequate workability of the mixtures in this investigation, a superplasticizer (SP) based on polycarboxylate ether was employed. The superplasticizer employed was Auramix 400, which complies with the specifications of IS 9103:1999, and was procured from FORSOC. Figure 24 is showing the superplasticizer Auramix 400.

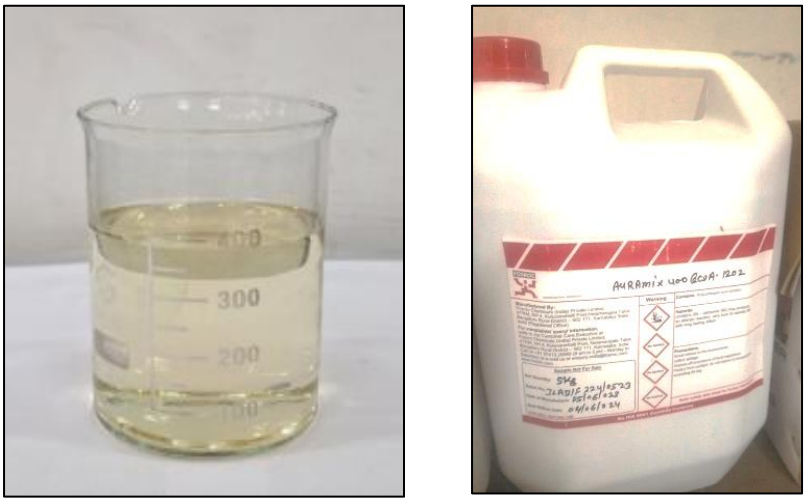

(a) Superplasticizer *(b) Packing of the superplasticizer*

Figure 24:Superplasticizer Auramix400

Table 9 contains the properties of the superplasticizer, which were provided by the manufacturer, FORSOC.

Table 9:Properties of Super-Plasticizer

Properties	Value
Aappearance	Light yellow coloured liquid
pH Value	6.0
Volumetric mass @ 20 degree C	1.09 kg/litre
Alkali Content	1.5 g Na_2O / liter

3.3 Research Framework

The research began with a comprehensive literature review to identify the current advancements and existing gaps in the field of ECC. To address the challenges faced by the modern construction industry and environmental concerns, appropriate materials mentioned in section 3.1 were selected, and their physical and chemical properties were thoroughly characterized.

In the absence of standardized design codes for ECC, several trial mixes were developed based on insights from existing literature to achieve the desired control mix performance. The trials were performed in two categories: the first FA based ECC and the second SCBA based ECC.

Particular focus was placed on evaluating the flowability, compressive strength, and direct tensile strength of the matrix during these trials and one control mix for each FA based ECC and the second SCBA based ECC was finalized, which marked the completion of the first objective of the study.

Following this, fresh property tests were conducted to assess the workability and uniformity of the mix. Subsequently, specimens were cast for twelve different mixes by replacing river sand with M-Sand for further evaluation.

These specimens were subjected to mechanical and durability tests to examine their strength, ductility, and resistance to environmental influences and this level marked the completion of the second objective of the study. The results obtained were then validated using

Finite Element Analysis (FEA) through ABAQUS, ensuring the accuracy and consistency of the mechanical performance via numerical modeling. Ultimately, the research concluded with the development of a final product that incorporates the optimized properties and fulfills the intended structural requirements. The entire workflow of the study is illustrated in Figure 25.

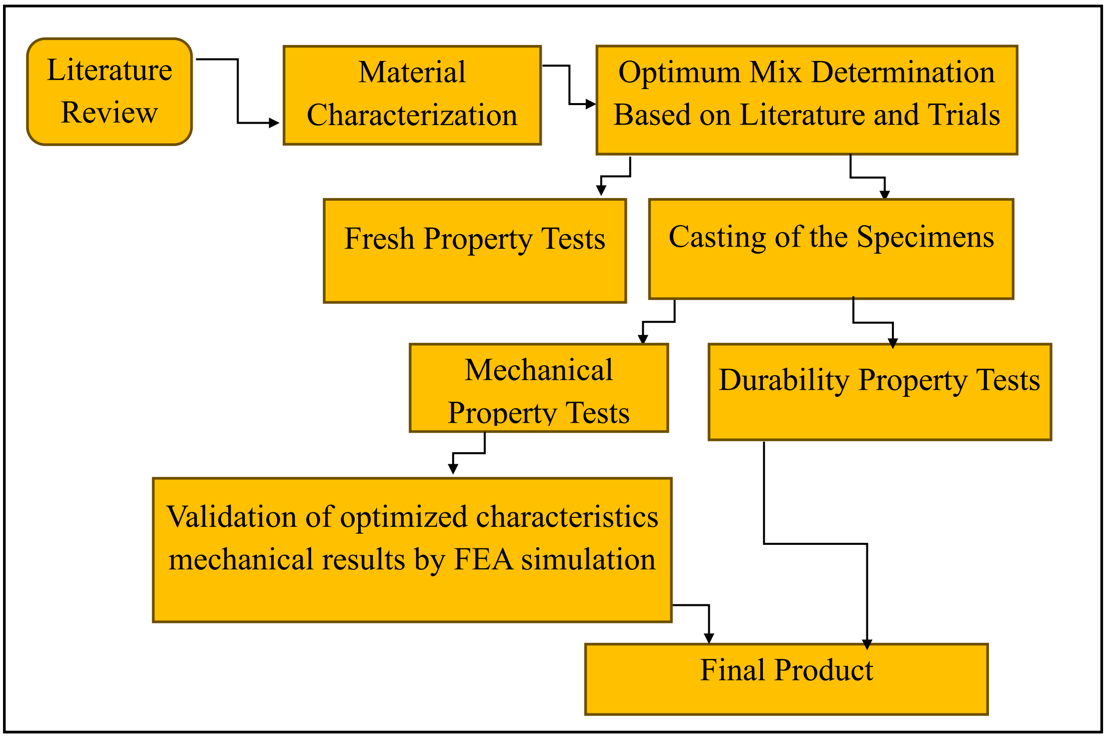

Figure 25: Framework of the Study

3.4 Trials and Control Mixes

The control mix for ECC was developed to optimize fresh, mechanical and durability properties. Two different set of trials were run: in the first group of the trails fly ash was used as the supplementary cementitious materials and in the second, sugarcane bagasse ash. The mix incorporated water to binder (w/b) ratio from 0.27 to 0.30, sand to binder (s/b) ration from 0.40 to 0.60, and superplasticizer to binder (sp/b) ratio from 0.01 to 0.02 with Ordinary Portland Cement at 480 kg/m^3, fly ash at 512 kg/m^3, and sugarcane Bagasse ash at 192 kg/m^3. The combination of cement and supplementary cementitious materials was considered as binder. Multiple trial mixes were prepared, and their performance was evaluated based on flowability, and 28 days compressive and direct tensile strength. The mix that exhibited optimal performance across these parameters was selected as the control mix, as detailed in Table10 and Table 11.

Table 10:Control design mix with FA as SCM

MIX ID	w/b	s/b	SP/b (%)	PC (Kg/m^3)	FA (Kg/m^3)	RS (Kg/m^3)	PVA (Kg/m^3)	Water (Kg/m^3)	SP (Kg/m^3)
FA-MS0	0.27	0.40	0.01	480	512	405	26	268	9.92

Table 11: Control design mix with SCBA as SCM

MIX ID	w/b	s/b	SP/b (%)	PC (Kg/m³)	SCBA (Kg/m³)	RS (Kg/m³)	PVA (Kg/m³)	Water (Kg/m³)	SP (Kg/m³)
SCBA-MS0	0.29	0.60	0.02	480	194	405	26	195	13.48

The ECC mix designs used in this study are presented in Table 12, where RS was replaced with M-Sand at varying levels of 0%, 20%, 40%, 60%, 80%, and 100% on a volume basis to account for differences in particle shape and bulk density between the two fine aggregates.

Table 12: Details of the Mix IDs and M-Sand Replacements

Mix Types	Mix ID	River Sand Replacement with M-Sand
Group I: Fly Ash Based ECC Mixes	FA-MS0	RS substitution with M-Sand at 0%
	FA-MS20	RS substitution with M-Sand at 20%
	FA-MS40	RS substitution with M-Sand at 40%
	FA-MS60	RS substitution with M-Sand at 60%
	FA-MS80	RS substitution with M-Sand at 80%
	FA-MS100	RS substitution with M-Sand at 100%
Group II: Sugarcane Bagasse Ash based ECC Mixes	SCBA-MS0	RS substitution with M-Sand at 0%
	SCBA-MS20	RS substitution with M-Sand at 20%
	SCBA-MS40	RS substitution with M-Sand at 40%
	SCBA-MS60	RS substitution with M-Sand at 60%
	SCBA-MS80	RS substitution with M-Sand at 80%
	SCBA-MS100	RS substitution with M-Sand at 100%

Table 13 provides the detailed mix proportions in kg/m³. The mixes labeled FA-MS0 and SCBA-MS0 serve as the reference mixes, containing no M-Sand and using only RS as the fine aggregate.

Table 13: Mix proportions of all 12 ECC mixes

Mix ID	**w/b**	**RS/b**	**MS/b**	**SP/b (%)**	**Cement (Kg/m^3)**	**Fly Ash/ SCBA (Kg/m^3)**	**River Sand (Kg/m^3)**	**M-Sand (Kg/m^3)**	**PVA (Kg/m^3)**	**Water (Kg/m^3)**	**SP (Kg/m^3)**
FA-MS0	0.27	0.40	0.00	0.01	480	512	405	00	26	268	9.92
FA-MS20	0.27	0.32	0.08	0.01	480	512	324	93	26	268	9.92
FA-MS40	0.27	0.24	0.16	0.01	480	512	243	186	26	268	9.92
FA-MS60	0.27	0.16	0.24	0.01	480	512	162	278	26	268	9.92
FA-MS80	0.27	0.08	0.32	0.01	480	512	81	371	26	268	9.92
FA-MS100	0.27	0.00	0.40	0.01	480	512	00	464	26	268	9.92
SCBA-MS0	0.29	0.60	0.00	0.02	480	194	405	00	26	195	13.48
SCBA-MS20	0.29	0.48	0.12	0.02	480	194	324	93	26	195	13.48
SCBA-MS40	0.29	0.36	0.24	0.02	480	194	243	186	26	195	13.48
SCBA-MS60	0.29	0.24	0.36	0.02	480	194	162	278	26	195	13.48
SCBA-MS80	0.29	0.12	0.48	0.02	480	194	81	371	26	195	13.48
SCBA-MS100	0.29	0.00	0.60	0.02	480	194	00	464	26	195	13.48

The experimental results in this study were based solely on variations in sand content, while all other mix parameters were held constant. As shown in Table 13, cement was used as the base reference material in the mix ratios at a set dose of 480 kg/m³ across all mixes. However, the supplementary cementitious materials (SCMs), fly ash (FA) in Group I and sugarcane bagasse ash (SCBA) in Group II, were used in varying proportions due to differences in their densities. Specifically, FA in Group I was incorporated at a density of 512 kg/m³, while SCBA in Group II was used at 194 kg/m³. The total binder content in each mix was calculated as the combined amount of cement and the respective SCM. The water-to-binder ratio (w/b) was kept constant to 0.27 in Group I and 0.29 in Group II to ensure uniform hydration and consistent strength development across all mixes. The sand-to-binder ratio (s/b) was systematically adjusted from 0% to 100% at the intervals of 20% in both Group I and Group II, as it significantly influences the packing density, matrix cohesion, and overall mechanical behavior of ECC. Therefore, the base mix in this study was prepared using a proportion of 1 part cement, 1.2 parts FA, and 0.8 parts RS (by weight), represented as 1:1.2:0.8 in the Group I and 1 part cement, 1.2 parts SCBA, and 0.8 parts RS (by weight), represented as 1:1.2:0.8 in the Group II.The dosage of superplasticizer was also kept constant to 0.01 in Group I and 0.02 in Group II to preserve consistent fresh properties such as workability and flowability stability. The PVA fiber content was maintained at a constant level of 2% volume fraction throughout all mixes, enabling a focused investigation into how varying sand proportions affect fresh, hardened and durability performance.

3.5 Mixing and Casting

For the preparation of ECC mixtures, a Rossmann stand mixer with a 5.5-liter capacity and a planetary rotating blade was employed as seen in Figure 26. Before mixing, all constituent materials were accurately weighed according to the batch proportions. A precision electrical scale was used for measuring dry ingredients and fiber content, while a graduated measuring cylinder was used to quantify the liquid admixtures, including the superplasticizer.

Figure 26: Mixer with planetary rotating blade

The mixing process commenced with the dry blending of fine sand and FA or SCBA for 2 minutes. Subsequently, cement was incorporated, and the dry materials were mixed for 3 minutes to confirm uniform dispersion. Following the dry mixing phase, water, and superplasticizer were gradually introduced into the mixer while mixing continued for 3–4 minutes, resulting in a smooth and homogeneous slurry. Once the matrix was well-formed, polyvinyl alcohol (PVA) fibers were slowly added to the mix while the mixer operated at a moderate speed. This step is critical to minimize the risk of fiber agglomeration or balling. Mixing was continued for an additional 3–5 minutes to achieve uniform fiber dispersion throughout the matrix.

For casting, pre-lubricated or coated molds were used to prevent adherence of the material to mold surfaces. The ECC mixture was gently placed into the molds without mechanical vibration, as the material exhibits self-compacting properties. Surface finishing was performed with minimal troweling to avoid disrupting the alignment of fibers, as shown in Figure 27 and Figure 28, freshly casted ECC cubes and coupons for Strength Testing. Apart from them, ECC beams and cylinders were also casted. The specimens were kept ideal for the initial 24-hour setting period. Following demolding, the samples underwent a water curing process for durations of 7, 28, 90 and 180 days, depending on the specific experimental requirements.

Figure 27: Freshly casted ECC cubes

Figure 28: Freshly casted ECC coupons

3.6 Testing Methodology

To comprehensively evaluate the performance of ECC a number of experiments were carried out, categorized into fresh properties, mechanical strength, and durability assessments. Fresh properties were assessed using the Mini Slump Cone Test to evaluate the flowability and workability of the mix. Mechanical strength tests included Compressive Strength, Direct Tensile Strength, and Flexural Strength tests to examine the load-bearing capacity and ductile behavior of ECC. To ensure long-term performance, durability tests such as Water Absorption, Sulphate Attack, Chloride Attack, Rapid Chloride Penetration Test (RCPT), and Water Permeability tests were carried out. Figure 29 is enlisting all the conducted tests. This comprehensive testing regime enabled a detailed analysis of ECC performance in terms of fresh, mechanical and durability behavior.

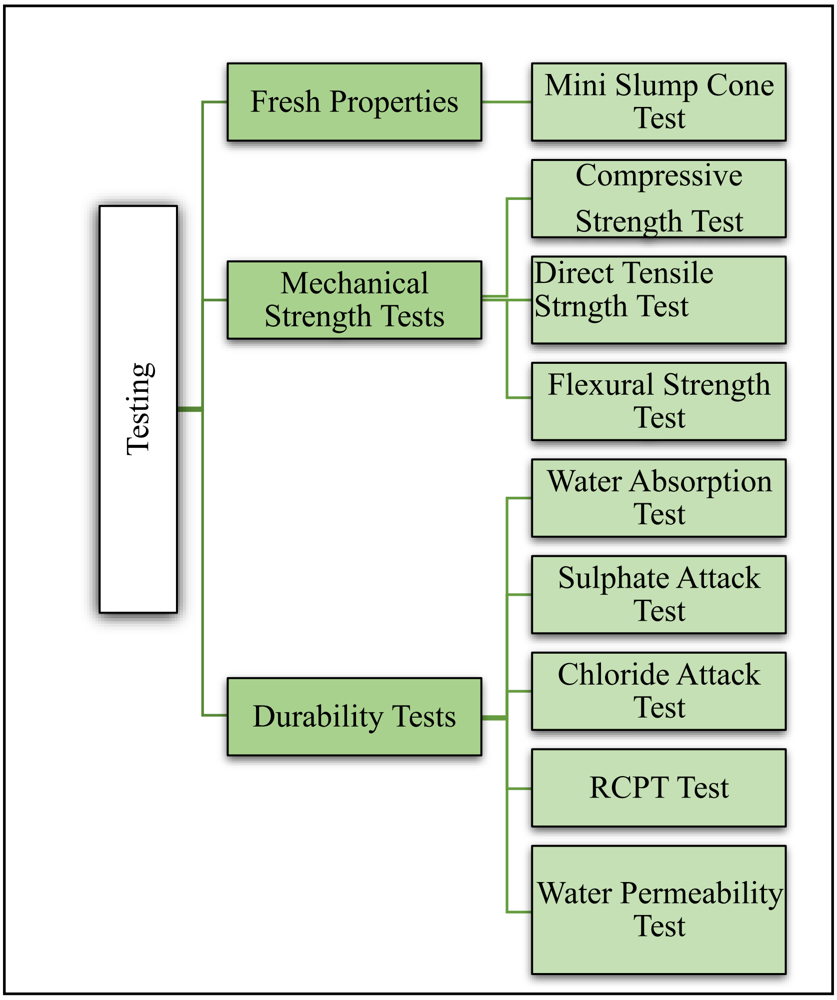

Figure 29: List of the fresh, mechanical and durability tests

3.7 Fresh Properties of ECC

Flowability tests were conducted on the fresh ECC mixes using the mini slump cone shown on the Figure 30 and Figure 31 with 60 mm in height, 70 mm in upper diameter, and 100 mm in lower diameter [176], [177]. Fresh ECC mixture was poured into the cone without consolidation, followed by leveling the surface. The cone is then removed, allowing it to slump under its own weight. The diameter of the flow is measured orthogonally in both perpendicular directions to assess flowability as shown in Figure 32 and Figure 33. For the output, the relative flow was calculated by taking the average of the flow. This test also serves as a visual inspection for segregation, indicated by the separation of the mortar and paste.

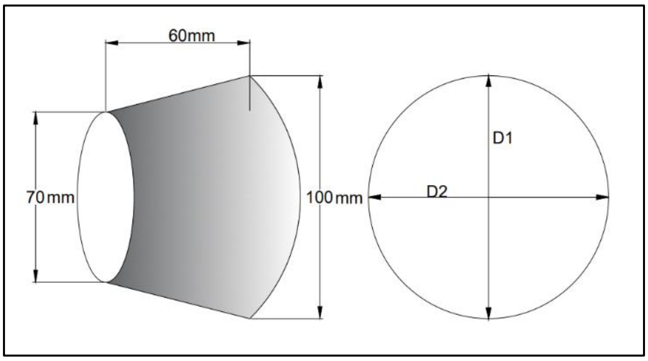

Figure 30: Mini Slimp Cone diagram

Figure 31: Mini Slimp Cone Set-up

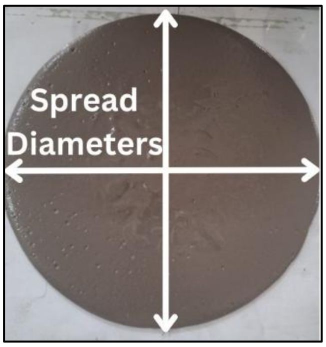

Figure 32: Spread of the Fresh ECC

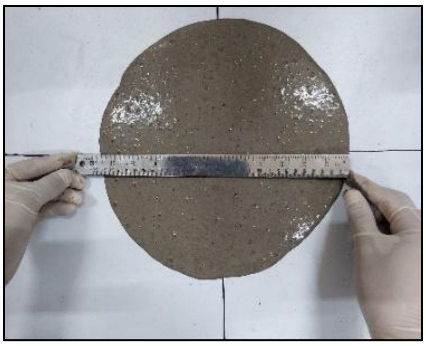

Figure 33: Measuring the Flow of the Fresh ECC

3.8 Mechanical Properties of ECC

3.8.1 Compression Test

Cube specimens of 70.6 mm × 70.6 mm × 70.6 mm were cast and cured in water for 7, 28, and 90 days in order to assess the specimens' compressive strength in accordance with IS 4031-Part 6. [178] (Figure 34 and Figure 35).

Figure 34: Casting of ECC Cubes

Figure 35: Curing of ECC Cubes

Later specimens were removed from water and wiped off surface moisture. The specimens are tested via a universal compressive machine, with a 1000 kN capacity and a 5.15 kN/sec loading rate. (Figure 36).

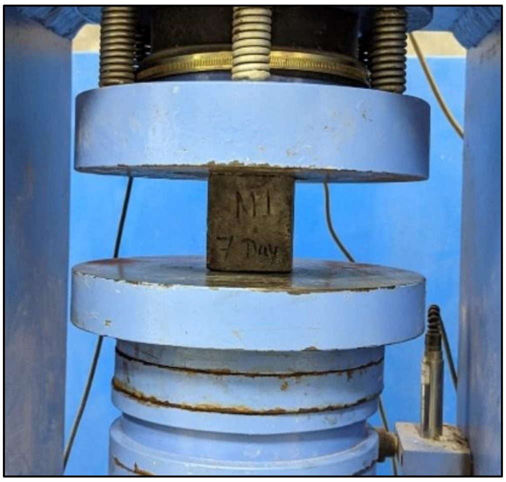

Figure 36: Testing of ECC Cubes

The average of three cubes were adopted at each testing age. The specimen was positioned in the center of the compression testing apparatus's lower platen. Before failure, a load was applied without shock. The highest load was noted, and Equation 7 was used to determine the compressive strength.

$$\text{Compressive strength (MPa)} = \frac{\text{Load}}{\text{Area}} \tag{7}$$

Figure 37 shows the tested specimen subjected to compressive loading. The specimen exhibits ductile failure, as indicated by visible surface microcracks, in contrast to the typical brittle failure observed in conventional concrete.

Figure 37: Cracks on ECC cube after Compression Test

3.8.2 Direct Tensile Strength

The lack of codal recommendations for performing direct tensile strength testing on fiber-reinforced cementitious matrix, the present study adopted testing procedures based on previously published literature. In earlier studies, specimens were typically prepared in dog-bone or coupon shapes. Accordingly, for this research, coupon-shaped specimens measuring 300 mm × 50 mm × 15 mm were used as shown in Figure 38 [25], [179].

Figure 38: Casted ECC Coupons

These samples were water-cured for durations of 7, 28, and 90 days. During testing, each specimen was mounted between grips of a Universal Testing Machine with a 9.8 kN (1000 kg) capacity, with 50 mm of each end held firmly in place (Figure 39 and Figure 40).

Figure 39: Universal Testing Machine

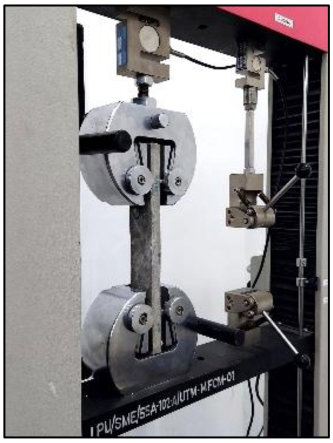

Figure 40: Direct Tensile Testing Set-up

Through the crosshead, a direct tensile stress was given at a steady displacement rate of 0.2 millimeters per minute until the specimen failed. The test setup is illustrated in Figure 41.

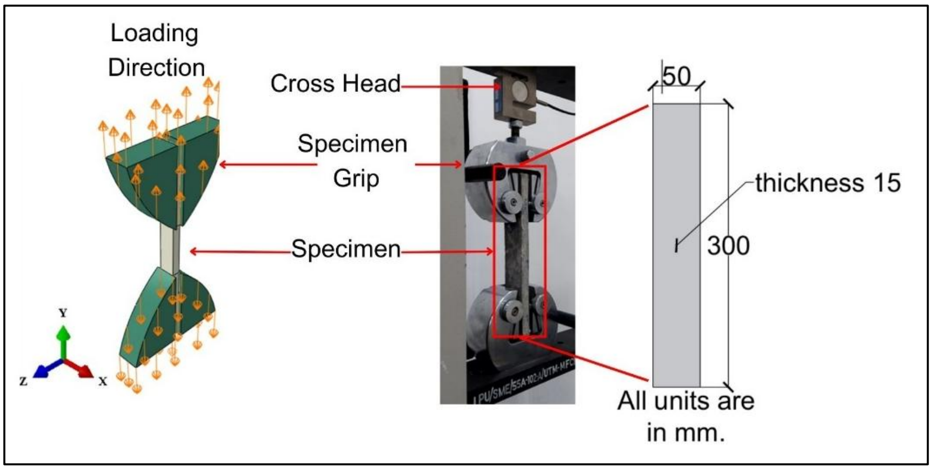

Figure 41: Details of the coupon and Direct Tensile Testing Specimen [175]

The peak load recorded during the test was used to calculate the tensile stress by dividing it by the specimen's cross-sectional area as per Equation 8.

$$\text{Direct Tensile strength (MPa)} = \frac{\text{Load}}{\text{Area}} \tag{8}$$

3.8.3 Flexural Test

Beam specimens of size 100mm × 100mm × 500mm were prepared as per IS 516:1959 for the flexural test at the curing for 7, 28, and 90 days as shown in Figure 42 [180].

Figure 42: ECC casted Beam Specimens

The beam was placed on the flexural testing machine for four-point loading testing with the longitudinal axis of the specimen at right angles to the rollers as per Figure 43 and Figure 44.

Figure 43:Flexural Test Set-up

Figure 44: Flexural Test Set-up

Without shock, a loading rate of 1.8 kN/min was applied. Equation 15 was used to determine the flexural strength once the maximum load was noted.

$$\text{Fkexure Strength (MPa)} = \frac{\text{F} * \text{L} * 10^3}{\text{b} * d^2} \qquad (15)$$

where L is the ECC beam's length (mm), b is its width (mm), d is its depth (mm), and F is the failure load (kN).

3.9 Durability Properties

3.9.1 Water Absorption Test

The water absorption test was performed in accordance with the provisions of ASTM C642-2013 to quantify the percentage of water absorption in hardened ECC. Standard cube specimens of dimensions 70.6 mm × 70.6 mm × 70.6 mm were casted and subjected to curing for 28 days to ensure adequate hydration (Figure 45). Following the curing period, the specimens were oven-dried at a temperature of 105 ± 5°C until a steady mass was attained, indicating the complete removal of free moisture (Figure 46). After drying, the samples were let to cool to room temperature., and the oven-dry mass (M_1) was accurately recorded using a digital balance. Subsequently, the specimens were completely submerged in water maintained for predetermined durations of 28, 90, and 180 days, respectively. After this period, the specimens were removed, gently surface-dried with a damp cloth to remove excess water without drawing moisture from the pores, and the saturated surface-dry mass (M_2) was measured as shown in Figure 47.

Figure 45: ECC Cubes in curing process

Figure 46: ECC Cubes in oven to get dry mass

Figure 47: ECC Cubes on weighing scale to get saturated mass

The water absorption percentage was calculated using Equation 16, which relates the increase in mass due to water absorption to the original oven-dry mass of the specimen.

$$\text{Water Absorption (\%)} = \frac{M_2 - M_1}{M_1}\ x\ 100\% \qquad (16)$$

3.9.2 Water Permeability Test

The water permeability test was conducted on 150 mm × 150 mm × 150 mm ECC cube specimens using the falling head permeability method, in accordance with the guidelines of ASTM D5084-16a. The samples were casted and water cured for 28 days. Prior to testing, the lateral surfaces were coated with epoxy resin to ensure unidirectional water flow through the specimen during the test. To achieve complete saturation, specimens were placed under a vacuum of 1 mmHg for 3 hours, followed by the introduction of de-aerated water while maintaining the vacuum for an additional 1 hour. The specimens were then soaked in water for a period of 18 to 24 hours to ensure full saturation of the pore structure. The test setup, illustrated in Figure 48, consisted of a permeameter cell equipped with rubber gaskets, a graduated standpipe, and watertight connectors to ensure leak-free operation.

Figure 48: Water Permeability Test Set-up

After sealing the saturated specimen within the permeameter, the system was filled using de-aerated water and permitting to stabilize for 30 minutes before initiating the test. Water was then allowed to flow through the specimen for a total duration of 100 hours under the influence of hydraulic pressure. The test commenced by recording the initial water head and the corresponding start time. As water permeated through the specimen, the time at which the water head dropped to a predefined lower level was recorded. The coefficient of permeability (k) was computed using the standard falling head Equation 17, taking into account the head difference, cross-sectional area, flow path length, and elapsed time.

$$\text{Coefficient of Permeability (k)} = \frac{\mathrm{aL}}{\mathrm{At}} \ln\left(\frac{h_1}{h_2}\right) \tag{17}$$

where k is the coefficient of permeability (cm/s), a is the standpipe's cross-sectional area (cm^2), L is the specimen's length (cm), and A is the specimen's cross-sectional area (cm^2). t is time taken for the water level to fall from $h_1$to h_2 (s), h_1 is initial water head (cm), h_2 is final water head (cm) and ln is natural logarithm.

3.9.3 Sulphate and Chloride Resistance

To assess the durability of ECC under aggressive environmental conditions, sulphate and chloride exposure tests were conducted following modified procedures in line with ASTM C1012 and ASTM C672. Freshly prepared ECC cubes of dimensions 70.6 mm × 70.6 mm × 70.6 mm were casted and subjected to standard water curing for 28 days. To simulate sulphate and chloride attack, aggressive solutions were prepared as recommended by previous studies: 5% sodium sulphate (Na_2SO_4) solution by mass, and 5% sodium chloride (NaCl) solution by mass. The 28-day water-cured specimens were then immersed in these solutions for 28, 90, and 180 days, as illustrated from Figure 49 to Figure 52.

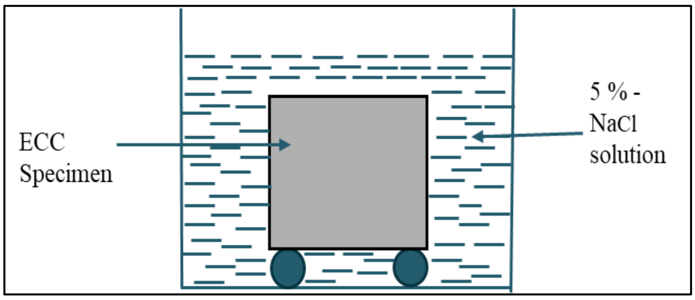

Figure 49: Line Diagram of the Chloride Attack Set-up

Figure 50: ECC specimen in the solution of 5% NaCl

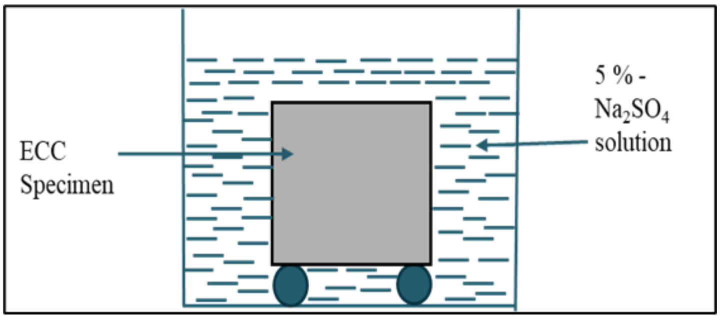

Figure 51: Line Diagram of the Sulphate Attack Set-up

Figure 52: ECC Specimen in the solution of 5% Na_2SO_4

Concurrently, a set of control specimens was maintained under identical curing conditions but immersed in plain water. For each exposure condition and curing duration, a set of three specimens per mix was tested. Following exposure, the specimens were air-dried for 24 hours and subsequently tested for their compressive strength. Visual inspection was also conducted to observe any signs of surface deterioration such as cracking, spalling, or discoloration (Figure 53 and Figure 54). The extent of degradation was quantified based on the dry density, percentage reduction in compressive strength, and weight when compared to control specimens.

Figure 53: ECC Cube before Chloride Attack

Figure 54: ECC Cube after Chloride Attack

3.9.4 Rapid Chloride Permeability Test

In compliance with ASTM C1202-22, the Rapid Chloride Penetration Test (RCPT) was performed to assess the chloride ion permeability of ECC. From hardened ECC samples, cylindrical pieces of 100 mm in diameter and 50 mm in thickness were removed. The lateral surface of each specimen was sealed with epoxy coating to ensure unidirectional ion migration during the test. The specimens were put in a vacuum chamber for three hours after the epoxy had dried. They were then vacuum-saturated with de-aerated water for an hour followed by soaking in the same water for 18 hours to ensure complete saturation, as illustrated in Figure 55.

Figure 55: Sample specimen in the vacuume

The prepared specimens were then positioned in the RCPT test apparatus, as shown in Figure 56.

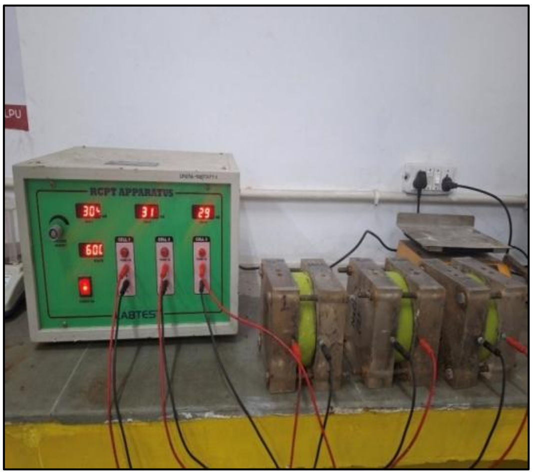

Figure 56: RCPT test set up apparatus

A 3% sodium chloride (NaCl) solution was placed in the test cell's negative terminal (-), and a 0.3N sodium hydroxide (NaOH) solution was placed in the positive terminal (+).

For six hours straight, a 60-volt DC voltage was placed across the specimen, during which current readings were recorded every 30 minutes. Upon completion of the test duration, the total charge passed through the specimen, measured in coulombs, was calculated using Equation 18.

$$\mathrm{I}_{average}\,(\text{coulomb}) = \mathrm{I}_{cummulative}\; x\; 900$$

$$\mathrm{I}_{cummulative} = \mathrm{I}_{0} + 2\,x\,\mathrm{I}_{30} + 2\,x\,\mathrm{I}_{60} + 2\,x\,\mathrm{I}_{90} + 2\,x\,\mathrm{I}_{120} + 2\,x\,\mathrm{I}_{150} + 2\,x\,\mathrm{I}_{180} + 2\,x\,\mathrm{I}_{210} + 2\,x\,\mathrm{I}_{240} + 2\,x\,\mathrm{I}_{270} + 2\,x\,\mathrm{I}_{300} + 2\,x\,\mathrm{I}_{320} + \mathrm{I}_{360} \quad (18)$$

Where, I_0 represent the initial current reading (mA) I_{30} represent the current reading at 30-minute (mA) I_{60} represent the current reading at 60 minute (mA) and so on.

This charge value serves as an indicator of the specimen's chloride permeability (Table 17).

Table 14: Chloride Permeability Classification Based on RCPT Results

Total Charge Passed (Coulombs)	Chloride Ion Permeability
> 4000	High Permeability
2000 – 4000	Moderate Permeability
1000 – 2000	Low Permeability
100 – 1000	Very Low Permeability
< 100	Negligible Permeability

According to ASTM C1202, the total charge passed through the specimen during the 6-hour test is used to classify the chloride ion permeability of concrete. Lower coulomb values indicate better resistance to chloride penetration, which is critical for durability in aggressive environments. A schematic of the RCPT setup is provided in Figure 57.

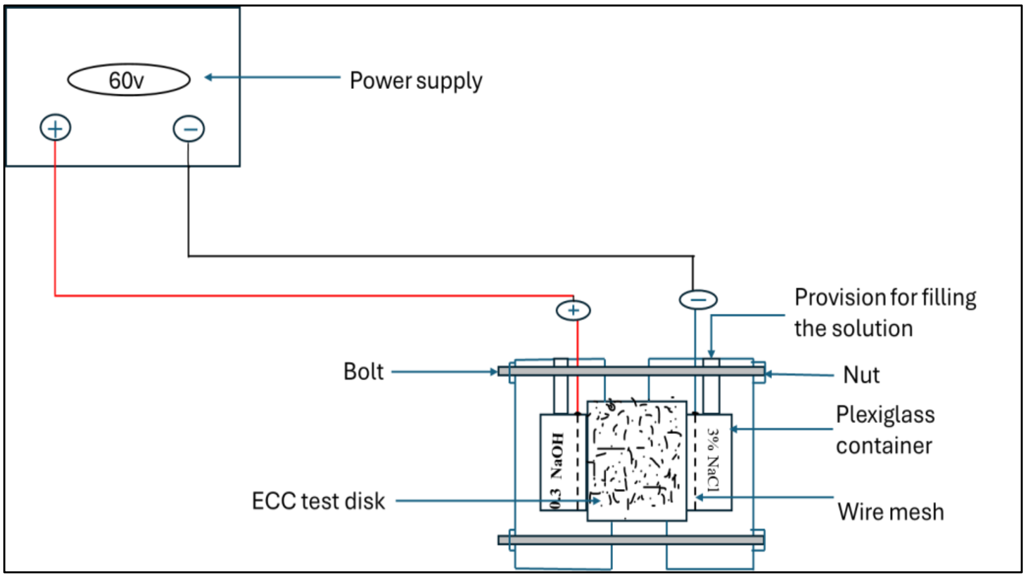

Figure 57: Schematic Diagram of RCPT Test Setup

3.10 Development of FEM Model

3.10.1 Geometry Design

The finite element model for the compressive strength analysis of ECC consists of three primary components: the ECC cube specimen, a loading plate, and a support plate. The cube specimen, depicted in Figure 58, is modelled as a 3D deformable body with dimensions of 70.6 mm × 70.6 mm × 70.6 mm to simulate the material's stress-strain behaviour under compression accurately. These dimensions adhere to standard testing protocols, ensuring the validity of the simulation when compared with experimental results. The loading and support plates, shown in Figure 59, are modelled as 3D discrete rigid bodies with a diameter of 150 mm and a depth of 25 mm. The rigid nature of these plates ensures that no deformation occurs during the simulation, allowing the applied load to be distributed uniformly across the contact surface. The dimensions of the plates are chosen to accommodate the cube specimen fully and to replicate experimental conditions accurately. The reference point (RP) located at the centre of the loading plate facilitates controlled load application. This setup mimics real-world testing conditions, ensuring that the simulation accurately captures the compressive response of the ECC material. The rigid support plate provides a stable base for the specimen, eliminating any potential boundary condition discrepancies.

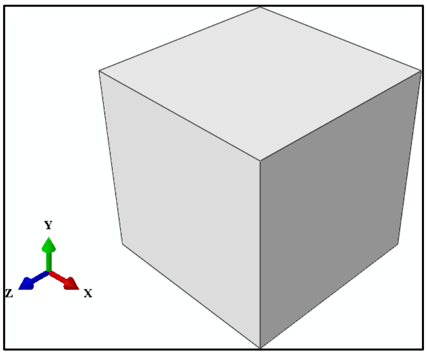

Figure 58:FEM Model of a 3D Deformable Cube Specimen for Compressive Strength Test.

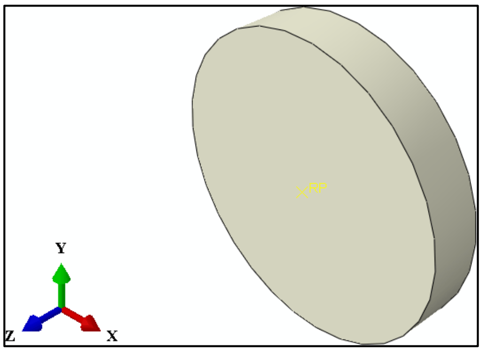

Figure 59: 3D Discrete Rigid Loading and Support Plate.

The geometry for the direct tensile test assembly includes a 3D deformable coupon specimen and 3D discrete rigid catchers. The dimensions of the coupon specimen are 300 mm × 50 mm × 15 mm, designed to simulate tensile stress distribution. The coupon is modelled as a 3D deformable solid, capable of capturing stress-strain behaviour under direct tensile loading. The catchers are modelled as 3D discrete rigid bodies, with vertical and horizontal dimensions of 150 mm and 100 mm, respectively, as shown in Figure 60 and Figure 61. The catcher assembly ensures accurate load application and uniform distribution across the beam's ends. The reference point (RP) at the top midpoint of the catcher facilitates the application of controlled tensile loads. This setup ensures precise alignment and load transfer during the tensile test simulation.

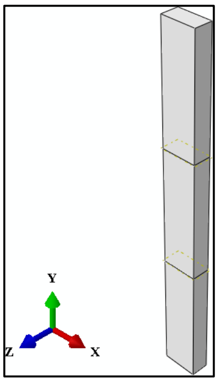

Figure 60: FEM Model of a 3D Deformable Beam Specimen for Tensile Strength Test.

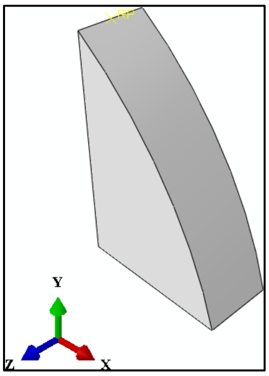

Figure 61: 3D Discrete Rigid Catcher in Tensile Strength Test Modelling.

The geometric and modelling details for both components are given in Table 18, which outlines the specifications of the beam sample and the catchers. The combination of deformable and rigid components ensures reliable simulation of tensile strength behaviour, accurately replicating experimental setups.

Table 15: Dimensions and Modelling Details of FEM Components for Compressive and tensile Strength Analysis.

Testing	Component	Parameter	Dimension (mm)	Model
Compressive Strength	Concrete Cube	Length	70.6	3D Deformable
		Thickness	70.6	
		Width	70.6	
	Loading Plate	Diameter	150	3D Discrete Rigid
		Depth	25	
	Support Plate	Diameter	150	3D Discrete Rigid
		Depth	25	
Tensile Strength	Beam	Length	300	3D Deformable
		Thickness	15	
		Width	15	
	Holding Catchers	Height	150	3D Discrete Rigid
		Width	100	

3.10.2 Material properties & Element Selection for data input

ECC is characterized by high ductility and superior crack resistance. The material properties, as presented in Table 19, include a mass density of 2143 kg/m³, Young's modulus of 25.1 GPa, and Poisson's ratio of 0.15, where the Young's modulus and Poisson's ratio of ECC was found using LVDT and extensometer respectively in compression testing machine in the accordance with ASTM C469. These properties are critical for accurately modelling the mechanical behaviour of ECC under compressive and tensile loading. To represent the ECC specimen, a solid and homogeneous section is selected, ensuring uniform material property distribution throughout the model. The experimental data for yield stress and strain values are incorporated into the FEM model to account for the non-linear behaviour of ECC during tensile stress analysis. The coupon is modelled as a solid homogeneous section, ensuring uniform material property distribution across the specimen.

ECC demonstrates different mechanical behaviours under compressive and tensile stresses, resulting in different values for Young's modulus. For compressive strength, the ECC is categorized by a Young's modulus of 25,100 MPa, while for tensile strength, a lower Young's modulus of 2,000 MPa is adopted. This distinction reflects the material's strain-hardening behaviour and reduced stiffness under tensile loading. This setup facilitates precise simulations of stress-strain responses, contributing to a realistic and reliable finite element analysis.

Table 16: Material Properties of Engineered Cementitious Composites (ECC) for Both Tensile and Compressive Strength Analyses

Name of Part	Property Description	Unit	Value
Cube	Density	Ton/mm^3	$2.143 * 10^{-9}$
	Young's Modulus	MPa	25100
	Poisson's Ratio	-	0.15
Coupon	Density	Ton/mm^3	$2.143 * 10^{-9}$
	Young's Modulus	MPa	2000
	Poisson's Ratio	-	0.15

3.10.3 Assembly, Step, and Interaction

As shown in Figure 62, the ECC cube specimen is positioned between the loading and support plates to form the assembly. The loading and support plates are represented as 3D discrete rigid bodies, but the cube is represented as a 3D deformable solid. The plates are positioned symmetrically with respect to the cube to ensure uniform load transfer during the compressive strength analysis. For the simulation, a static general step is selected to capture the compressive behaviour of the ECC under gradual load application. The interaction between the rigid plates and the deformable cube is defined using a tie interaction, ensuring perfect bonding and preventing relative motion at the contact surfaces. This setup accurately replicates the experimental boundary conditions and provides a stable and efficient computational model for analysing the compressive response of ECC.

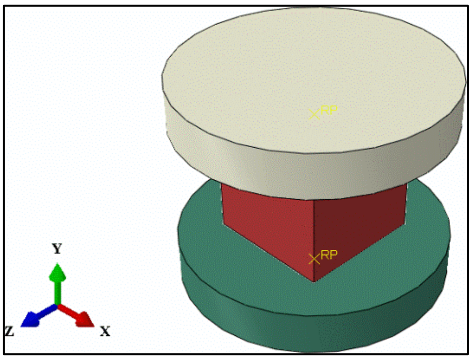

Figure 62 Assembly of ECC Cube Specimen with Loading and Support Plates.

The assembly for the tensile strength analysis consists of the ECC coupon specimen placed between two catchers, as shown in Figure 63. The catchers are positioned at the top and bottom of the coupon to ensure symmetrical load transfer. The coupon is modelled as a 3D deformable solid, while the catchers are represented as 3D discrete rigid bodies for accurate load application. A dynamic explicit step is selected for the tensile strength simulation to account for the non-linear behaviour of the ECC material under dynamic tensile loading conditions. This approach enables precise modelling of the strain-hardening and crack propagation phenomena inherent in ECC. The interaction behaviour between the ECC beam and the catchers is defined using a tie interaction, ensuring no relative motion or slippage occurs at the contact surfaces during tensile loading. This interaction setup guarantees uniform stress distribution across the beam and eliminates the possibility of inaccuracies due to slip or misalignment. This robust assembly and interaction modelling allow for reliable simulation of the tensile strength behaviour of ECC.

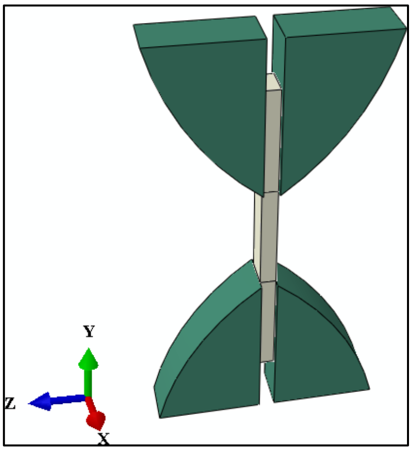

Figure 63 Assembly of ECC beam Specimen with catchers

3.10.4 Loading and Boundary Conditions

In the finite element analysis, a uniform pressure load of 46 N/mm² was applied to the top surface of the rigid loading plate to represent an idealized and evenly distributed compressive load. This loading approach ensures numerical stability and avoids localized stress concentrations that may arise from point or nodal loading, as shown in Figure 64. The applied pressure level was selected to be representative of the experimentally observed 28-day compressive strength of the ECC cube specimen (43.58 MPa), enabling meaningful comparison between experimental and numerical results. The use of uniform pressure further ensures an even distribution of compressive force across the ECC cube, thereby realistically simulating platen-induced loading conditions in the physical compression test. The load is transmitted to the cube via the tie interaction between the rigid plate and the specimen. The bottom support plate is fixed with a boundary condition of Ux = Uy = Uz = UR1 = UR2 = UR3 = 0**,** where all translational and rotational degrees of freedom are restrained. This rigid fixed boundary condition ensures the stability of the support plate during the simulation and prevents any displacement or rotation, allowing the cube to experience pure compressive loading.

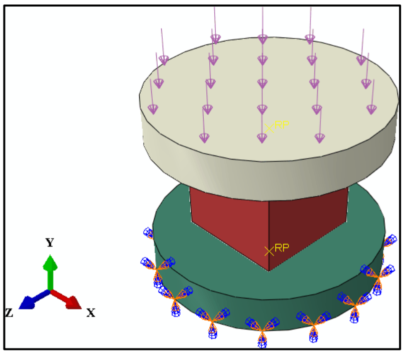

Figure 64: Loading and Boundary Conditions for ECC Cube Specimen under compression loading.

For the tensile strength analysis, constant displacement forces are applied to the catchers in the positive and negative Y-directions to create tensile loading on the ECC coupon specimen. A displacement of 6.4 mm is prescribed at the top catcher in the positive Y-direction, while an equal and opposite displacement of -6.4 mm is applied to the bottom catcher in the negative Y-direction, as illustrated in Figure 65. This displacement-controlled loading ensures uniform tensile forces are generated along the coupon 's length, enabling accurate simulation of the material's response under tensile stress. The catchers, modelled as rigid bodies, ensure no deformation occurs at the boundaries, facilitating precise load application. The tie interaction between the coupon and the catchers ensures no slip occurs, maintaining consistent stress transfer throughout the tensile loading process.

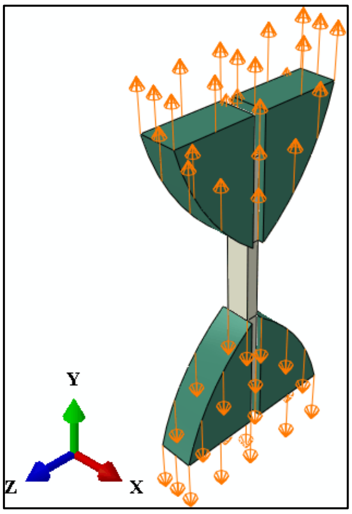

Figure 65: Loading and Boundary Conditions for ECC Beam Specimen Under Tensile Loading

3.10.5 Modelling in FEM

The finite element mesh was generated for all components in the assembly to ensure accurate analysis of the compressive strength of the ECC cube as shown in Figure 66. The meshing parameters and details are summarized in Table 20. The cube was meshed using linear hexahedral elements (C3D8R) with an element size of 7.1 mm, resulting in a total of 1331 nodes and 1000 elements. This element type and size were chosen to accurately capture the deformation and stress distribution in the cube under compressive loading while maintaining computational efficiency.

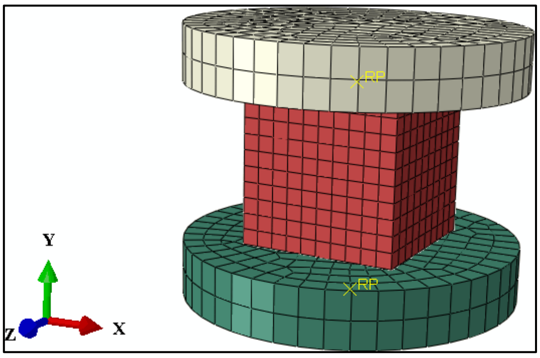

Figure 66: Meshed Assembly of ECC Cube with Loading and Support Plates.

The loading and support plates were meshed using linear triangular elements (R3D4) with an element size of 10.5 mm. Each plate consisted of 521 nodes and 527 elements, providing sufficient resolution for rigid body interactions without unnecessary computational overhead. The meshing of the plates was uniform to facilitate smooth load transfer to the cube via the tie interaction defined between the plates and the cube. The meshing, as shown in Table 20, ensures compatibility between the deformable and rigid components in the assembly, with sufficient refinement at the contact interfaces. The finite element model for the tensile strength analysis was meshed to ensure computational efficiency while maintaining accuracy in stress and strain predictions. The meshed assembly of the ECC coupon and catchers is shown in Figure 67, while the detailed meshing parameters are summarized in Table 20. The ECC beam was meshed using linear hexahedral elements (C3D8R), with an element size of 5 mm. This fine meshing resulted in 1708 nodes and 1080 elements, allowing precise capture of the strain-hardening and failure behaviour of ECC under tensile loading. The holding catchers, modelled as discrete rigid bodies, were meshed using linear triangular elements (R3D4) with an element size of 18 mm. Each catcher consisted of 148 nodes and 147 elements. The coarser mesh for the catchers ensures computational efficiency, as these components are rigid and do not deform under loading. This meshing strategy ensures compatibility between the deformable ECC beam and the rigid catchers, enabling accurate stress transfer and realistic simulation results. The uniform meshing across the beam facilitates detailed analysis of the stress and strain distribution under tensile loading.

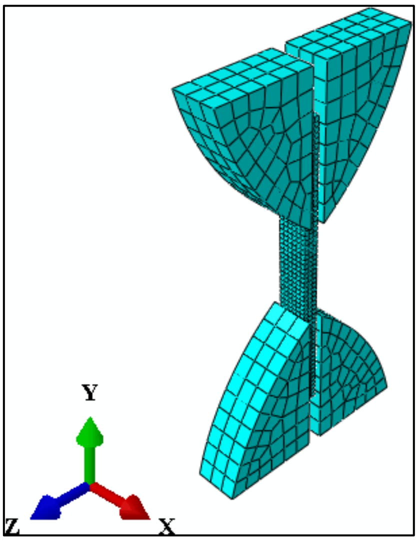

Figure 67: Meshed Assembly of ECC beam with catchers

Table 17: Meshing Details of FEM Components for Compressive and tensile Strength Analysis.

Analysis	**Part**	**Description**	**Details**
Compressive Strength	Cube	Element Size	7.1
		No. of nodes	1331
		No. of elements	1000
		Type of Element	linear hexahedral (C3D8R)
	Loading Plate	Element Size	10.5
		No. of nodes	521
		No. of elements	527
		Type of Element	linear triangular (R3D4)
	Support Plate	Element Size	10.5

		No. of nodes	521
		No. of elements	527
		Type of Element	linear triangular (R3D4)
Tensile Strength	ECC Beam	Element Size	5
		No. of nodes	1708
		No. of elements	1080
		Type of Element	linear hexahedral (C3D8R)
	Holding Catchers Each	Element Size	18
		No. of nodes	148
		No. of elements	147
		Type of Element	linear triangular (R3D4)

3.11 Summary of the Chapter

This chapter presents a comprehensive overview of the materials and methodologies employed in the experimental investigation of ECC. The chapter begins by detailing the key materials used such as cement, river sand, manufactured sand, fly ash, sugarcane bagasse ash (SCBA), polyvinyl alcohol (PVA) fiber, superplasticizer, and water—highlighting their roles and physical properties. The research framework and various trial and control mix designs are explained, followed by procedures for mixing, casting, and curing. The testing methodology included evaluation of both fresh and mechanical properties, such as workability, compressive strength, direct tensile strength, and flexural performance. Durability assessments cover water absorption, water permeability, sulfate and chloride resistance, and the Rapid Chloride Penetration Test (RCPT), conducted in accordance with relevant ASTM standards. The chapter concludes with the development of a Finite Element Method (FEM) model using ABAQUS, describing the geometry creation, material properties, element selection, boundary conditions, and simulation setup for analyzing ECC behavior under different loading scenarios.

CHAPTER 4

RESULTS & DISCUSSION

4.1 General

This chapter provides a thorough analysis and explanation of the findings from the several experimental and numerical tests conducted for this ECC research. The analysis begins with the evaluation of fresh properties of ECC, which includes the impact of RS replacement with M-Sand at 0%, 20%, 40%, 60%, 80% and 100% on flowability characteristics essential for its placement and compaction. Subsequently, the mechanical performance of ECC is examined through standard strength evaluation methods, namely the compressive strength test, direct tensile strength test, and flexural strength test. These tests offer insights into the fundamental load-bearing capabilities and ductility of the developed ECC mixes. Furthermore, the durability performance of ECC is assessed through multiple tests such as water absorption, water permeability, resistance to sulphate and chloride attack, and rapid chloride penetration. These evaluations are crucial in comprehending the long-term performance and serviceability of ECC in aggressive environments.

In addition, this chapter encompasses the development and execution of a Finite Element Method (FEM) model designed to replicate the mechanical behaviour of ECC. The simulation specifically targeted the compressive and direct tensile strengths, aiming to mirror the experimental performance observed at 28 days. A comparative analysis was conducted between the simulated outcomes and the corresponding experimental results. The FEM model demonstrated a strong correlation with the actual test data, confirming the accuracy and reliability of the numerical approach used in evaluating ECC's mechanical properties.

4.2 Fresh Properties of ECC

4.2.1 Flowability of ECC

Flowability variations of all the mixes are shown in Figure 68. Both ECC-FA (Group I) mixes and ECC-SCBA (Group II) mixes showed a decline in flowability as M-sand content increases. This trend is primarily attributed to the angular shape, rough texture, and higher water demand of M-sand particles compared to the smoother, rounded particles of river sand (RS), which increases inter-particle friction and reduces flow spread.

Another trend is witnessed where ECC-FA mixes consistently exhibited higher flowability of around 6% than ECC-SCBA across all replacement levels, with the average diameter spread for ECC-FA ranging from 278 mm at 0% M-sand to 218 mm at 100% M-sand, while ECC-SCBA ranged from 256 mm to 212 mm under the same replacements. The better flowability of ECC-FA can be attributed to the spherical shape, smaller particle size, and smoother surface texture of FA compared to the larger and irregular SCBA particles, which tend to increase inter-particle friction and reduce lubrication.

Although some variation is observed in individual flow test results, the consistently lower flowability of ECC-SCBA mixes across all M-sand replacement levels indicates a material-dependent trend rather than random experimental scatter. The reduction in flowability associated with SCBA is governed by its irregular morphology, rough surface texture, and internal porosity, as observed from SEM analysis, which increases water absorption and internal friction within the matrix.

The gap in flowability between ECC-FA and ECC-SCBA narrows from 7.9% to 2.7% as M-sand content increases. At higher M-sand replacement levels, the angularity and surface texture of M-sand dominate the fresh-state behaviour of the mix, thereby reducing the relative influence of the binder type (FA or SCBA) on flowability. Despite the reduction in flowability with increasing M-sand content, all mixes maintained adequate workability suitable for ECC applications.

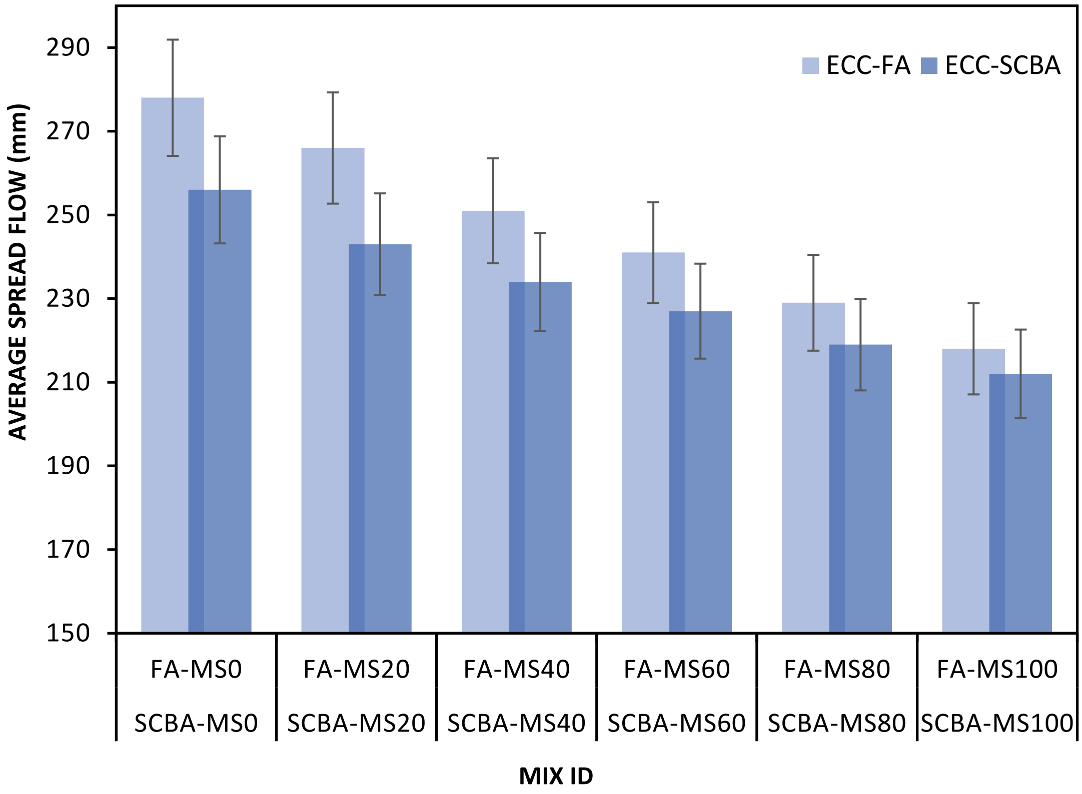

Figure 68: Average Spread Flow of Fresh ECC for all Mixes

4.3 Mechanical Properties

4.3.1 Compressive strength

The compressive strength results of ECC-FA (Group I) mixes with varying M-sand content demonstrated in Figure 67 depicts a clear trend of strength development over time, with all mixes showing significant improvement from 7 to 90 days. At 28 days, the mix with 60% M-sand replacement (FA-MS60) achieved the most strength i.e. 43.98 MPa, showing an approximate 22% increase in comparison with the control mix FA-MS0 i.e. 36.47 MPa. The strength increased progressively from FA-MS0 to FA-MS60, indicating that partial replacement of river sand with M-sand enhances the performance of fly ash-based concrete. The increase is largely due to improved particle packing, stronger paste-aggregate bonding, and reduced voids, all of which contribute to a more cohesive and durable concrete mix. However, a slight decline in strength was noted beyond 60% replacement: FA-MS80 at 42.63 MPa and FA-MS100 at 41.89 MPa showed a 2.5% and 4% decrease, respectively, compared to FA-MS60. Despite this minor reduction, their strength remained higher than that of the control mix. These results confirm that using M-sand up to 60% optimizes the compressive strength at 7 days, 28 days and 90 days, while higher levels may reduce effectiveness due to the increased angularity and reduced particle packing associated with excess M-sand.

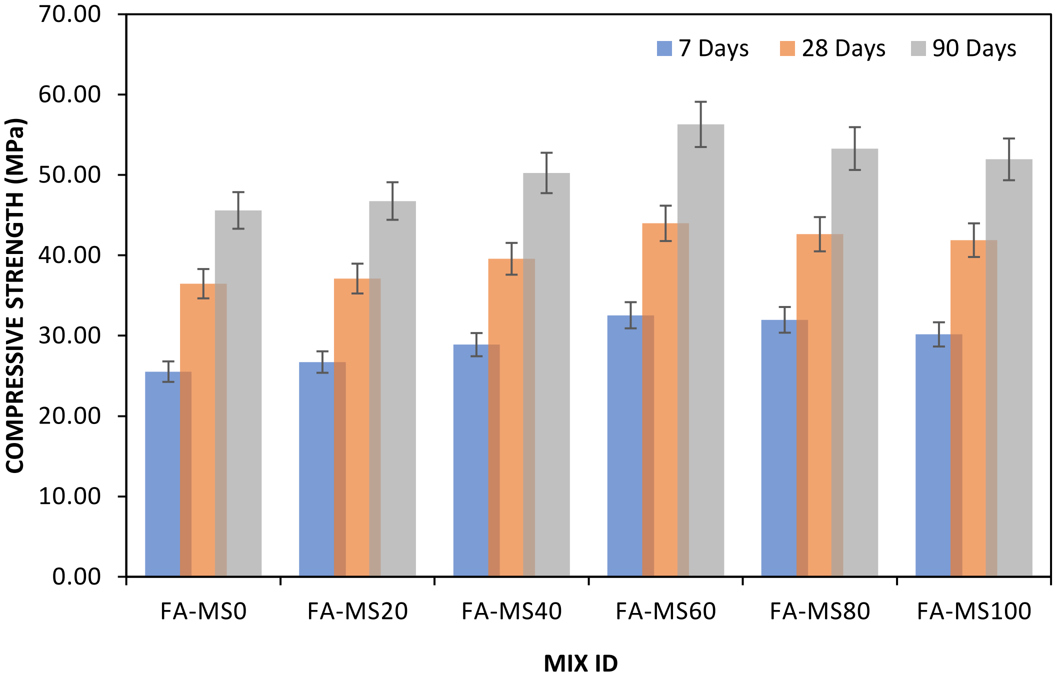

Figure 69: Compressive Strength of ECC-FA (Group I) at 7, 28 and 90 Days

The compressive strength of ECC-SCBA (Group II) with varying M-sand content showed a consistent increase from 7 to 90 days for all mix types (Figure 70). Among these, the SCBA-MS60 mix achieved the highest compressive strength across all curing periods. At 28 days, SCBA-MS60 recorded a strength of 35.89 MPa approximately 25% higher than the control mix (SCBA-MS0). This improvement can be attributed to the enhanced interlocking and paste bonding facilitated by the angular texture of M-sand up to this replacement level. The strength increased steadily from SCBA-MS0 to SCBA-MS60, confirming that partial substitute of river sand with M-sand improves strength in SCBA-based systems as well. However, beyond 60% replacement, the strength began to decline slightly, with SCBA-MS80 at 33.12 MPa and SCBA-MS100 at 32.49 MPa showing a 3.5% and 6% decrease, respectively, compared to SCBA-MS60 at 28 days. Despite this reduction, both mixes still outperformed the control.

These findings suggest that a 60% M-sand replacement is optimal for maximizing compressive strength in SCBA-based concrete, while higher levels may compromise performance due to excessive angularity, leading to reduced workability and packing efficiency.

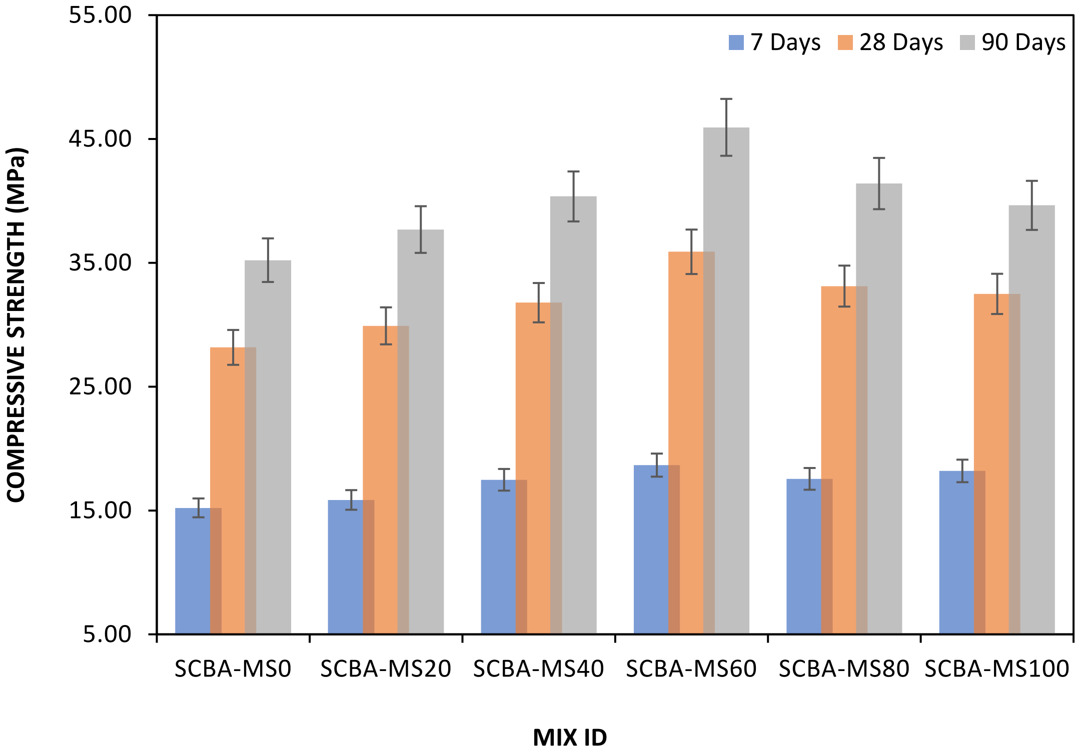

Figure 70: Compressive Strength of ECC-SCBA (Group II) at 7, 28 and 90 Days

At 28 days, both FA and SCBA mixes achieved peak strength at 60% M-sand replacement. While SCBA mixes showed a slightly higher percentage gain from their control 25% against 22%, the overall compressive strength was consistently higher in FA mixes across all M-sand levels. The observed increase in compressive strength at replacement levels up to and around 60% for both FA- and SCBA-based ECC mixes can be attributed to improved particle packing and enhanced paste–aggregate interlocking achieved through partial replacement of river sand with angular M-sand. At this replacement level, the angularity and surface roughness of M-sand promote better mechanical interlocking with the cementitious matrix, while the presence of fine particles assists in filling micro-voids, leading to a denser and more homogeneous microstructure. Additionally, the denser packing improves stress transfer across the matrix–aggregate interface, contributing to higher compressive strength. Beyond this level, further increase in M-sand content introduces excessive angularity, which marginally reduces workability and packing efficiency, resulting in a slight reduction in strength.

4.3.2 Direct-Tensile Strength

The direct tensile strength of all ECC-FA (Group I) mixes improved over time with higher M-sand content, with peak values consistently observed at 90 days (Figure 71). Strength increased with M-sand replacement up to 60%, where FA-MS60 recorded the highest tensile strength of 3.37 MPa at 7 days, 4.89 MPa at 28 days, and 5.56 MPa at 90 days across all curing periods. At 28 days, FA-MS60 achieved a 16% increase compared to the control mix (FA-MS0). This enhancement is attributed to better aggregate interlocking and bond strength due to M-sand's angular texture resulting in to improved matrix-fiber interaction.

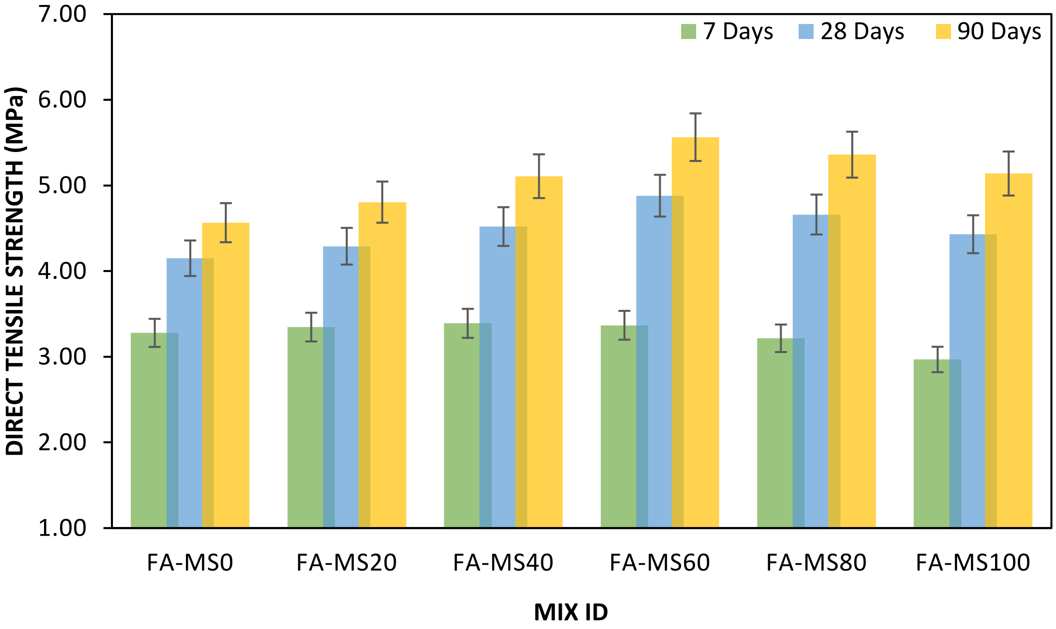

Figure 71: Direct-Tensile Strength of ECC-FA (Group I) at 7, 28 and 90 Days

However, beyond 60% replacement, a gradual decline in tensile strength was observed, FA-MS80 at 4.66 MPa and FA-MS100 at 4.43 MPa showed a 4% and 7% reduction, respectively, compared to FA-MS60. This drop may be attributed to the loss in fiber-matrix bond due to higher content of M-sand leading to poor workability. Fibers are most beneficial when adequate lubrication and dispersion are maintained in the mix typically achievable at up to 60% M-sand. Beyond that, their positive effect is offset by workability.

The direct tensile strength of all ECC-SCBA (Group II) mixes increased steadily with M-sand replacement up to 60%, followed by a reduction at higher replacement levels (Figure 72). An increase in strength from around 3.1 MPa at 0% M-sand to 4.0 MPa at 60% M-Sand was recorded at 28 days, which is a 29% increase. The reason for this improvement is the angularity and rough texture of M-sand enhancing the aggregate–matrix interlock and improving fiber anchorage, thus boosting the overall crack-bridging capacity of the matrix. Additionally, the denser packing at optimal M-sand levels contributed to a more homogeneous matrix that facilitated efficient fiber stress transfer.

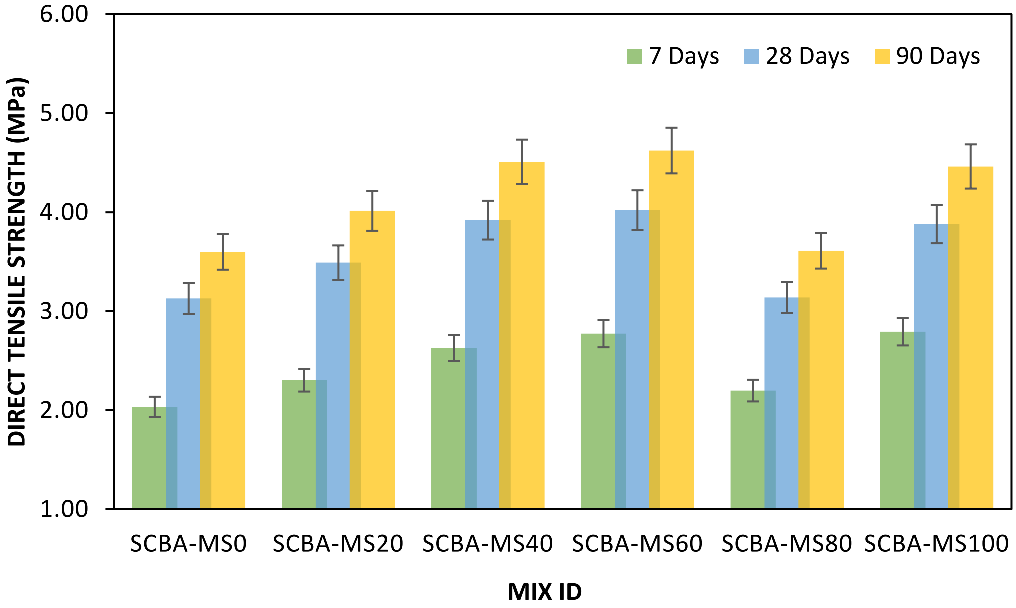

Figure 72: Direct-Tensile Strength of ECC-SCBA (Group II) at 7, 28 and 90 Days

However, beyond 60% M-sand replacement, tensile strength declined. At 100% M-sand, the tensile strength dropped to 3.9 MPa, marking a 2.5% decrease from its respective peak. This decline is primarily due to a reduction in workability caused by M-sand's high angularity and lack of fines, which hindered uniform fiber dispersion.

Poor fiber orientation and clustering reduced their crack-bridging efficiency. Moreover, the increased internal friction and reduced cohesiveness at higher M-sand contents led to localized weaknesses and stress concentrations, negatively impacting tensile strength performance.

The direct tension test results highlight a clear difference in the influence of FA and SCBA on tensile ductility. ECC-FA mixes consistently exhibited higher tensile ductility than ECC-SCBA mixes at all M-sand replacement levels and curing ages. This behaviour is attributed to the finer particle size and spherical morphology of FA, which results in a denser and more homogeneous matrix, enhancing fiber dispersion and fiber–matrix bonding, and thereby promoting stable multiple micro-cracking under tensile loading. In contrast, the coarser and more irregular SCBA particles increase matrix heterogeneity, which limits fiber bridging efficiency and reduces crack control, leading to comparatively lower tensile ductility. Although both systems achieved maximum ductility at 60% M-sand replacement, the superior ductility performance of ECC-FA confirms the more favourable role of FA in enhancing tensile strain capacity compared to SCBA.

4.3.3 Flexural Strength

The flexural strength of ECC-FA (Group I) mixes demonstrated a clear increasing trend with M-sand replacement up to 60%, followed by a marginal reduction at higher replacement levels (Figure 73). At 28 days, the strength improved from approximately 4.6 MPa for FA-MS0 to around 6.1 MPa for FA-MS60, showing a significant increase of about 32.6%. This enhancement can be attributed to the angular and rough-textured nature of M-sand, which promotes better mechanical interlocking between aggregate particles and improves the bond at the matrix–aggregate interface. This denser interlocking, combined with enhanced fiber anchorage, facilitates more efficient crack bridging under flexural loads.

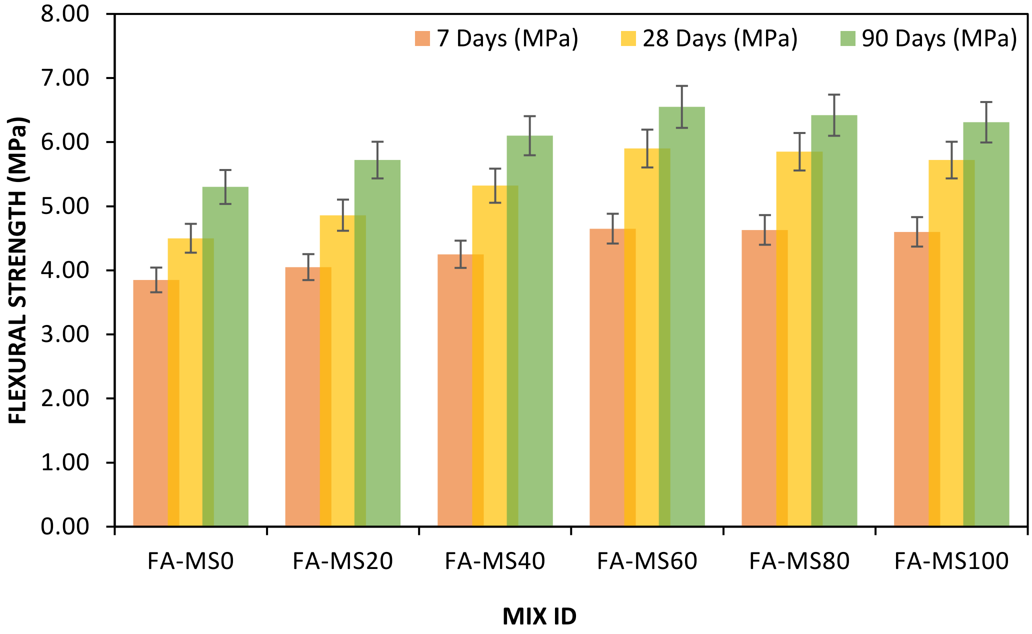

Figure 73: Flexural Strength of ECC-FA (Group I) at 7, 28 and 90 Days

However, beyond the 60% replacement level, a slight reduction in flexural strength was observed. At 100% M-sand (FA-MS100), the strength dropped to around 5.8 MPa, indicating a 5% decrease compared to the FA-MS60 peak. This reduction is likely due to compromised workability and poor fiber dispersion at higher M-sand content, which could lead to uneven distribution and orientation of fibers. Such clustering diminishes the crack-bridging efficiency of fibers, leading to early crack initiation and propagation under bending stresses.

The flexural strength development of ECC-SCBA (Group II) mixes with increasing M-sand replacement shows a consistent increase across all curing ages 7, 28, and 90 days reaching peak values at 80–100% M-sand content (Figure 74). At 7 days, the flexural strength rose from 3.7 MPa in the control mix (SCBA-MS0) to 4.5 MPa in SCBA-MS80, marking an improvement of approximately 21.6%. At 28 days, the strength increased from 4.4 MPa to 5.3 MPa (20.5% increase), and at 90 days, it rose from 5.0 MPa to 5.9 MPa (18% increase).

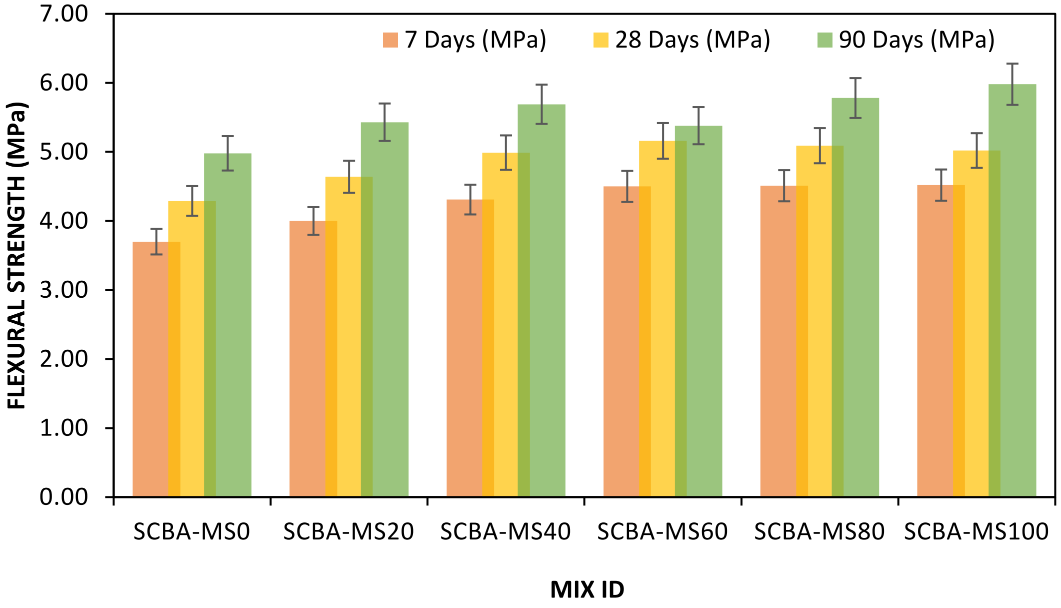

Figure 74: Flexural Strength of ECC-SCBA (Group II) at 7, 28 and 90 Days

This progressive enhancement in strength can be attributed to the combined effects of SCBA's pozzolanic activity and the angular, coarse texture of M-sand, which together lead to improved particle packing, matrix densification, and better fiber matrix bonding under flexural loads. Additionally, the sustained or even improved performance at higher M-sand replacements in SCBA mixes unlike in FA-based mixes where a drop was observed beyond 60% suggests better compatibility of SCBA with M-sand, likely due to its finer reactive silica content enhancing the interfacial transition zone over time.

4.4 Durability Properties

4.4.1 Water Absorption and Dry Density

Figure 75 depicts the water absorption of ECC-FA (Group I) mixes and shows water absorption rate reduces with increment in curing age owing to the densification of the matrix with age. Also, an increasing trend with the increase in M-sand content across all ages is witnessed. At 28 days, absorption rises from 6.79% (FA-MS0) to about 7.52% (FA-MS100). This consistent increase indicates that higher replacement of river sand with M-sand, which is more angular and less rounded, contributes to higher void content and surface area, allowing more water ingress. Over time, water absorption slightly decreases, reflecting ongoing hydration and refinement of the microstructure, but the effect of increasing M-sand still dominates, leading to overall higher absorption values at higher replacement levels.

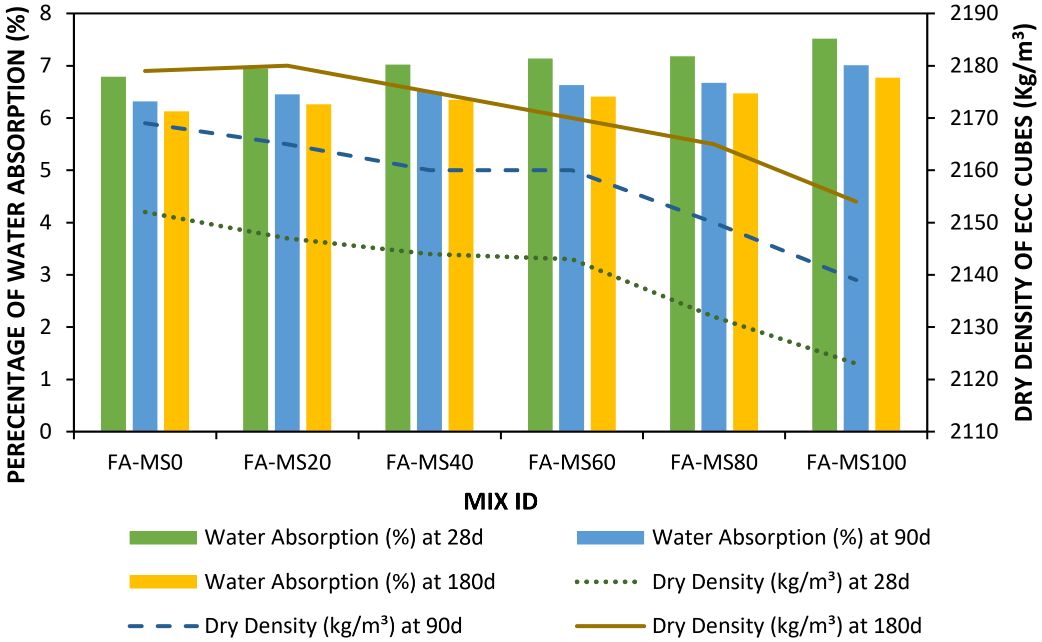

Figure 75: Water Absorption and Dry Density of ECC-FA (Group I) at 28, 90 and 180 Days

In contrast, dry density shows a clear decreasing pattern with increasing M-sand. The density drops gradually from around 2180 kg/m³ at FA-MS0 to approximately 2150 kg/m³ at FA-MS100 (180 days) (Figure 75). This reduction is due to the increased porosity introduced by the angular and coarser nature of M-sand and possible less effective particle packing compared to finer river sand.

The (Figure 76) illustrates the relationship between water absorption and dry density for ECC-SCBA (Group II) mixes at various curing ages (28, 90, and 180 days). Water absorption shows an increasing trend with higher M-sand replacement levels. At 28 days, absorption rises from approximately 7.81% in SCBA-MS0 to over 8.35% in SCBA-MS100, indicating greater porosity. This is primarily owing to the porous and irregular nature of SCBA particles, combined with the angular texture of M-sand, which reduces the packing efficiency and increases capillary voids within the matrix.

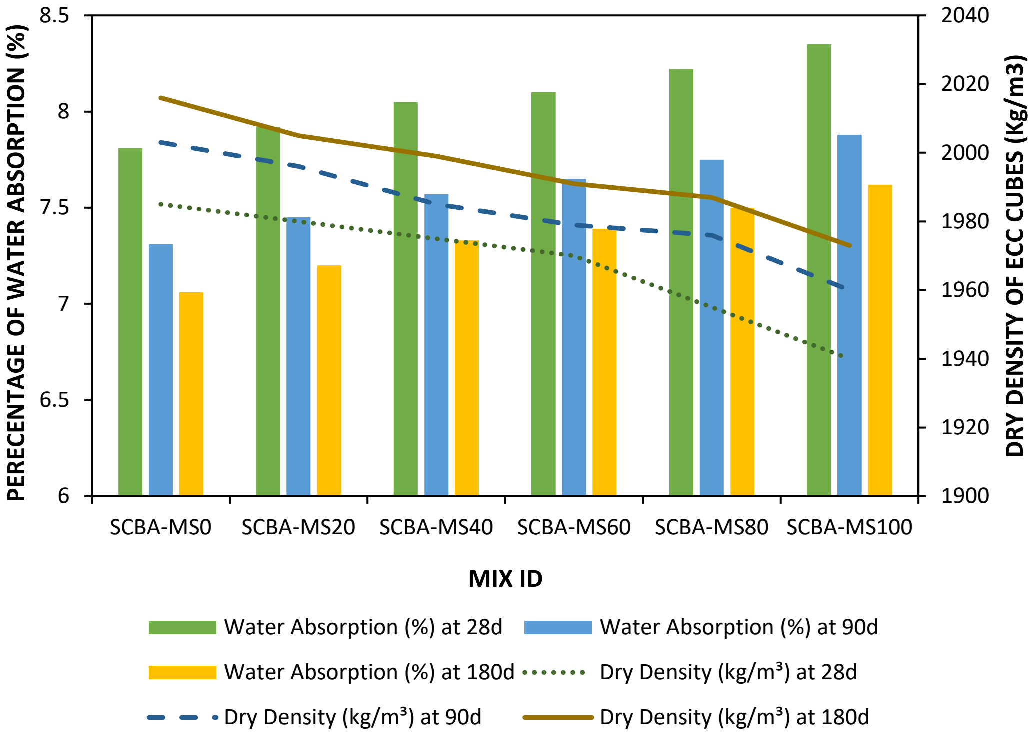

Figure 76: Water Absorption and Dry Density of ECC-SCBA (Group II) at 28, 90 and 180 Days

In contrast, dry density exhibits a downward trend as M-sand content increases (Figure 76). At 180 days, density decreases from approximately 2016kg/m³ in SCBA-MS0 to about 1973 kg/m³ in SCBA-MS100. This decrease is due to the decrement in specific gravity of SCBA and its tendency to introduce microstructural voids. Moreover, higher M-sand content does not sufficiently counterbalance the lightweight, porous nature of SCBA, leading to lower overall matrix compactness. Although minor increases in density are observed over time due to late pozzolanic reactions, these are not substantial enough to reverse the declining trend. Together, these results suggest that increased SCBA and M-sand contents negatively influence both density and water resistance, underlining the importance of careful proportioning in ECC mix design.

4.4.2 Water Permeability

The Figure 77 presents the coefficient of permeability for both ECC-FA (Group I) and ECC-SCBA (Group II) mixes across different M-sand replacement levels. It is evident that FA-based mixes consistently exhibit lower permeability compared to their SCBA counterparts at each corresponding mix ratio. For example, at 0% M-sand replacement, the permeability for the FA-MS0 mix is approximately 7.02 × 10^{-10} m/s, while the SCBA-MS0 is significantly higher at around 13.2 × 10^{-10} m/s. This trend continues across all mix levels, highlighting the relatively more porous and permeable nature of SCBA-containing ECCs.

The increase in permeability in SCBA mixes can be attributed to several factors. SCBA is highly porous and contains irregularly shaped particles, this may result in poor packing density and higher interconnected voids within the ECC matrix. This, combined with the fact that SCBA has a lower pozzolanic reactivity compared to FA, results in slower and less efficient matrix densification, allowing for greater fluid penetration. Additionally, as M-sand content increases from 0% to 100%, permeability generally rises in both mix types. This is likely due to the coarser particle structure and angular shape of M-sand compared to river sand, leading to less compact matrices with higher capillary pathways.

Notably, the lowest permeability in both FA and SCBA systems is observed at 60% M-sand replacement (FA-MS60 and SCBA-MS60), suggesting an optimal balance between workability and particle packing at this replacement level. This indicates that moderate substitution levels might improve microstructure through better pozzolanic synergy and reduced bleeding, enhancing overall matrix compactness.

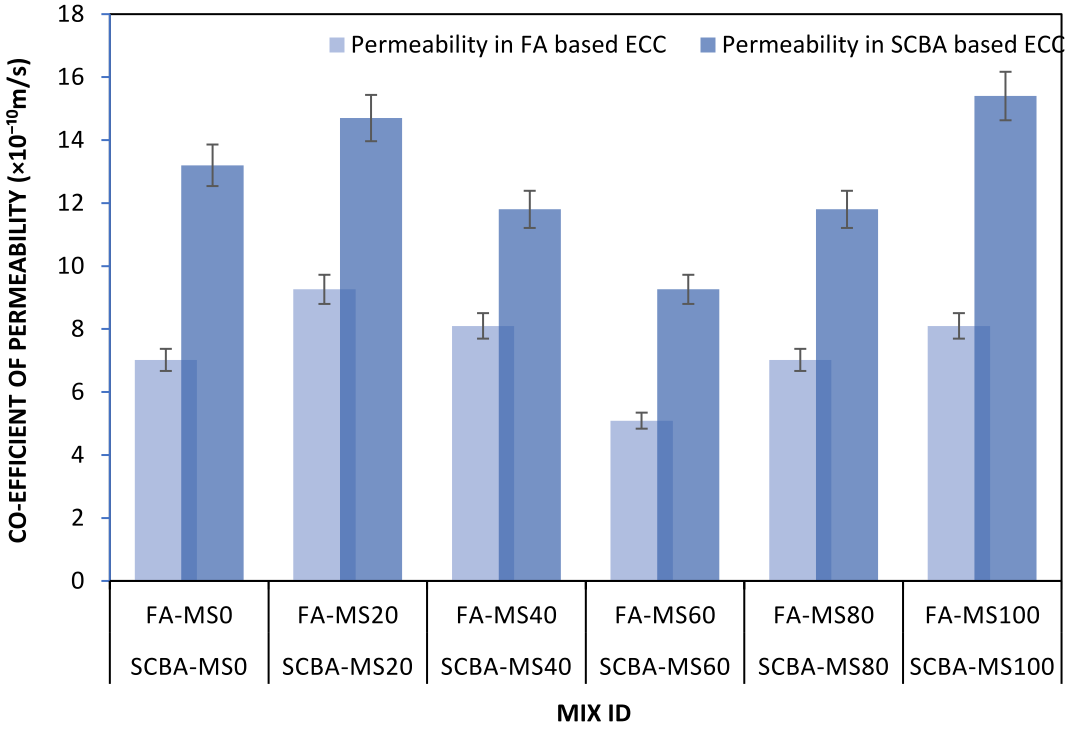

Figure 77: Water Permeability of All ECC Mixes

4.4.3 Sulphate Attack

The resistance of ECC mixes to sulphate attack was evaluated through two key parameters: compressive strength retention and percentage weight loss over exposure periods of 28, 90, and 180 days. The results clearly highlight the superior performance of ECC-FA (Group I) mixes over ECC-SCBA (Group II) mixes (Figure 78). Among FA-based mixes, FA-MS60 exhibited the most favourable performance in sulphate environments, retaining the highest compressive strengths over time. FA-MS60 reached around 49.69 MPa at 180 days with minimal weight loss of below 2.24% and compressive strength loss of 18.27% at 180 days. This indicates strong microstructural stability and sulphate resistance.

In contrast, SCBA-based ECCs demonstrated comparatively reduced sulphate resistance. While SCBA-MS60 showed acceptable strength retention 41.25 MPa at 180 days, they consistently exhibited higher weight loss than their FA-based equivalents, indicating more pronounced surface degradation and internal microcracking. Notably, SCBA-MS100 showed the weakest sulphate resistance, with compressive strength dropping to 11.54% i.e. 37.87 MPa at 180 days, and recording the weight loss of about 2.45% suggesting poor long-term durability. This performance can be attributed to the relatively amorphous and porous nature of SCBA, which may lack the pozzolanic reactivity and filler effect exhibited by FA in refining the matrix.

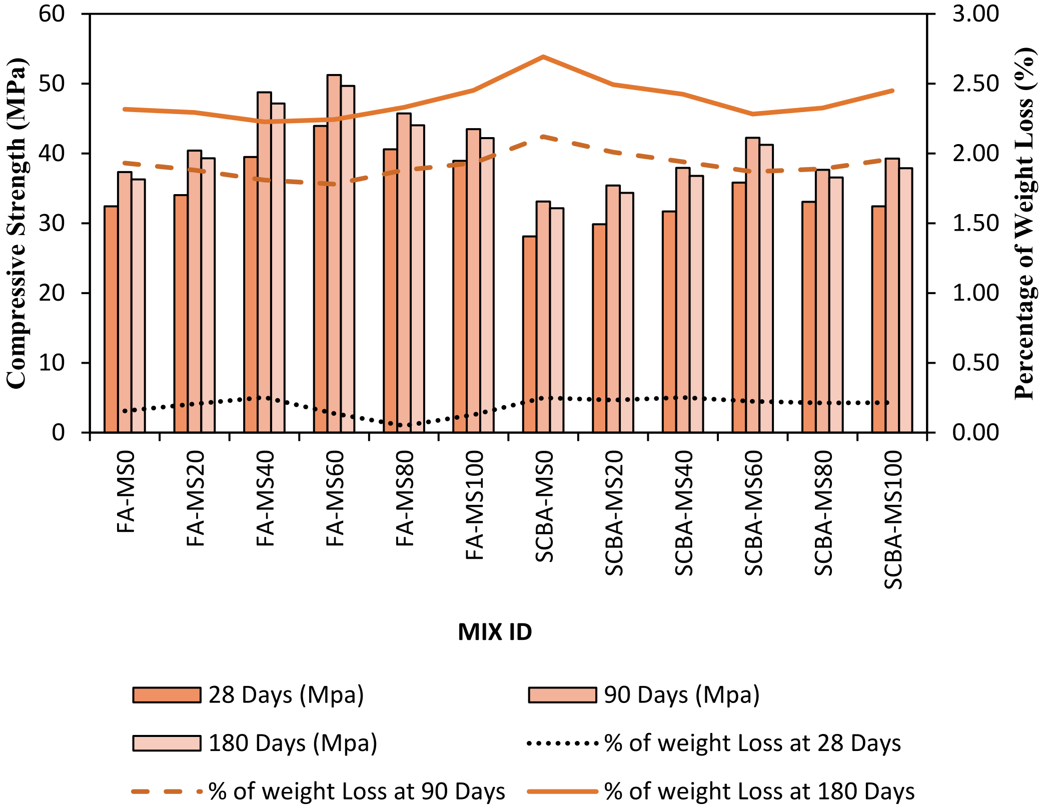

Figure 78: Sulphate Attack and Percentage of Weight Loss of ECC Cubes

4.4.4 Chloride Attack

The chloride resistance of Engineered Cementitious Composites (ECCs) was assessed by evaluating compressive strength retention and percentage weight loss after chloride exposure over 28, 90, and 180 days. The results reveal that FA-based mixes consistently outperformed SCBA-based mixes in both strength retention and minimal weight loss, indicating superior durability under chloride ingress (Figure 79). Specifically, FA-MS60 and FA-MS80 stood out, achieving the highest compressive strengths of approximately 44.23 MPa and 42.06 MPa, respectively, at 180 days. These mixes also recorded the marginal weight loss percentages, remaining below 3.5% at 28 days and staying well under 5% even at 180 days, indicating excellent resistance to chloride-induced deterioration. This suggests that these mixes have a dense microstructure and reduced permeability, likely due to the synergistic action of FA, which improves the formation of C-S-H gel and refines pore structure.

In contrast, SCBA-based mixes, while still performing reasonably well, showed relatively higher weight losses and lower compressive strengths. SCBA-MS60 and SCBA-MS80 reached 32.85 MPa and 36.77 MPa at 180 days, but their weight loss values climbed closer to 5%, indicating greater vulnerability to chloride penetration and surface degradation. Among all SCBA mixes, SCBA-MS100 was the least resistant, with the lowest compressive strength (34.04 MPa at 180 days) and the weight loss approaching 5.18%, highlighting a pronounced susceptibility to chloride attack. The increased porosity and variable reactivity of SCBA likely contributed to the higher permeability and less effective resistance compared to FA mixes.

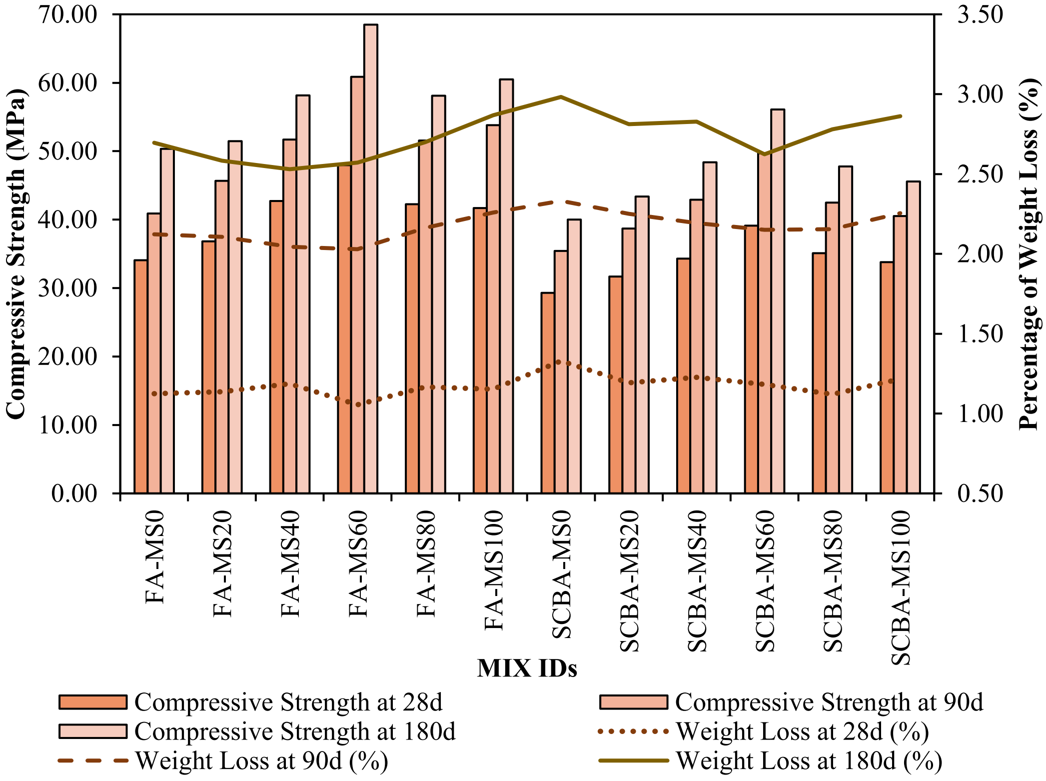

Figure 79: Chloride Attack and Percentage of Weight Loss of all ECC mixes

4.4.5 Rapid Chloride Penetration Test

In this study, twelve mixes were evaluated, categorized into two groups based on the supplementary cementitious material (SCM) used: FA and SCBA. Each group consisted of mixes with M-Sand replacement ranging from 0% to 100% in increments of 20% (Figure 81).

The FA-based mixes from Group I (FA-MS0 to FA-MS100) demonstrated a clear trend of decreasing charge passed over time, indicating an improvement in durability with age due to the ongoing pozzolanic activity of fly ash. Among these, FA-MS0 recorded the lowest charge passed at 180 days (897 C), showing excellent chloride resistance. This behaviour can be attributed to the use of 100% natural sand, which likely resulted in better particle packing and enhanced the pozzolanic reaction of fly ash, leading to a denser matrix. As the percentage of M-Sand increased, a slight deterioration in performance was observed. FA-MS20 and FA-MS40 exhibited good resistance, but marginally higher charges (977 C and 1031 C, respectively) suggest that M-Sand slightly compromised matrix refinement. FA-MS60 had a similar charge to FA-MS40, indicating a limit where M-Sand's effect and fly ash's benefit balance out. FA-MS80 and FA-MS100 showed significantly higher RCPT values (1209 C and 1347 C), likely due to increased surface roughness and angularity of M-Sand, leading to higher porosity and reduced workability.

In contrast, the SCBA-based mixes (SCBA-MS0 to SCBA-MS100) displayed a consistently higher range of RCPT values across all curing ages when compared to the FA-based mixes. SCBA-MS0 performed the best in this group with a charge of 1297 C at 180 days, suggesting that natural sand, when used with SCBA, could still provide reasonable durability. However, with increasing M-Sand content, the performance gradually declined. SCBA-MS20 and SCBA-MS40 recorded charges of 1377 C and 1431 C, respectively, reflecting reduced refinement and possible challenges in workability. Beyond 40% M-Sand replacement, a substantial increase in charge was noted. SCBA-MS60 (1502 C), SCBA-MS80 (1609 C), and SCBA-MS100 (1747 C) all indicated a marked drop in chloride resistance. This behaviour can be credited to the comparatively lower reactivity of SCBA compared to FA, coupled with the void-forming tendency of M-Sand at higher replacement levels.

Comparatively, the fly ash-based ECC mixes showed significantly better chloride resistance at all ages than the SCBA-based mixes. The best-performing mix overall was FA-MS0, which saw a 56.9% reduction in RCPT values from 28 days to 180 days, showcasing strong long-term densification. Among the SCBA mixes, SCBA-MS0 exhibited the best reduction (49.0%) but still had higher charge values than its FA counterpart. The increasing trend in charge passed with higher M-Sand replacement suggests that while M-Sand can be used as a sustainable alternative to natural sand, its proportion must be controlled. Replacement beyond 40% tends to increase permeability, mainly due to reduced workability, inadequate compaction, and the formation of interconnected voids.

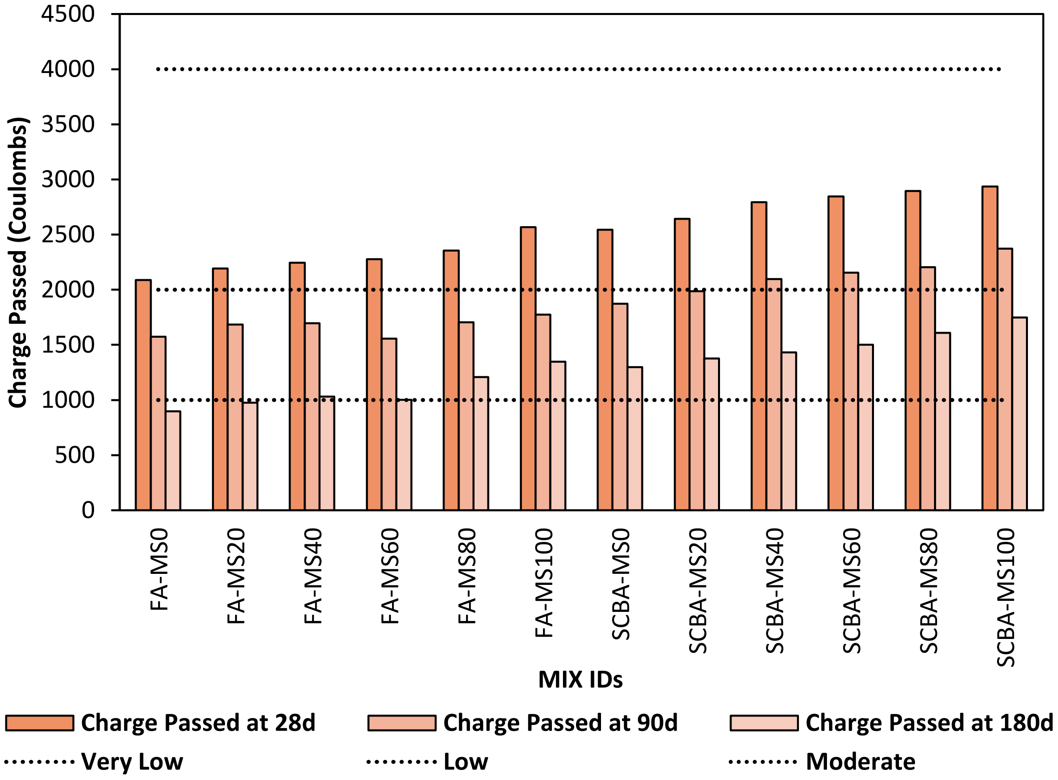

Figure 80: RCPT of all mixes of ECC at 28, 90, 180 Days

4.5 Finite Element Analysis

The FA-MS60 mix showed the best mechanical properties, with a compressive strength of 43.98 MPa and a direct-tensile strength of 7.14 MPa at 28 days. These results were validated using two Finite Element Analysis (FEA) models in ABAQUS: an ECC cube for compressive stress and an ECC coupon for tensile stress.

4.6 Development of FEA Models

4.6.1 Compressive Stress FEA Model

The cube specimen was modelled as a 3D deformable body with dimensions 70.6 mm × 70.6 mm × 70.6 mm to simulate stress-strain behaviour under compression, following standard testing protocols. The loading and support plates were modelled as 3D rigid bodies with a diameter of 150 mm and thickness of 25 mm to ensure uniform load distribution and replicate experimental conditions. Experimental yield stress and strain data were incorporated into the FEM model to capture the non-linear tensile behaviour of ECC and a mass density of 2143 kg/m^3, Young's modulus of 25.1 GPa, and Poisson's ratio of 0.15 were assigned. A static general step was used for simulating the compressive behaviour of ECC under gradual load application. To ensure even distribution of compressive force across the ECC cube specimen, a consistent pressure load was applied to the upper surface of the rigid loading plate, while the lower support plate was kept fixed. The cube was meshed using linear hexahedral elements (C3D8R), whereas the loading and support plates were meshed using linear triangular elements (R3D4).

4.6.2 Tensile Stress FEA Model

The direct tensile test assembly included a 3D deformable coupon measuring 300 mm × 50 mm × 15 mm to simulate tensile stress distribution and capture stress-strain behaviour. Catchers, modelled as 3D rigid bodies with dimensions 150 mm × 100 mm, ensured accurate and uniform load application. It was assigned with a Young's modulus of 2,000 MPa for tensile strength, reflecting its strain-hardening behaviour and reduced stiffness under tension. A dynamic explicit step was employed to capture the material's non-linear behaviour under dynamic tensile loading conditions. For tensile stress analysis, constant displacement forces are applied to the catchers in the positive and negative Y-directions to create tensile loading. The ECC coupon was meshed using linear hexahedral elements (C3D8R) and the holding catchers, modelled as discrete rigid bodies, were meshed using linear triangular elements (R3D4).

4.7 Stress and Strain generation

4.7.1 Compressive Strength FEA

The simulation of stress and strain distribution due to compressive stress of ECC cube is shown in Figures 81–84. The top and bottom plates, modelled as discrete rigid bodies, did not generate stress but allowed strain to develop in the top plate, ensuring uniform load transfer without distortion. Figure 82 is showing overall stress concentration within the ECC cube, with no stress in the rigid plates. Figure 83 is highlighting equivalent (von Mises) stress, which peaked beneath the loading plate and decreased toward the bottom.

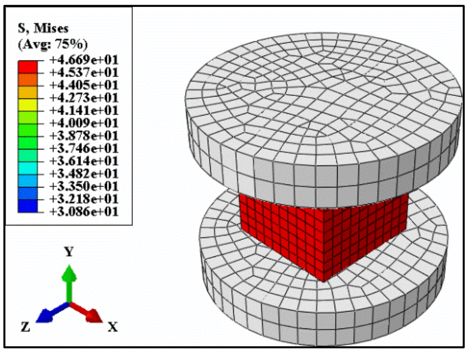

Figure 81 Stress Generation in whole assembly.

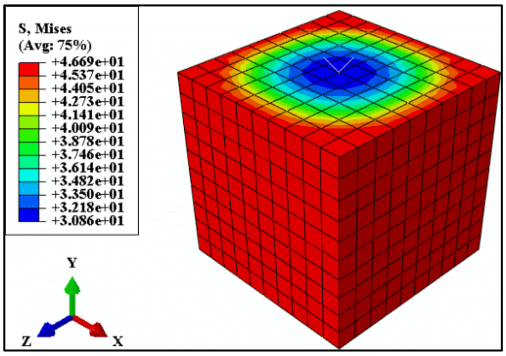

Figure 82 Stress mises in cube.

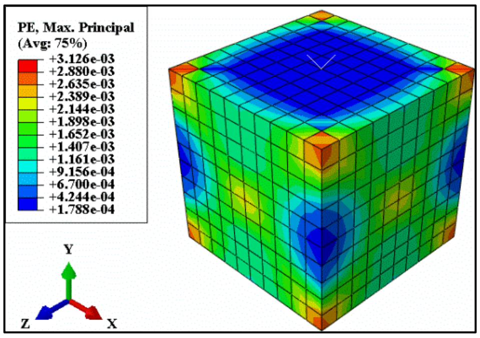

Figure 83 Plastic strain (Maximum Principle) generation in Cube.

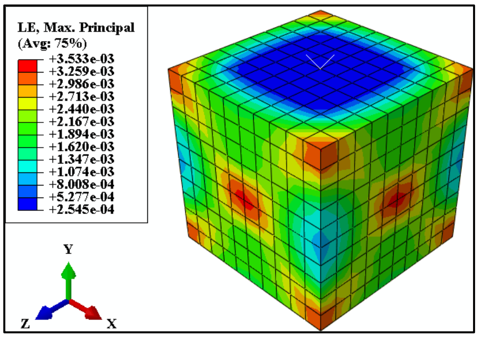

Figure 84 Linear strain (Maximum Principle) generation in Cube.

Figures 84 and 85 are depicting plastic and elastic strain distributions, respectively, showing strain concentration near the contact surfaces and a uniform spread throughout the cube.

4.7.2 Direct-Tensile Strength FEA

The tensile strength FEA analysed stress, strain, and displacement in the ECC coupon under tensile loading. The catchers, modelled as discrete rigid bodies, did not exhibit stress or plastic strain, ensuring accurate load transfer without deformation (Figure 86). Figure 86 showed stress concentrations in the coupon's middle region near the tie interaction. This behaviour is indicative of ECC's strain-hardening capability under tensile forces. Figure 87 highlighted von Mises stress, with peak values in the central region aligned with tensile forces. Plastic strain (Figure 88) was concentrated in the middle, indicating ECC's strain-hardening behaviour. Figure 89 depicted symmetric deformation along the Y-axis, with maximum displacements at the coupon's top and bottom ends.

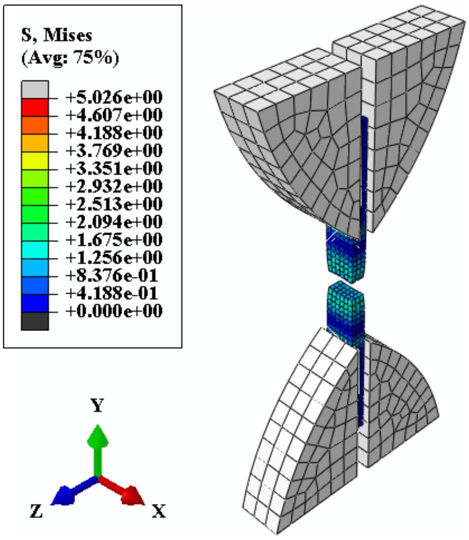

Figure 85 Stress Generation in whole assembly.

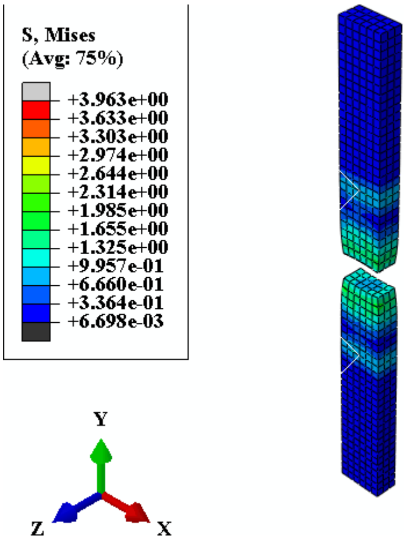

Figure 86 Stress mises in cube.

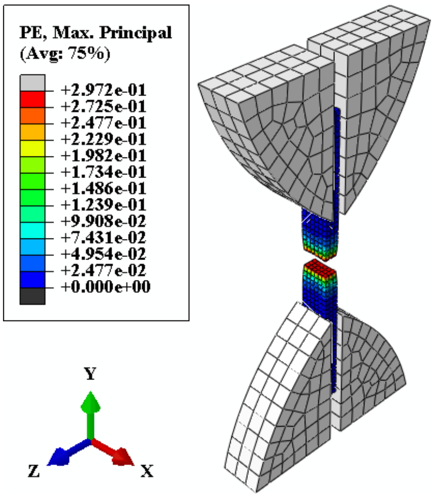

Figure 87 Plastic strain (Maximum Principle) generation in Cube.

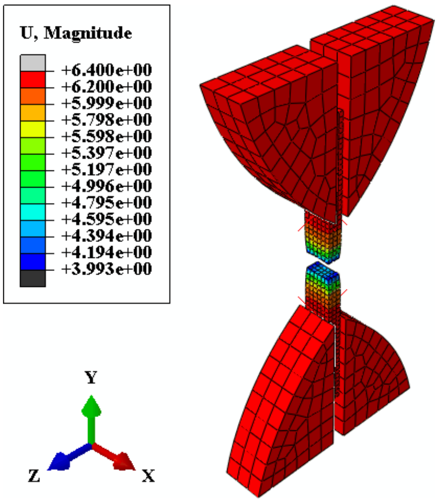

Figure 88 Displacement generation in Cube.

4.8 Validation of Experimental Results

4.8.1 Compressive Strength

The experimental compressive stress–strain curve obtained from testing of the ECC cube specimen at 28 days was used to calibrate the material behavior adopted in the finite element model. The FEM-generated stress–strain curve represents the numerical response of the ECC cube under uniform compressive loading applied in ABAQUS. Both experimental and FEM curves are presented together to demonstrate the ability of the numerical model to capture the compressive behavior of ECC. The validation of the experimental data with FEM results is performed by graphical comparing shown in Figure 90 illustrating the stress-strain behaviour of ECC Cube under compressive loading.

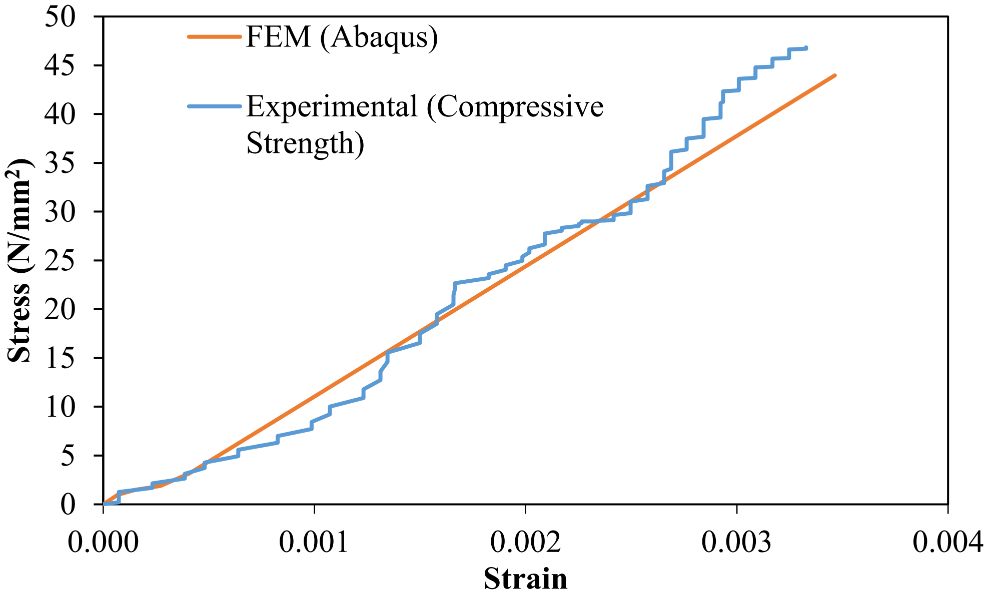

Figure 89 Comparison of Experimental and FEM Results for Compressive Strength.

The experimental curve (True Stress and Strain) and FEM simulation curve (ABAQUS) exhibit close agreement throughout the loading process, with only minor deviations observed at higher strain levels.

Not only this, but this comparison was further carried out using seven statistical techniques, as summarized in Table 21. These techniques include Root Mean Square Error (RMSE), Mean Square Error (MSE), Mean Absolute Error (MAE), Mean Bias Error (MBE), Coefficient of Determination (R^2), Normalized Root Mean Square Error (NRMSE), and Pearson Correlation Coefficient (PCC). The low RMSE (2.79), MAE (2.39), and NRMSE (0.07) values indicate minimal discrepancies between the FEM predictions and experimental results. The high values of R^2 (0.95) and PCC (0.99) further confirm a strong correlation and predictive accuracy of the FEM model.

Table 18 Statistical Validation Metrics for Experimental and FEM Results.

Statistical Tools	**RMSE**	**MSE**	**MAE**	**MBE**	**R^2**	**NRMSE**	**PCC**
Compressive Strength	2.79	7.76	2.39	2.33	0.95	0.07	0.99

This alignment validates the accuracy of the FEM model in capturing the mechanical response of ECC. Together, the statistical metrics and the stress-strain comparison demonstrate the robustness of the FEM model in replicating experimental behaviour, making it a reliable tool for analysing the compressive strength of ECC. These results support the use of FEM for predictive analysis and material design optimization in structural engineering applications.

4.8.2 Tensile Strength

The experimental direct tensile stress–strain curve obtained from coupon specimen testing was used to define the tensile material response for the finite element analysis. The corresponding FEM stress–strain curve represents the numerical prediction of tensile behavior under displacement-controlled loading. Comparative presentation of experimental and FEM curves is used to validate the accuracy of the numerical model in reproducing the tensile response of ECC. The validation of the tensile strength analysis with FEA model is conducted by comparing the simulated results with experimental data. Figure 91 presents the stress-strain behaviour of the ECC coupon under tensile loading, showing a close agreement between the FEM (ABAQUS) predictions and the experimental results. While minor deviations are observed at higher strain levels, the overall trend aligns well, demonstrating the accuracy of the FEM model in replicating the tensile behaviour of ECC. To quantitatively assess the model's accuracy, seven statistical metrics are evaluated, as summarized in Table 22. These include RMSE, MSE, MAE, MBE, R^2, NRMSE, and PCC. The results indicate excellent agreement, with an R^2 value of 0.98701 and a PCC value of 0.98289, reflecting a strong correlation between the FEM and experimental data. The low RMSE (0.51413) and NRMSE (0.10230) further confirm minimal discrepancies between the two datasets. This validation establishes the reliability of the FEM model for predicting the tensile behaviour of ECC. The statistical and graphical comparison demonstrates the robustness of the model in capturing the mechanical performance of ECC under tensile loads.

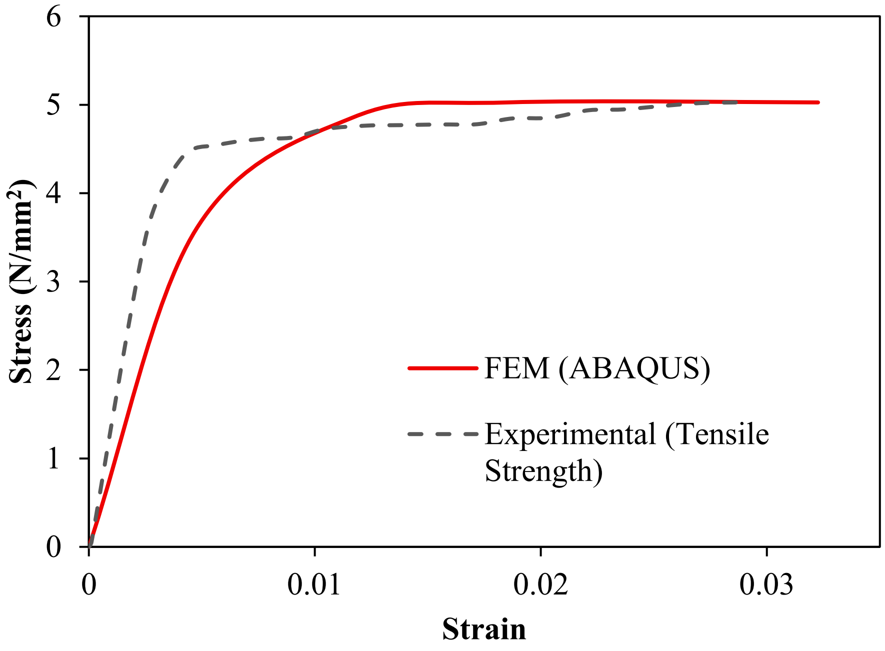

Figure 90 Stress-Strain Comparison of FEM (ABAQUS) and Experimental Results for Tensile Strength.

Table 19 Statistical Validation Metrics for Experimental and FEM Results for Tensile Strength Analysis.

Statistical Tool	RMSE	MSE	MAE	MBE	R2	NRMSE	PCC
Tensile Strength	0.51413	0.26433	0.30526	0.18228	0.98701	0.10230	0.98289

4.9 Scanning Electron Microscopy (SEM) analysis

The difference in morphology of the tested specimens was examined using Scanning Electron Microscopy (SEM. Small fragments were extracted from the fractured surfaces of the coupon specimens of 28 days for sample preparation. Figure 91(a), Figure 91(b), and Figure 91(c) shows the images of FA-MS0, FA-MS60 and FA-MS100. As observed in Figure 91(a), numerous semi-spherical pits were present, likely formed due to the detachment of unreacted FA particles that remained adhered to the opposite fracture surface, leaving behind smooth-walled cavities. In addition, slender voids were observed, which can be attributed to the debonding of PVA fibers from the cementitious matrix, primarily due weak interlocking in the presence of smooth and rounded RS particles, during tensile loading. Furthermore, large calcium hydroxide (CH) crystals were observed within the matrix, while in certain regions, calcium silicate hydrate (C-

S-H) and micro-cracks were also formed. Figure 91(b), representing FA-MS60 mix, revealed a relatively dense and well-compacted matrix with minimal large voids, indicating efficient particle packing and reduced porosity. In comparison to the FA-MS0 mix, a higher number of CH crystals were observed; however, this was accompanied by slightly wider and more frequent microcracks, likely due to the increased brittleness of the matrix resulting from excessive CH formation. The number of slender voids resulting from debonding of PVA fibers from the matrix was competitively low. In many regions, embedded fibers were observed with their free ends exhibiting flat or inclined rapture, indicating tensile failure of the fibers rather than pull out. Their embedment can be primarily attributed to the improved fiber-matrix interlocking facilitated by the presence of 60% M-Sand, characterized by its irregular shape and rough textured surface. A few irregularly shaped voids, potentially from entrapped air or partial hydration, are scattered in some regions. In Figure 91(c), the SEM microstructure of the FA-MS100 mix, revealed a dense but homogeneous matrix. While M-Sand's angular and rough-textured particles enhanced mechanical interlocking, their 100% presence appeared to reduce the overall packing efficiency, leading to localized porosity and weaker regions. Several irregularly shaped voids and wider microcracks were evident, indicating potential stress concert rations and increased brittleness. The interfacial bonding between the sand particles and cementitious paste was moderately strong, though interfacial transition zone (ITZs) appears more pronounced in certain areas. Hydration products were present, but with limited C-S-H gel and poorly defined CH crystals in some zones, suggesting non-uniform hydration. The minimum presence of slender voids associated with fiber pull-out further implies a dominance of fiber rupture, likely influenced by rough and angular sand matrix. These observations suggests that 100% M-sand improvs interlocking, it may also contribute to reduced microstructural uniformity and increased cracking tendency.

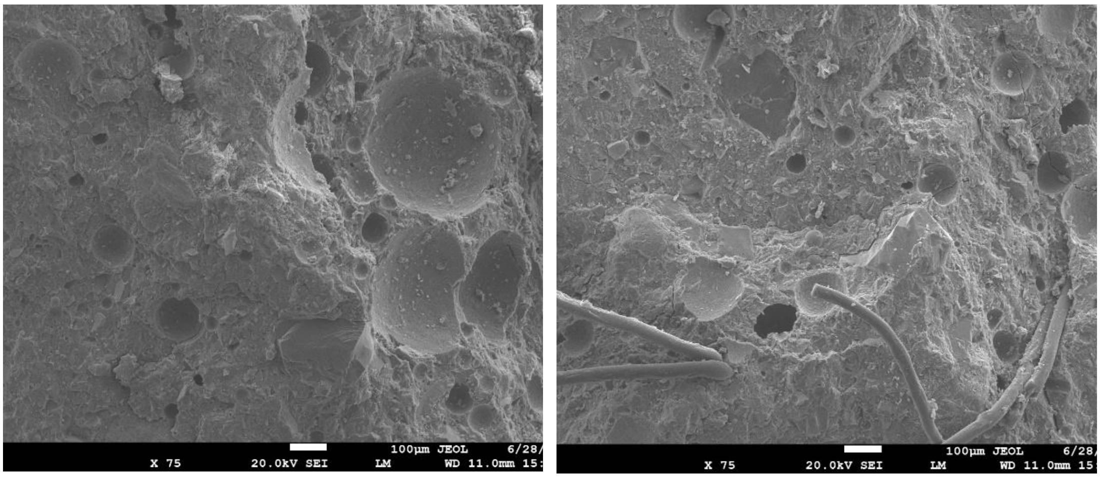

(a) SEM of FA-MS0 (b) SEM of FA-MS60

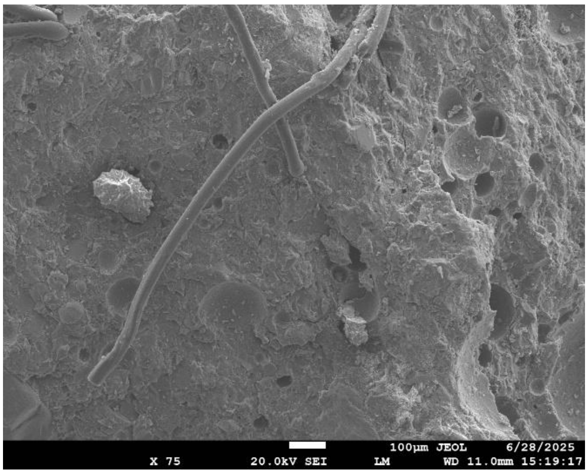

(c) SEM of MS-FA100

Figure 91:SEM images of (a) FA-MS0, (b) FA-MS60 and (c) FA-MS100

4.10 Summary

This chapter is dedicated to presenting and analysing the outcomes of the experimental program and numerical simulations conducted on various ECC mixes. This section begins with the assessment of workability, focusing on the flowability of different ECC mixes using varying proportions of FA, SCBA, and M-sand. The discussion revolves around how these ingredients influence the rheology and mix consistency. The chapter then moves to evaluate mechanical behaviour through compressive strength, direct tensile strength, and flexural strength tests. Each property is examined at multiple curing ages to understand strength development over time. The influence of varying binder types and sand replacements on mechanical performance is thoroughly discussed. A significant portion is devoted to assessing the long-term performance of ECC under environmental stressors. Tests include water absorption, water permeability, sulphate attack, chloride attack, and the Rapid Chloride Penetration Test (RCPT). These tests simulate aggressive conditions to evaluate how different ECC mixes perform in terms of resistance to degradation.

The chapter also presents the development of FEM models to simulate compressive and tensile behaviour of ECC. This includes defining model geometry, assigning material properties, setting boundary conditions, and simulating the stress-strain responses. It serves to validate experimental results and demonstrates the potential of numerical tools in predicting ECC performance. Lastly, the chapter compares the numerical results obtained from FEM models with actual experimental data. This validation ensures the accuracy of the models and builds confidence in their applicability for future ECC analysis and design. Overall, Chapter 4 integrates both experimental and computational approaches to offer a comprehensive understanding of ECC behaviour across multiple performance aspects.

CHAPTER 5

CONCLUSIONS AND RECOMMENDATION

5.1 Overview

The present research was undertaken to address the environmental and sustainability challenges associated with the excessive use of natural river sand and cement in construction, by developing an optimized Engineered Cementitious Composite (ECC) incorporating alternative fine aggregates and supplementary cementitious materials. A total of twelve ECC mixes were formulated using varying combinations of RS, M-Sand FA, and SCBA, along with cement, water, superplasticizer, and PVA fibers. These mixes were evaluated for fresh, mechanical, and durability properties through a series of standardized tests, including mini slump flow, compressive strength, direct tensile strength, flexural strength, water absorption, water permeability, sulphate and chloride attack resistance, and RCPT. The characteristic mechanical performance of selected ECC mixes was further validated using Finite Element Modelling (FEM) through ABAQUS software. In addition to investigating the possibilities of underused agro-industrial wastes in the manufacturing of ECC, this study promotes sustainable building methods by lowering reliance on river sand and decreasing environmental damage.

5.2 Summary of Key Findings

The experimental results revealed several critical insights into the performance of ECC incorporating manufactured sand (M-sand).

i. The flowability and workability of ECC mixes showed a marginal reduction with increasing M-sand content, with a maximum decline of approximately 5% for every 20% replacement of RS by M-sand. Despite this reduction, all twelve ECC mixes maintained sufficient workability suitable for ECC applications. Throughout all replacement levels, ECC-FA (Group I) consistently exhibited about 6% higher flowability than ECC-SCBA (Group II), indicating the beneficial role of fly ash in enhancing fresh-state performance.

ii. An optimum replacement level of 60% M-sand was identified for compressive strength development, resulting in an improvement of approximately 22%

compared to the control mix. The FA-MS60 mix achieved the highest compressive strength of 43.98 MPa. The combination of 40% RS and 60% M-sand proved effective for both ECC-FA and ECC-SCBA mixes due to optimal particle packing, where rounded fines fill voids between angular particles, reducing porosity and increasing the effective load-bearing area. Overall, FA-based ECC mixes achieved approximately 15–20% higher compressive strength than SCBA-based mixes.

iii. Direct tensile strength improved with increasing M-sand content up to an optimum replacement level of 60% RS. FA-based mixes, particularly FA-MS60 and FA-MS80, exhibited the highest tensile strengths of 4.88 MPa and 4.66 MPa, respectively. This enhancement is attributed to improved fiber–matrix interfacial friction from angular particles combined with matrix densification provided by finer RS, leading to uniform microcrack formation and effective fiber engagement. Although SCBA-based mixes also demonstrated strain-hardening behavior, their tensile strength was generally 10–15% lower than FA-based mixes, primarily due to lower pozzolanic activity and higher porosity of SCBA.

iv. In flexural performance, ECC-FA mixes with 60% and 80% M-sand replacement achieved peak strengths exceeding 30% improvement over the control mix, with values of 5.90 MPa and 5.85 MPa at 28 days, respectively. This improvement is attributed to refined matrix structure and improved fiber dispersion. SCBA-based mixes exhibited comparatively lower flexural strength, ranging from 4.29 MPa to 5.16 MPa, with SCBA-MS60 performing the best among them. The reduction beyond 60% replacement in SCBA mixes is associated with increased porosity and reduced fiber–matrix bonding efficiency.

v. Water absorption increased gradually with increasing M-sand replacement, by approximately 2–3% for every 20% increment. The lowest water absorption (6.79%) and highest dry density (2179 kg/m^3) were observed in FA-based ECC with 100% RS. The progressive increase in absorption with higher M-sand content is attributed to the angular nature and higher surface area of M-sand, which increases void content and facilitates greater water ingress.

vi. Permeability decreased with increasing M-sand replacement up to an optimum level of 60%, with the lowest permeability recorded for FA-MS60 at 5.09×10^{-10} m/s, representing an approximate 35% reduction compared to the control mix. This improvement indicates a denser and less permeable matrix achieved through improved gradation and packing. Beyond 60% replacement, permeability increased by approximately 30% for every additional 20% M-sand, likely due to excess angular fines and reduced interparticle efficiency.

vii. Although water absorption increases with higher M-sand replacement, the permeability of both ECC-FA and ECC-SCBA mixes decreases up to 60% replacement, indicating that these two parameters are governed by different pore characteristics. Water absorption is influenced by the total volume of accessible pores, including isolated and gel pores, whereas permeability depends primarily on the connectivity and continuity of capillary pores. Up to 60% M-sand replacement, improved particle packing, finer pore structure, and enhanced paste–aggregate interlocking lead to pore refinement and reduced capillary pore connectivity, resulting in lower permeability despite increased absorption. Beyond 60% replacement, excessive angularity of M-sand increases pore interconnection, leading to a rise in permeability, which aligns with the observed trend in both ECC-FA and ECC-SCBA mixes.

viii. ECC mixes incorporating fly ash demonstrated superior sulphate resistance compared to SCBA-based mixes. FA-MS60 exhibited the best performance, retaining a compressive strength of 49.69 MPa at 180 days with limited strength loss (18.27%) and weight loss below 2.24%. In contrast, SCBA-based mixes, particularly SCBA-MS100, showed reduced resistance due to higher porosity and lower reactivity, confirming the beneficial role of FA in enhancing long-term sulphate durability.

ix. FA-based ECC mixes exhibited significantly higher resistance to chloride attack than SCBA-based mixes. FA-MS60 and FA-MS80 retained high compressive strengths of 44.23 MPa and 42.06 MPa at 180 days with weight loss below 5%. SCBA-based mixes, especially SCBA-MS100, showed reduced resistance, indicating increased vulnerability to chloride ingress due to higher porosity and lower pozzolanic activity.

x. Chloride resistance decreased with increasing M-Sand content. Up to 40% replacement, ECC mixes—especially FA-based—maintained low RCPT values (e.g., FA-MS40: 1031 C). Beyond 40%, resistance declined notably, with FA-MS100 and SCBA-MS100 reaching 1347 C and 1747 C, respectively. The drop is due to M-Sand's angularity and poor grading, which increased porosity and reduced workability, compromising durability.

xi. The experimentally obtained direct tensile stress–strain curves exhibit higher initial stiffness than the FEM predictions due to the idealized material modeling assumptions adopted in the numerical analysis. In the FEM model, ECC was represented using homogenized material properties and smeared cracking behavior, which do not fully capture the localized fiber–matrix interaction, crack-bridging efficiency, and strain-hardening mechanisms observed in experimental specimens. Additionally, experimental boundary conditions and gripping effects contribute to higher apparent stiffness, whereas the FEM model assumes idealized loading and deformation conditions.

xii. The finite element model (FEM) in ABAQUS accurately captured the compressive stress-strain behaviour of ECC, closely aligning with experimental data. With a high coefficient of determination (R^2 = 0.95) and Pearson correlation (PCC = 0.99), along with low RMSE (2.79), the model demonstrates excellent predictive capability, validating its effectiveness for simulating compressive performance in ECC materials.

xiii. The FEM simulation of tensile strength exhibited a strong correlation with experimental results, achieving R^2 = 0.987 and PCC = 0.983. The low RMSE (0.514) and NRMSE (0.102) further confirm the model's precision. This validates the FEM's reliability in replicating the tensile behaviour of ECC, making it a dependable tool for material behaviour analysis under tensile loading.

5.3 General Conclusions

The following conclusions have been reached in accordance with the research goals based on the discussion and analysis of the study's findings.

5.3.1 Conclusion on objective 1: *To arrive at optimum Mix based on literature and various trials.*

i. Based on the literature of the trial mixes, water-to-binder (w/b) ratio of 0.27 and 0.29, a sand-to-binder (s/b) ratio of 0.40 and 0.60, with a superplasticizer-to-binder (SP/b) ratio of 0.01 and 0.02 were fixed for ECC-FA (Group I) and ECC-SCBA (Group II) respectively.

ii. The mix contained 480 kg/m³ of OPC and 512 kg/m³ of FA as the binder components, along with 405 kg/m³ of natural sand. PVA fibers were added at a dosage of 26 kg/m³, while the water and superplasticizer contents were maintained at 268 kg/m³ and 9.92 kg/m³, respectively. This composition provided an effective balance between flowability, strength, and fiber dispersion, making it the most suitable mix for further evaluation and serving as the control mix.

5.3.2 Conclusion on objective 2: *To evaluate the mechanical and durability properties of Engineered Cementitious Composite (ECC).*

i. The results demonstrated that FA-based ECC mixes consistently achieved higher compressive strengths than SCBA-based counterparts across all curing ages. The mix FA-MS60 achieved the highest compressive strength. M-sand replacement up to 60% was found to enhance strength due to better particle packing, beyond which a reduction was observed. In contrast, SCBA mixes displayed lower strength, especially beyond 60% M-sand replacement, due to the amorphous and porous nature of SCBA. This research underscores the effectiveness of FA in enhancing compressive performance and identifies the threshold for M-sand usage in ECC.

ii. Tensile strength analysis revealed the superior strain-hardening and crack-bridging ability of FA-based ECCs. Mix FA-MS60 again emerged as the best performer with tensile strength showing excellent ductility. The study established that optimal tensile performance was achieved at moderate M-sand levels (40–60%), where fiber dispersion and matrix bonding were ideal. Excessive M-sand content, especially in SCBA mixes, led to reduced tensile capacity due to poor matrix-fiber interaction. This highlights the role of fine matrix optimization for ductile ECC behaviour.

iii. ECC mixes incorporating FA showed better flexural strength development than those with SCBA, attributed to the denser microstructure and better pozzolanic activity of FA. FA-MS60 recorded the highest flexural strength, with a significant gain over time. M-sand up to 60% replacement supported flexural performance, beyond which a drop was noted. SCBA mixes lagged due to lower reactivity and microstructural weaknesses. The study confirms that controlled M-sand usage and high-reactivity SCMs like FA are crucial for achieving high flexural performance.

iv. The research identified that FA-based mixes had the lowest water absorption and permeability values, especially FA-MS60 and FA-MS40, indicating a highly refined pore structure. In contrast, SCBA mixes recorded higher values due to their porous nature. Higher M-sand content increased both water absorption and permeability, especially beyond 60%, due to poor compaction and increased porosity. These findings inform durability-oriented ECC mix design, especially for structures exposed to moisture ingress.

v. The sulphate durability tests demonstrated that FA-based ECCs, particularly FA-MS60, offered superior resistance, maintaining high strength and low weight loss over 180 days. SCBA mixes, although moderately resistant, exhibited higher degradation and lower strength retention. This behaviour is attributed to the better matrix densification and chemical stability imparted by FA. The results indicate that FA-rich matrices are better suited for sulphate-exposed environments, and the role of M-sand must be controlled to retain resistance.

vi. FA-based ECCs again outperformed SCBA-based mixes in chloride environments. FA-MS60 and FA-MS80 maintained high compressive strength and low weight loss, indicating excellent resistance to chloride-induced deterioration. Conversely, SCBA-MS100 showed the lowest resistance. The synergy between FA and metakaolin was critical in refining the microstructure and reducing permeability. These results highlight the potential of FA-based ECCs for use in chloride-prone environments like coastal infrastructure.

vii. RCPT results confirmed that FA-based ECCs significantly restricted chloride ion penetration compared to SCBA mixes. FA-MS0 showed the lowest charge passed, with a 56.9% reduction from 28 days, highlighting strong densification. In contrast, SCBA-MS100 recorded the highest charge, indicating high permeability. M-sand replacement beyond 40% consistently increased the charge passed for both SCM types.

5.3.3 Conclusion on objective 3: *To validate the obtained mechanical results of the study by using simulation software.*

i. The finite element model (FEM) developed using ABAQUS was successfully validated against experimental compressive strength results. The model accurately simulated the stress-strain response with minor deviations, achieving high R^2 (0.95) and PCC (0.99), along with low RMSE (2.79). These outcomes validate the FEM approach as a powerful predictive tool for simulating ECC compressive performance and support its use for design optimization and structural evaluation.

ii. FEM simulations of tensile behaviour closely matched the experimental results, with high R^2 (0.987) and PCC (0.983), and a low RMSE of 0.514. The results confirm that the numerical model can effectively replicate the complex tensile response of ECC, including strain hardening behaviour. This contributes significantly to the use of computational models in understanding and predicting ECC performance under tensile loads, supporting efficient material development and structural applications.

5.4 Advancement of Knowledge and Practice

The present research advances existing knowledge on engineered cementitious composites by systematically demonstrating the combined use of manufactured sand and alternative supplementary cementitious materials in ECC. While most existing studies rely on river sand and fly ash, this work establishes that manufactured sand can replace river sand up to an optimal level of 60% without compromising workability, mechanical performance, tensile ductility, or durability. This finding provides a clear, experimentally validated guideline for sustainable ECC mix design.

The study further contributes to ECC material science by quantifying the comparative performance of fly ash and sugarcane bagasse ash within the same ECC framework. Although FA-based ECC exhibited superior flowability, tensile ductility, and durability, the results confirm that SCBA-based ECC can still achieve adequate strain-hardening behavior and strength when proportioned appropriately, supporting the practical use of locally available agricultural waste as a supplementary cementitious material.

From a durability perspective, the research clarifies the non-linear relationship between water absorption and permeability, showing that pore connectivity rather than total porosity governs transport properties in ECC. This insight refines conventional interpretations of durability indicators and provides a more accurate basis for material selection in aggressive environments.

Finally, the integration of experimental testing with finite element modeling demonstrates the reliability of FEM tools for predicting ECC behavior, while also identifying limitations related to stiffness prediction. This combined experimental–numerical approach enhances confidence in using FEM for ECC design and analysis, thereby bridging the gap between laboratory research and structural-level applications.

5.4 Future Scope

- Further research is needed to reduce the high material cost of ECC by exploring cost-effective fiber alternatives, locally available industrial by-products, and optimized mix designs. Investigation into different types and proportions of supplementary cementitious materials (SCMs) beyond FA and SCBA, such as GGBS, metakaolin, and rice husk ash, could enhance sustainability and performance.
- Future work should incorporate rheological parameters like yield stress, plastic viscosity, and setting time. Effects of varying superplasticizer (SP) and viscosity-modifying agent (VMA) dosages on flow and fiber dispersion should be explored for better workability control. Fiber characterization (length, aspect ratio, surface treatment) and their influence on fresh behavior remain unexplored and warrant detailed examination.

- Microstructural analysis of fiber distribution (via imaging or sectioning) could help link fiber clumping with strength reductions observed at higher dosages. Broader evaluation across various fiber types (e.g., PE, steel, or hybrid fibers) and dosages could establish more generalized conclusions.
- Future studies should investigate flexural toughness, ductility indices, and energy absorption to fully understand ECC's post-crack behavior. Direct imaging techniques could provide insight into fiber bridging, crack propagation, and failure modes under flexure. The effect of environmental conditions (e.g., humidity, temperature variation) on fiber-matrix bonding and flexural strength should be explored.
- Durability testing should be extended to include long-term exposure durations (e.g. 365 or more days) to capture progressive deterioration. Advanced tests such as sorptivity, drying shrinkage, carbonation depth, and freeze-thaw resistance should be integrated into future studies. Microstructural observations (e.g., SEM, XRD, MIP) are recommended to confirm mechanisms behind permeability and degradation changes.
- Detailed chloride ion profiling and visual crack inspection could improve understanding of ingress mechanisms. Longer-term studies under chloride and sulphate exposure would help assess sustained durability, especially in marine or aggressive environments. Ettringite and gypsum formation should be directly measured to confirm chemical degradation pathways under sulphate attack.
- Beyond RCPT, diffusion-based methods and longer-term permeability assessments are essential for realistic durability modeling. Fiber orientation and dispersion effects on permeability should be validated through imaging or 3D tomograph.

REFERNCES

[1] G. H. Kusuma, J. Budidarmawan, and A. Susilowati, “Impact of concrete quality on sustainability,” *Procedia Eng*, vol. 125, pp. 754–759, 2015, doi: 10.1016/j.proeng.2015.11.122.

[2] T. R. Naik, “Sustainability of Concrete Construction,” *Practice Periodical on Structural Design and Construction*, vol. 13, no. 2, pp. 98–103, 2008, doi: 10.1061/(asce)1084-0680(2008)13:2(98).

[3] Q. Wang, Y. Yi, G. Ma, and H. Luo, “Hybrid effects of steel fibers , basalt fibers and calcium sulfate on mechanical performance of PVA-ECC containing high-volume fly ash,” vol. 97, no. January, pp. 357–368, 2019, doi: 10.1016/j.cemconcomp.2019.01.009.

[4] B. S. Mohammed, V. C. Khed, and M. S. Liew, “Optimization of hybrid fibres in engineered cementitious composites,” *Constr Build Mater*, vol. 190, pp. 24–37, 2018, doi: 10.1016/j.conbuildmat.2018.08.188.

[5] C. G. Christopher, R. Gopal, S. Sadasivam, A. K. Devi Keerthika Esakki, and P. Dinesh Kumar, “Experimental Toughness and Durability Evaluation of FRC Composite Reinforced with Steel–Polyester Fiber Combination,” *Int J Concr Struct Mater*, vol. 17, no. 1, 2023, doi: 10.1186/s40069-023-00599-z.

[6] C. Li, “From Micromechanics Engineering Design For Compo- Of Cementitious Engineering,” vol. 10, no. 2, 1993.

[7] V. C. Li, “Introduction to Engineered Cementitious Composites (ECC),” *Engineered Cementitious Composites (ECC)*, pp. 1–10, 2019, doi: 10.1007/978-3-662-58438-5_1.

[8] Ş. Mustafa, M. Lachemi, K. M. A. Hossain, and V. C. Li, “Cement and Concrete Research Internal curing of engineered cementitious composites for prevention of early age autogenous shrinkage cracking,” vol. 39, pp. 893–901, 2009, doi: 10.1016/j.cemconres.2009.07.006.

[9] Y. Yang, E. Yang, and V. C. Li, “Cement and Concrete Research Autogenous healing of engineered cementitious composites at early age,” *Cem Concr Res*, vol. 41, no. 2, pp. 176–183, 2011, doi: 10.1016/j.cemconres.2010.11.002.

[10] F. B. P. da Costa, D. P. Righi, A. G. Graeff, and L. C. P. da Silva Filho, “Experimental study of some durability properties of ECC with a more environmentally sustainable rice husk ash and high tenacity polypropylene fibers,” *Constr Build Mater*, vol. 213, pp. 505–513, 2019, doi: 10.1016/j.conbuildmat.2019.04.092.

[11] V. C. Li, “On engineered cementitious composites (ECC). A review of the material and its applications,” *Journal of Advanced Concrete Technology*, vol. 1, no. 3, pp. 215–230, 2003,

[12] K. Tosun-Felekoğlu, B. Felekoğlu, R. Ranade, B. Y. Lee, and V. C. Li, “The role of flaw size and fiber distribution on tensile ductility of PVA-ECC,” *Compos B Eng*, vol. 56, pp. 536–545, 2014, doi: 10.1016/j.compositesb.2013.08.089.

[13] V. C. Li, H. C. Wu, and Y. W. Chan, “Effect of plasma treatment of polyethylene fibers on interface and cementitious composite properties,” 1996. doi: 10.1111/j.1151-2916.1996.tb07932.x.

[14] S. Ranjith, R. Venkatasubramani, and V. Sreevidya, “Comparative Study on Durability Properties of Engineered Cementitious Composites with Polypropylene Fiber and Glass Fiber,” *Archives of Civil Engineering*, vol. 63, no. 4, pp. 83–101, 2017, doi: 10.1515/ace-2017-0042.

[15] S. Wang and V. C. Li, “Engineered cementitious composites with high-volume fly ash,” *ACI Mater J*, vol. 104, no. 3, pp. 233–241, 2007, doi: 10.14359/18668.

[16] F. Mahmoudi, J. A. Abdalla, R. A. Hawileh, and Z. Zhang, “An overview of mechanical properties of engineered cementitious composite (ECC) with different percentages of GGBS,” *Mater Today Proc*, vol. 65, pp. 2077–2080, 2022, doi: 10.1016/j.matpr.2022.06.448.

[17] Y. Liu, X. Zhou, C. Lv, Y. Yang, and T. Liu, “Use of Silica Fume and GGBS to Improve Frost Resistance of ECC with High-Volume Fly Ash,” *Advances in Civil Engineering*, vol. 2018, 2018, doi: 10.1155/2018/7987589.

[18] V. C. Li, T. Horikoshi, A. Ogawa, S. Torigoe, and T. Saito, “Micromechanics-based durability study of polyvinyl alcohol-engineered cementitious composite,” *ACI Mater J*, vol. 101, no. 3, pp. 242–248, 2004, doi: 10.14359/13120.

[19] Victor C.Li, “Engineered Cementitious Composites (Ecc) – Tailored Composites through Micromechanical Modeling,” *Canadian Society for Civil Engineering*, pp. 1–38, 1997.

[20] J. Qiu and E. Yang, “Cement and Concrete Research Micromechanics-based investigation of fatigue deterioration of engineered cementitious composite (ECC),” *Cem Concr Res*, vol. 95, pp. 65–74, 2017, doi: 10.1016/j.cemconres.2017.02.029.

[21] C. Lin, T. Kanstad, S. Jacobsen, and G. Ji, “Bonding property between fiber and cementitious matrix : A critical review,” *Constr Build Mater*, vol. 378, no. December 2022, p. 131169, 2023, doi: 10.1016/j.conbuildmat.2023.131169.

[22] J. Yu, H. Li, C. K. Y. Leung, X. Lin, J. Y. K. Lam, and I. M. L. Sham, “Matrix design for waterproof Engineered Cementitious Composites (ECCs),” *Constr Build Mater*, vol. 139, pp. 438–446, 2017, doi: 10.1016/j.conbuildmat.2017.02.076.

[23] V. C. Li, *Micromechanics and Engineered Cementitious Composites (ECC) Design Basis*. 2019. doi: 10.1007/978-3-662-58438-5_2.

[24] V. C. Li, “Engineered cementitious composite (ecc): Material, structural, and durability performance,” *Concrete Construction Engineering Handbook, Second Edition*, no. June 2011, pp. 1001–1048, 2008.

[25] V. C. Li, C. Wu, S. Wang, A. Ogawa, and T. Saito, “Interface tailoring for strain-hardening polyvinyl alcohol-engineered cementitious composite (PVA-ECC),” *ACI Mater J*, vol. 99, no. 5, pp. 463–472, 2002, doi: 10.14359/12325.

[26] V. C. Li, “From micromechanics to structural engineering -the design of cementitious composites for civil engineering applications,” *Structural Engineering/Earthquake Engineering*, vol. 10, no. 2, pp. 1–34, 1994.

[27] D. Zhang, J. Yu, H. Wu, B. Jaworska, B. R. Ellis, and V. C. Li, “Discontinuous micro-fibers as intrinsic reinforcement for ductile Engineered Cementitious Composites (ECC),” *Compos B Eng*, vol. 184, no. March 2019, p. 107741, 2020, doi: 10.1016/j.compositesb.2020.107741.

[28] C. Ding, L. Guo, B. Chen, Y. Xu, Y. Cao, and C. Fei, “Micromechanics theory guidelines and method exploration for surface treatment of PVA fibers used in high-ductility cementitious composites,” *Constr Build Mater*, vol. 196, pp. 154–165, 2019, doi: 10.1016/j.conbuildmat.2018.11.118.

[29] V. C. Li, S. Wang, and C. Wu, “Tensile strain-hardening behavior or polyvinyl alcohol engineered cementitious composite (PVA-ECC),” *ACI Mater J*, vol. 98, no. 6, pp. 483–492, 2001, doi: 10.14359/10851.

[30] M. Hou and V. C. Li, “Materials & Design Tailoring crack width control of LC3-based engineered cementitious composites (ECC) via fiber hybridization : From micromechanics design to macro investigation,” *Mater Des*, vol. 235, no. October, p. 112433, 2023, doi: 10.1016/j.matdes.2023.112433.

[31] Y. Bayapureddy, K. Muniraj, and M. R. G. Mutukuru, “Sugarcane bagasse ash as supplementary cementitious material in cement composites: strength, durability, and microstructural analysis,” *Journal of the Korean Ceramic Society*, vol. 57, no. 5, pp. 513–519, 2020, doi: 10.1007/s43207-020-00055-8.

[32] Y. Chengfang, A. Raza, A. Manan, S. Ahmad, W. Chao, and M. Umar, “Experimental and FEM analysis on the impact of Yellow River Sand replacement rate on Engineered Cementitious Composite (ECC),” *Proceedings of the Institution of Civil Engineers: Engineering Sustainability*, 2024, doi: 10.1680/jensu.23.00080.

[33] L. Liu *et al.*, “Flexural behavior of ECC reinforced RC beams under secondary load: Experimental, numerical simulation and theoretical analysis,” *Case Studies in Construction Materials*, vol. 20, Jul. 2024, doi: 10.1016/j.cscm.2024.e03340.

[34] H. Ren, F. Zhang, C. Mao, Q. Fan, and Z. Lu, “Numerical and experimental analysis in seismic performance of post-earthquake reinforced concrete frame retrofitted with ECC,” *Advances in Structural Engineering*, vol. 27, no. 1, pp. 3–16, Jan. 2024, doi: 10.1177/13694332231213456.

[35] C. Z. Woo, W. Teo, and K. Shirai, “Numerical Simulation on the Tensile Strain Hardening Behaviour Of Engineered Cementitious Composites (ECC),” *J Teknol*, vol. 84, no. 6, pp. 39–50, Nov. 2022, doi: 10.11113/jurnalteknologi.v84.18452.

[36] J. Maheswaran, M. Chellapandian, M. V. R. Sivasubramanian, G. Murali, and N. I. Vatin, “Experimental and Numerical Investigation on the Shear Behavior of Engineered Cementitious Composite Beams with Hybrid Fibers,” *Materials*, vol. 15, no. 14, Jul. 2022, doi: 10.3390/ma15145059.

[37] P. M. Arulanandam, M. V. R. Sivasubramnaian, M. Chellapandian, G. Murali, and N. I. Vatin, “Analytical and Numerical Investigation of the Behavior of Engineered Cementitious Composite Members under Shear Loads,” *Materials*, vol. 15, no. 13, Jul. 2022, doi: 10.3390/ma15134640.

[38] UNEP, “SandSust.pdf,” 2019.

[39] L. Barcelo, J. Kline, G. Walenta, and E. Gartner, “Cement and carbon emissions,” *Materials and Structures/Materiaux et Constructions*, vol. 47, no. 6, pp. 1055–1065, 2014, doi: 10.1617/s11527-013-0114-5.

[40] V. C. Li, “From micromechanics to structural engineering -the design of cementitious composites for civil engineering applications,” *Structural Engineering/Earthquake Engineering*, vol. 10, no. 2, pp. 1–34, 1994.

[41] V. C. Li, “On Engineered Cementitious Composites (ECC) A Review of the Material and Its Applications,” vol. 1, no. 3, pp. 215–230, 2003.

[42] E. H. Yang, Y. Yang, and V. C. Li, “Use of high volumes of fly ash to improve ECC mechanical properties and material greenness,” *ACI Mater J*, vol. 104, no. 6, pp. 620–628, 2007, doi: 10.14359/18966.

[43] V. C. Li, “Engineered Cementitious Composites (ECC) – Material... - Google Scholar,” 2007,

[44] E. D. Shumuye, W. Li, G. Fang, Z. Wang, J. Liu, and K. Zerfu, “Review on the durability of eco-friendly engineering cementitious composite (ECC),” *Case Studies in Construction Materials*, vol. 19, no. July, pp. e02324–e02324, 2023, doi: 10.1016/j.cscm.2023.e02324.

[45] X. H. Wang, Z. C. Fang, and L. Zheng, “Effect of Dose and Types of the Water Reducing Admixtures and Superplasticizers on Concrete Strength and Durability Behaviour: a Review,” *Journal of Civil Engineering and Management*, vol. 30, no. 1, pp. 33–48, 2024, doi: 10.3846/jcem.2024.20145.

[46] M. Şahmaran and V. C. Li, “Durability properties of micro-cracked ECC containing high volumes fly ash,” *Cem Concr Res*, vol. 39, no. 11, pp. 1033–1043, 2009, doi: 10.1016/j.cemconres.2009.07.009.

[47] V. C.Li, “On Engineered Cementitious Composites (ECC) A Review of the Material and Its Applications,” *Journal of Advanced Concrete Technology*, vol. 1, no. 3, pp. 215–230, 2003.

[48] A. E. Naaman, “Report of the RILEM International Workshop on High Performance Fiber Reinforced Cement Composites (HPFRCC-4) - Ann Arbor, Michigan, June 16-18, 2003,” *Mater Struct*, vol. 36, no. 264, pp. 710–712, 2003, doi: 10.1617/14103.

[49] V. C. Li, “Engineered Cementitious Composites (ECC) – Material , Structural , and Durability Performance,” 2007.

[50] M. Sahmaran, M. Lachemi, and V. C. Li, “Assessing mechanical properties and microstructure of fire-damaged engineered cementitious composites,” *ACI Mater J*, vol. 107, no. 3, pp. 297–304, 2010, doi: 10.14359/51663759.

[51] M. B. Weimann and V. C. Li, “Hygral Behavior of Engineered Cementitious Composites (ECC) / Vergleich der hygrischen Eigenschaften von ECC mit Beton,” *Restoration of Buildings and Monuments*, vol. 9, no. 5, pp. 513–534, 2014, doi: 10.1515/rbm-2003-5791.

[52] V. C. Li, M. D. Lepech, and M. Li, “Field Demonstration of Durable Link Slabs for Jointless Bridge Decks Based on Strain-Hardening Cementitious Composites,” *Li, V. C., Lepech, M. D., Li, M.*, no. Research Report RC-1471, p. 147, 2005, [Online]. Available: https://trid.trb.org/view/875207

[53] M. Kunieda and K. Rokugo, “Recent progress on HPFRCC in Japan required performance and applications,” *Journal of Advanced Concrete Technology*, vol. 4, no. 1, pp. 19–33, 2006, doi: 10.3151/jact.4.19.

[54] K. Rokugo, T. Kanda, H. Yokota, and N. Sakata, “Applications and recommendations of high performance fiber reinforced cement composites with multiple fine cracking (HPFRCC) in Japan,” *Materials and Structures/Materiaux et Constructions*, vol. 42, no. 9, pp. 1197–1208, 2009, doi: 10.1617/s11527-009-9541-8.

[55] K. Kesner and S. L. Billington, “Investigation of Infill Panels Made from Engineered Cementitious Composites for Seismic Strengthening and Retrofit,” *Journal of Structural Engineering*, vol. 131, no. 11, pp. 1712–1720, 2005, doi: 10.1061/(asce)0733-9445(2005)131:11(1712).

[56] M. D. Lepech and V. C. Li, “Sustainable pavement overlays using Engineered Cementitious Composites,” *International Journal of Pavement Research and Technology*, vol. 3, no. 5, pp. 241–250, 2010.

[57] M. Li and V. C. Li, “High-early-strength engineered cementitious composites for fast, durable concrete repair-material properties,” *ACI Mater J*, vol. 108, no. 1, pp. 3–12, 2011, doi: 10.14359/51664210.

[58] V. C. Li and E. N. Herbert, “Self-healing of microcracks in engineered cementitious composites (ECC) under a natural environment,” *Materials*, vol. 6, no. 7, pp. 2831–2845, 2013, doi: 10.3390/ma6072831.

[59] G. A. Keoleian *et al.*, “Life Cycle Modeling of Concrete Bridge Design: Comparison of Engineered Cementitious Composite Link Slabs and Conventional Steel Expansion Joints,” *Journal of Infrastructure Systems*, vol. 11, no. 1, pp. 51–60, 2005, doi: 10.1061/(asce)1076-0342(2005)11:1(51).

[60] K. Yu, J. Yu, J. Dai, Z. Lu, and S. P. Shah, “Development of ultra-high performance engineered cementitious composites using polyethylene (PE) fibers,” *Constr Build Mater*, vol. 158, pp. 217–227, 2018, doi: 10.1016/j.conbuildmat.2017.10.040.

[61] J. Zhou, S. Qian, M. G. S. Beltran, G. Ye, K. Van Breugel, and V. C. Li, “Development of engineered cementitious composites with limestone powder and blast furnace slag,” *Materials and Structures/Materiaux et Constructions*, vol. 43, no. 6, pp. 803–814, 2010, doi: 10.1617/s11527-009-9549-0.

[62] Z. Pan, C. Wu, J. Liu, W. Wang, and J. Liu, “Study on mechanical properties of cost-effective polyvinyl alcohol engineered cementitious composites (PVA-ECC),” *Constr Build Mater*, vol. 78, pp. 397–404, 2015, doi: 10.1016/j.conbuildmat.2014.12.071.

[63] P. Zhang, Y. Dai, X. Ding, C. Zhou, X. Xue, and T. Zhao, “Self-healing behaviour of multiple microcracks of strain hardening cementitious composites (SHCC),” *Constr Build Mater*, vol. 169, pp. 705–715, 2018, doi: 10.1016/j.conbuildmat.2018.03.032.

[64] Y. Yang, M. D. Lepech, E. H. Yang, and V. C. Li, “Autogenous healing of engineered cementitious composites under wet-dry cycles,” *Cem Concr Res*, vol. 39, no. 5, pp. 382–390, 2009, doi: 10.1016/j.cemconres.2009.01.013.

[65] H. J. Kong, S. G. Bike, and V. C. Li, “Development of a self-consolidating engineered cementitious composite employing electrosteric dispersion/stabilization,” *Cem Concr Compos*, vol. 25, no. 3, pp. 301–309, 2003, doi: 10.1016/S0958-9465(02)00057-4.

[66] M. Maalej, S. T. Quek, and J. Zhang, “Behavior of Hybrid-Fiber Engineered Cementitious Composites Subjected to Dynamic Tensile Loading and Projectile

Impact," *Journal of Materials in Civil Engineering*, vol. 17, no. 2, pp. 143–152, 2005, doi: 10.1061/(asce)0899-1561(2005)17:2(143).

[67] I. Komara, A. Tambusay, W. Sutrisno, and P. Suprobo, "Engineered Cementitious Composite as an innovative durable material: A review," *ARPN Journal of Engineering and Applied Sciences*, vol. 14, no. 4, pp. 822–833, 2019.

[68] B. Dadmand, M. Pourbaba, and R. Riahi, "Experimental and Numerical Investigation of Different Types of Jacketing Effect on Retrofitting RC Short Columns Using ECC Concrete," *Periodica Polytechnica Civil Engineering*, vol. 66, no. 2, pp. 603–613, 2022, doi: 10.3311/PPci.19114.

[69] B. Dadmand, M. Pourbaba, H. Sadaghian, and A. Mirmiran, "Experimental & numerical investigation of mechanical properties in steel fiber-reinforced UHPC," *Computers and Concrete*, vol. 26, no. 5, pp. 451–465, 2020, doi: 10.12989/cac.2020.26.5.451.

[70] X. Long, Y. Tan, X. Wan, L. Zhou, and C. Wang, "Effect of freeze-thaw cycles and chloride salt erosion coupling conditions on fatigue properties of PE-ECC," *Case Studies in Construction Materials*, vol. 20, no. October 2023, pp. e02726–e02726, 2024, doi: 10.1016/j.cscm.2023.e02726.

[71] Z. Yan, J. J. Zeng, Y. Zhuge, J. J. Liao, J. K. Zhou, and G. Ma, "Compressive behavior of FRP-confined 3D printed ultra-high performance concrete cylinders," *Journal of Building Engineering*, vol. 83, no. November 2023, p. 108304, 2024, doi: 10.1016/j.jobe.2023.108304.

[72] B. Benmokrane, C. Nazair, M. Loranger, and A. Manalo, "Field Durability Study of Vinyl-Ester – Based GFRP Rebars in Concrete Bridge Barriers," vol. 23, no. 12, pp. 1–13, 2019, doi: 10.1061/(ASCE)BE.1943-5592.0001315.

[73] Y. Liu, X. Zhou, C. Lv, Y. Yang, and T. Liu, "Use of Silica Fume and GGBS to Improve Frost Resistance of ECC with High-Volume Fly Ash," vol. 2018, 2018.

[74] A. R. Bagheri, H. Zanganeh, and M. M. Moalemi, "Mechanical and durability properties of ternary concretes containing silica fume and low reactivity blast

furnace slag," *Cem Concr Compos*, vol. 34, no. 5, pp. 663–670, 2012, doi: 10.1016/j.cemconcomp.2012.01.007.

[75] L. Wang, S. H. Zhou, Y. Shi, S. W. Tang, and E. Chen, "Effect of silica fume and PVA fiber on the abrasion resistance and volume stability of concrete," *Compos B Eng*, vol. 130, pp. 28–37, 2017, doi: 10.1016/j.compositesb.2017.07.058.

[76] K. L. Chung, M. Ghannam, and C. Zhang, "Effect of Specimen Shapes on Compressive Strength of Engineered Cementitious Composites (ECCs) with Different Values of Water-to-Binder Ratio and PVA Fiber," *Arab J Sci Eng*, vol. 43, no. 4, pp. 1825–1837, 2018, doi: 10.1007/s13369-017-2776-8.

[77] J. Il Choi, K. Il Song, J. K. Song, and B. Y. Lee, "Composite properties of high-strength polyethylene fiber-reinforced cement and cementless composites," *Compos Struct*, vol. 138, pp. 116–121, 2016, doi: 10.1016/j.compstruct.2015.11.046.

[78] C. Li, J. Li, Q. Ren, Q. Zheng, and Z. Jiang, "Durability of concrete coupled with life cycle assessment: Review and perspective," *Cem Concr Compos*, vol. 139, no. March, 2023, doi: 10.1016/j.cemconcomp.2023.105041.

[79] H. Ma, S. Qian, and Z. Zhang, "Effect of self-healing on water permeability and mechanical property of Medium-Early-Strength Engineered Cementitious Composites," *Constr Build Mater*, vol. 68, pp. 92–101, 2014, doi: 10.1016/j.conbuildmat.2014.05.065.

[80] Y. Ding, J. tao Yu, K. Q. Yu, and S. lang Xu, "Basic mechanical properties of ultra-high ductility cementitious composites: From 40 MPa to 120 MPa," *Compos Struct*, vol. 185, no. November 2017, pp. 634–645, 2018, doi: 10.1016/j.compstruct.2017.11.034.

[81] G. FISCHER, S. WANG, and V. C. LI, "Design of Engineered Cementitious Composites (Ecc) for Processing and Workability Requirements," 2003. doi: 10.1533/9780857093103.29.

[82] S. Wali *et al.*, "Case Studies in Construction Materials Performance evaluation of the fresh and hardened properties of different PVA-ECC mixes : An

experimental approach," *Case Studies in Construction Materials*, vol. 18, no. September 2022, pp. e01764–e01764, 2023, doi: 10.1016/j.cscm.2022.e01764.

[83] B. Dadmand, M. Pourbaba, H. Sadaghian, and A. Mirmiran, "Effectiveness of steel fibers in ultra-high-performance fiber-reinforced concrete construction," *Advances in Concrete Construction*, vol. 10, no. 3, pp. 195–209, 2020, doi: 10.12989/acc.2020.10.3.195.

[84] Ş. Mustafa, M. Lachemi, K. M. A. Hossain, R. Ranade, and V. C. Li, "Influence of Aggregate Type and Size on Ductility and Mechanical Properties of Engineered Cementitious Composites," no. 106, 2010.

[85] B. Merchant and A. Gelot, "Evaluation of Engineering Cementitious Composites (ECC) With Different Percentage of Fibers," *International Journal of Engineering Research and*, vol. V4, no. 06, pp. 4–8, 2015, doi: 10.17577/ijertv4is060084.

[86] A. Al-Fakih, B. S. Mohammed, and M. S. Liew, "On rubberized engineered cementitious composites (R-ECC): A review of the constituent material," *Case Studies in Construction Materials*, vol. 14, p. e00536, 2021, doi: 10.1016/j.cscm.2021.e00536.

[87] H. Su, J. Yang, T. Ling, G. S. Ghataora, and S. Dirar, "Properties of concrete prepared with waste tyre rubber particles of uniform and varying sizes," *J Clean Prod*, pp. 1–9, 2014, doi: 10.1016/j.jclepro.2014.12.022.

[88] Z. Zhang, A. Yuvaraj, J. Di, and S. Qian, "Matrix design of light weight , high strength , high ductility ECC," *Constr Build Mater*, vol. 210, pp. 188–197, 2019, doi: 10.1016/j.conbuildmat.2019.03.159.

[89] S. Wang and V. C. Li, "High-early-strength engineered cementitious composites," *ACI Mater J*, vol. 103, no. 2, pp. 97–105, 2006, doi: 10.14359/15260.

[90] M. Li and V. C. Li, "Rheology, fiber dispersion, and robust properties of engineered cementitious composites," *Materials and Structures/Materiaux et*

Constructions, vol. 46, no. 3, pp. 405–420, 2013, doi: 10.1617/s11527-012-9909-z.

[91] W. Zhang, C. Yin, F. Ma, and Z. Huang, “Mechanical properties and carbonation durability of engineered cementitious composites reinforced by polypropylene and hydrophilic polyvinyl alcohol fibers,” *Materials*, vol. 11, no. 7, 2018, doi: 10.3390/ma11071147.

[92] K. Yu, W. Mcgee, T. Yan, H. Zhu, and V. C. Li, “Cement and Concrete Research 3D-printable engineered cementitious composites (3DP-ECC): Fresh and hardened properties,” *Cem Concr Res*, vol. 143, no. May 2020, p. 106388, 2021, doi: 10.1016/j.cemconres.2021.106388.

[93] I. Abdulkadir, B. S. Mohammed, M. S. Liew, and M. M. A. Wahab, “Case Studies in Construction Materials Modelling and multi-objective optimization of the fresh and mechanical properties of self-compacting high volume fl y ash ECC (HVFA-ECC) using response surface methodology (RSM),” *Case Studies in Construction Materials*, vol. 14, pp. e00525–e00525, 2021, doi: 10.1016/j.cscm.2021.e00525.

[94] M. Singh, B. Saini, and H. D. Chalak, “Performance and composition analysis of engineered cementitious composite (ECC) – A review,” *Journal of Building Engineering*, vol. 26, no. June, p. 100851, 2019, doi: 10.1016/j.jobe.2019.100851.

[95] Q. Wang, M. H. Lai, J. Zhang, Z. Wang, and J. C. M. Ho, “Greener engineered cementitious composite (ECC) – The use of pozzolanic fillers and unoiled PVA fibers,” vol. 247, 2020, doi: 10.1016/j.conbuildmat.2020.118211.

[96] F. Mahmoudi, J. A. Abdalla, R. A. Hawileh, and Z. Zhang, “Materials Today : Proceedings An overview of mechanical properties of engineered cementitious composite (ECC) with different percentages of GGBS,” *Mater Today Proc*, vol. 65, pp. 2077–2080, 2022, doi: 10.1016/j.matpr.2022.06.448.

[97] S. Zhou, L. Xie, Y. Jia, and C. Wang, “Review review of cementitious composites containing polyethylene fibers as repairing materials,” *Polymers (Basel)*, vol. 12, no. 11, pp. 1–22, 2020, doi: 10.3390/polym12112624.

[98] M. P. Kumar, K. M. Mini, and M. Rangarajan, “Ultrafine GGBS and calcium nitrate as concrete admixtures for improved mechanical properties and corrosion resistance,” *Constr Build Mater*, vol. 182, pp. 249–257, 2018, doi: 10.1016/j.conbuildmat.2018.06.096.

[99] K. Turk and M. L. Nehdi, “Flexural toughness of sustainable ECC with high-volume substitution of cement and silica sand,” no. xxxx, 2020.

[100] J. Y. Wang, K. S. Chia, J. Y. R. Liew, and M. H. Zhang, “Flexural performance of fiber-reinforced ultra lightweight cement composites with low fiber content,” *Cem Concr Compos*, vol. 43, pp. 39–47, 2013, doi: 10.1016/j.cemconcomp.2013.06.006.

[101] H. E. Yücel, S. Demirhan, M. T. Arık, and V. C. Li, “Combined Effect of Aggregate and Mineral Admixtures on Tensile Ductility of Engineered Cementitious Composites,” *ACI Mater J*, vol. 109, no. 6, pp. 627–638, 2012, doi: 10.14359/51684160.

[102] W. Li, Z. Huang, F. Cao, Z. Sun, and S. P. Shah, “Effects of nano-silica and nano-limestone on flowability and mechanical properties of ultra-high-performance concrete matrix,” *Constr Build Mater*, vol. 95, pp. 366–374, 2015, doi: 10.1016/j.conbuildmat.2015.05.137.

[103] V. C. Li, S. Wang, and C. Wu, “Tensile strain-hardening behavior or polyvinyl alcohol engineered cementitious composite (PVA-ECC),” *ACI Mater J*, vol. 98, no. 6, pp. 483–492, 2001, doi: 10.14359/10851.

[104] T. Kanda and V. C. Li, “Practical Design Criteria for Saturated Pseudo Strain Hardening Behavior in ECC,” vol. 4, no. 1, pp. 59–72, 2006.

[105] V. C. Li and E. H. Yang, “Self Healing in Concrete Materials,” *Springer Series in Materials Science*, vol. 100, pp. 161–193, 2007, doi: 10.1007/978-1-4020-6250-6_8.

[106] H. Liu, Q. Zhang, C. Gu, H. Su, and V. C. Li, "Influence of micro-cracking on the permeability of engineered cementitious composites," *Cem Concr Compos*, vol. 72, pp. 104–113, 2016, doi: 10.1016/j.cemconcomp.2016.05.016.

[107] X. Huang, R. Ranade, W. Ni, and V. C. Li, "Development of green engineered cementitious composites using iron ore tailings as aggregates," *Constr Build Mater*, vol. 44, pp. 757–764, 2013, doi: 10.1016/j.conbuildmat.2013.03.088.

[108] Y. Y. Kim, H.-J. Kong, and V. C. Li, "Design of Engineered Cementitious Composite Suitable for Wet-Mixture Shotcreting," *ACI Mater J*, vol. 100, no. 6, pp. 511–518, 2003.

[109] M. D. Lepech and V. Li, "Long Term Durability Performance of Engineered Cementitious Composites DURABILITY AND LONG TERM PERFORMANCE OF ENGINEERED," no. May, 2015.

[110] J. Yu, J. Lin, Z. Zhang, and V. C. Li, "Mechanical performance of ECC with high-volume fly ash after sub-elevated temperatures," vol. 99, pp. 82–89, 2015, doi: 10.1016/j.conbuildmat.2015.09.002.

[111] M. O. Connell, C. Mcnally, and M. G. Richardson, "Performance of concrete incorporating GGBS in aggressive wastewater environments," *Constr Build Mater*, vol. 27, no. 1, pp. 368–374, 2012, doi: 10.1016/j.conbuildmat.2011.07.036.

[112] S. U. Al-Dulaijan, M. Maslehuddin, M. M. Al-Zahrani, A. M. Sharif, M. Shameem, and M. Ibrahim, "Sulfate resistance of plain and blended cements exposed to varying concentrations of sodium sulfate," *Cem Concr Compos*, vol. 25, no. 4-5 SPEC, pp. 429–437, 2003, doi: 10.1016/S0958-9465(02)00083-5.

[113] T. U. Mohammed, H. Hamada, and T. Yamaji, "Performance of seawater-mixed concrete in the tidal environment," vol. 34, no. September 2001, pp. 593–601, 2004, doi: 10.1016/j.cemconres.2003.09.020.

[114] H. Liu, Q. Zhang, V. Li, H. Su, and C. Gu, "Durability study on engineered cementitious composites (ECC) under sulfate and chloride environment,"

Constr Build Mater, vol. 133, pp. 171–181, 2017, doi: 10.1016/j.conbuildmat.2016.12.074.

[115] X. Quan *et al.*, “The corrosion resistance of engineered cementitious composite (ECC) containing high-volume fly ash and low-volume bentonite against the combined action of sulfate attack and dry-wet cycles,” *Constr Build Mater*, vol. 303, no. August, p. 124599, 2021, doi: 10.1016/j.conbuildmat.2021.124599.

[116] H. Liu, Q. Zhang, C. Gu, H. Su, and V. Li, “Self-healing of microcracks in Engineered Cementitious Composites under sulfate and chloride environment,” *Constr Build Mater*, vol. 153, pp. 948–956, 2017, doi: 10.1016/j.conbuildmat.2017.07.126.

[117] M. Li and V. C. Li, “Cracking and Healing of Engineered Cemetitious Composites under Chloride Cracking and Healing of Engineered Cementitious Composites under Chloride Environment,” no. October 2012, 2017.

[118] H. Ma, C. Yi, and C. Wu, “Review and outlook on durability of engineered cementitious composite (ECC),” *Constr Build Mater*, vol. 287, p. 122719, 2021, doi: 10.1016/j.conbuildmat.2021.122719.

[119] S. Rawat, C. K. Lee, and Y. X. Zhang, “Performance of fibre-reinforced cementitious composites at elevated temperatures: A review,” *Constr Build Mater*, vol. 292, pp. 0–74, 2021, doi: 10.1016/j.conbuildmat.2021.123382.

[120] M. Şahmaran, E. Özbay, H. E. Yücel, M. Lachemi, and V. C. Li, “Effect of Fly Ash and PVA Fiber on Microstructural Damage and Residual Properties of Engineered Cementitious Composites Exposed to High Temperatures,” *Journal of Materials in Civil Engineering*, vol. 23, no. 12, pp. 1735–1745, 2011, doi: 10.1061/(asce)mt.1943-5533.0000335.

[121] V. Mechtcherine, F. De Andrade, S. Müller, P. Jun, R. Dias, and T. Filho, “Cement and Concrete Research Coupled strain rate and temperature effects on the tensile behavior of strain-hardening cement-based composites (SHCC) with PVA fi bers,” vol. 42, pp. 1417–1427, 2012, doi: 10.1016/j.cemconres.2012.08.011.

[122] S. Pourfalah, “Behaviour of engineered cementitious composites and hybrid engineered cementitious composites at high temperatures,” *Constr Build Mater*, vol. 158, pp. 921–937, 2018, doi: 10.1016/j.conbuildmat.2017.10.077.

[123] J. K. Zhou *et al.*, “Durability assessment of GFRP bars embedded in UHP-ECCs subjected to an accelerated aging environment with sustained loading,” *Constr Build Mater*, vol. 419, no. February, p. 135364, 2024, doi: 10.1016/j.conbuildmat.2024.135364.

[124] J. Tian *et al.*, “Investigation of damage behaviors of ECC-to-concrete interface and damage prediction model under salt freeze-thaw cycles,” *Constr Build Mater*, vol. 226, pp. 238–249, 2019, doi: 10.1016/j.conbuildmat.2019.07.237.

[125] C. Wu, Y. Pan, and T. Ueda, “Characterization of the abrasion resistance and the acoustic wave attenuation of the engineered cementitious composites for runway pavement,” *Constr Build Mater*, vol. 174, pp. 537–546, 2018, doi: 10.1016/j.conbuildmat.2018.04.152.

[126] H. Yun, S. Kim, Y. Lee, and K. Rokugo, “Cold Regions Science and Technology Tensile behavior of synthetic fi ber-reinforced strain-hardening cement-based composite (SHCC) after freezing and thawing exposure,” *Cold Reg Sci Technol*, vol. 67, no. 1–2, pp. 49–57, 2011, doi: 10.1016/j.coldregions.2011.02.002.

[127] F. Li, T. Wen, J. Li, H. Tang, Z. Chen, and H. Wu, “Case Studies in Construction Materials Ultrasonic-detected damage and bending behavior of reinforced PP-ECC beams after coupled action of freeze-thaw cycles and constant flexural load,” *Case Studies in Construction Materials*, vol. 17, no. June, pp. e01284–e01284, 2022, doi: 10.1016/j.cscm.2022.e01284.

[128] M. Şahmaran and V. C. Li, “De-icing salt scaling resistance of mechanically loaded engineered cementitious composites,” *Cem Concr Res*, vol. 37, no. 7, pp. 1035–1046, 2007, doi: 10.1016/j.cemconres.2007.04.001.

[129] Y. Zhu, Y. Yang, and Y. Yao, “Autogenous self-healing of engineered cementitious composites under freeze – thaw cycles,” *Constr Build Mater*, vol. 34, pp. 522–530, 2012, doi: 10.1016/j.conbuildmat.2012.03.001.

[130] N. Zhao, S. Wang, C. Wang, X. Quan, Q. Yan, and B. Li, “Study on the durability of engineered cementitious composites (ECCs) containing high-volume fly ash and bentonite against the combined attack of sulfate and freezing-thawing (F-T),” *Constr Build Mater*, vol. 233, p. 117313, 2020, doi: 10.1016/j.conbuildmat.2019.117313.

[131] R. Oliveira *et al.*, “Assessment of the durability of grout submitted to accelerated carbonation test,” *Constr Build Mater*, vol. 159, pp. 261–268, 2018, doi: 10.1016/j.conbuildmat.2017.10.111.

[132] K. Turk and S. Demirhan, “Effect of limestone powder on the rheological , mechanical and durability properties of ECC,” vol. 8189, no. February, 2016, doi: 10.1080/19648189.2016.1150902.

[133] C. Shi, T. He, G. Zhang, X. Wang, and Y. Hu, “Effects of superplasticizers on carbonation resistance of concrete,” *Constr Build Mater*, vol. 108, pp. 48–55, 2016, doi: 10.1016/j.conbuildmat.2016.01.037.

[134] S. Tsivilis *et al.*, “Cement & Concrete Composites The effect of clinker and limestone quality on the gas permeability , water absorption and pore structure of limestone cement concrete,” vol. 21, pp. 139–146, 1999.

[135] Y. Wang, D. Niu, and Z. Dong, “Experimental study on carbonation of steel fiber reinforced concrete,” *Proceedings of the 4th International Conference on the Durability of Concrete Structures, ICDCS 2014*, no. July, pp. 55–59, 2014, doi: 10.5703/1288284315382.

[136] A. Fibers, “Mechanical Properties and Carbonation Durability of Engineered Cementitious Composites Reinforced by Polypropylene and Hydrophilic Polyvinyl,” 2018, doi: 10.3390/ma11071147.

[137] M. Hou, D. Zhang, and V. C. Li, “Material processing, microstructure, and composite properties of low carbon Engineered Cementitious Composites (ECC),” *Cem Concr Compos*, vol. 134, 2022, doi: 10.1016/j.cemconcomp.2022.104790.

[138] D. Zhang, B. R. Ellis, B. Jaworska, W. H. Hu, and V. C. Li, “Carbonation curing for precast Engineered Cementitious Composites,” *Constr Build Mater*, vol. 313, 2021, doi: 10.1016/j.conbuildmat.2021.125502.

[139] H. Wu, D. Zhang, B. R. Ellis, and V. C. Li, “Development of reactive MgO-based Engineered Cementitious Composite (ECC) through accelerated carbonation curing,” *Constr Build Mater*, vol. 191, pp. 23–31, 2018, doi: 10.1016/j.conbuildmat.2018.09.196.

[140] J. C. Struct, Z. Luo, X. Yang, H. Ji, and C. Zhang, “Carbonation Model and Prediction of Polyvinyl Alcohol Fiber Concrete with Fiber Length and Content Effects,” pp. 1–14, 2022.

[141] L. Cheng, S. Chen, F. Chen, C. Wang, and Q. Chen, “Research Progress and Performance Evaluation of Polyvinyl Alcohol Fiber Engineered Cementitious Composites,” *Sustainability (Switzerland)*, vol. 15, no. 14, 2023, doi: 10.3390/su151410991.

[142] S. R. Shiradhonkar, R. Sinha, and M. Asce, “Maximum and Residual Flexural Crack Width Estimation in Reinforced Concrete Frame Members under Seismic Excitation,” vol. 144, no. 8, pp. 1–12, 2018, doi: 10.1061/(ASCE)ST.1943-541X.0002116.

[143] Z. Zhang and Q. Zhang, “Matrix tailoring of Engineered Cementitious Composites (ECC) with non-oil-coated, low tensile strength PVA fiber,” *Constr Build Mater*, vol. 161, pp. 420–431, 2018, doi: 10.1016/j.conbuildmat.2017.11.072.

[144] H. Reinhardt and M. Jooss, “Permeability and self-healing of cracked concrete as a function of temperature and crack width,” vol. 33, pp. 981–985, 2003, doi: 10.1016/S0008-8846(02)01099-2.

[145] H. Liu, Q. Zhang, C. Gu, H. Su, and V. Li, “Influence of microcrack self-healing behavior on the permeability of Engineered Cementitious Composites,” *Cem Concr Compos*, 2017, doi: 10.1016/j.cemconcomp.2017.04.004.

[146] X. Huang, R. Ranade, Q. Zhang, W. Ni, and V. C. Li, “Mechanical and thermal properties of green lightweight engineered cementitious composites,” vol. 48, pp. 954–960, 2013, doi: 10.1016/j.conbuildmat.2013.07.104.

[147] S. R. Abid, M. S. Shamkhi, N. S. Mahdi, and Y. H. Daek, “Hydro-abrasive resistance of engineered cementitious composites with PP and PVA fibers,” *Constr Build Mater*, vol. 187, pp. 168–177, 2018, doi: 10.1016/j.conbuildmat.2018.07.194.

[148] S. R. Abid, A. N. Hilo, and Y. H. Daek, “Experimental tests on the underwater abrasion of Engineered Cementitious Composites,” *Constr Build Mater*, vol. 171, pp. 779–792, 2018, doi: 10.1016/j.conbuildmat.2018.03.213.

[149] E. Desta, W. Li, G. Fang, Z. Wang, and J. Liu, “Case Studies in Construction Materials Review on the durability of eco-friendly engineering cementitious composite (ECC),” *Case Studies in Construction Materials*, vol. 19, no. July, pp. e02324–e02324, 2023, doi: 10.1016/j.cscm.2023.e02324.

[150] T. Huang, Y. X. Zhang, S. R. Lo, and C. K. Lee, “Experimental study on crack bridging in engineered cementitious composites under fatigue tensile loading,” vol. 154, pp. 167–175, 2017, doi: 10.1016/j.conbuildmat.2017.07.193.

[151] A. Clay *et al.*, “Case Studies in Construction Materials Fatigue behavior of steel fiber reinforced geopolymer concrete Ver o,” vol. 16, no. November 2021, pp. 0–8, 2022, doi: 10.1016/j.cscm.2021.e00829.

[152] V. Scarpini, A. Clay, N. Tonini, E. Sousa, F. Santos, and S. Neves, “Mechanical and microstructural characterization of geopolymeric concrete subjected to fatigue ଝ,” *Integr Med Res*, vol. 7, no. 4, pp. 566–570, 2018, doi: 10.1016/j.jmrt.2018.07.011.

[153] H. Wang, Y. Wu, M. Wei, L. Wang, and B. Cheng, “Hysteretic Behavior of Geopolymer Concrete with Active Confinement Subjected to Monotonic and Cyclic Axial Compression : An Experimental Study”.

[154] L. Liu, S. Gao, J. Xin, and D. Huang, “Effect of Low-Stress Fatigue on the Off-Crack-Plane Fracture Energy in Engineered Cementitious Composites,” vol. 2018, 2018.

[155] U. Reinforced *et al.*, “Flexural Fatigue Properties of Ultra-High Performance Engineered Cementitious Composites,” 2018, doi: 10.3390/polym10080892.

[156] J. Qiu, W. L. Aw-Yong, and E. H. Yang, “Effect of self-healing on fatigue of engineered cementitious composites (ECCs),” *Cem Concr Compos*, vol. 94, pp. 145–152, 2018, doi: 10.1016/j.cemconcomp.2018.09.007.

[157] T. Huang and Y. X. Zhang, “Numerical modelling on degradation of mechanical behaviour for engineered cementitious composites under fatigue tensile loading,” *Eng Fract Mech*, 2017, doi: 10.1016/j.engfracmech.2017.08.036.

[158] W. Liu, S. Xu, and P. Feng, “Fatigue damage propagation models for ductile fracture of ultrahigh toughness cementitious composites,” vol. 0, no. 0, pp. 1–14, 2016, doi: 10.1177/1056789516635727.

[159] P. Suthiwarapirak, T. Matsumoto, and T. Kanda, “Multiple Cracking and Fiber Bridging Characteristics of Engineered Cementitious Composites under Fatigue Flexure,” vol. 16, no. 5, pp. 433–443, 2005.

[160] A. Mansoori, “Evaluation of the effects of nanomaterials on durability of engineered cementitious composites exposed to the aggressive environment,” 2019, doi: 10.1177/0021998319887208.

[161] H. Wu, D. Zhang, Y. Du, and V. C. Li, “Durability of engineered cementitious composite exposed to acid mine drainage,” *Cem Concr Compos*, vol. 108, no. January, p. 103550, 2020, doi: 10.1016/j.cemconcomp.2020.103550.

[162] T. Paper, “SULFURIC ACID RESISTANCE OF STRAIN HARDENING FIBER REINFORCED GEOPOLYMER,” no. December, pp. 47–53, 2019.

[163] J. Zhang, Y. Gao, and Z. Wang, “Composites : Part B Evaluation of shrinkage induced cracking performance of low shrinkage engineered cementitious

composite by ring tests," *Composites Part B*, vol. 52, pp. 21–29, 2013, doi: 10.1016/j.compositesb.2013.03.012.

[164] T. Kanda, S. Nagai, and M. Maruta, "Experimental investigation for ECC improving shrinkage crack resistance and workability," *Fracture Mechanics of Concrete and Concrete Structures*, pp. 1600–1604, 2010.

[165] B. Ye, Y. Zhang, J. Han, and P. Pan, "Effect of water to binder ratio and sand to binder ratio on shrinkage and mechanical properties of High-strength Engineered Cementitious Composite," vol. 226, pp. 899–909, 2019, doi: 10.1016/j.conbuildmat.2019.07.303.

[166] M. Şahmaran, Z. Bilici, E. Ozbay, T. K. Erdem, H. E. Yucel, and M. Lachemi, "Improving the workability and rheological properties of Engineered Cementitious Composites using factorial experimental design," *Compos B Eng*, vol. 45, no. 1, pp. 356–368, 2013, doi: 10.1016/j.compositesb.2012.08.015.

[167] S. Gao, Z. Wang, W. Wang, and H. Qiu, "Effect of shrinkage-reducing admixture and expansive agent on mechanical properties and drying shrinkage of Engineered Cementitious Composite (ECC)," *Constr Build Mater*, vol. 179, pp. 172–185, 2018, doi: 10.1016/j.conbuildmat.2018.05.203.

[168] E. H. Yang, Y. Yang, and V. C. Li, "Use of high volumes of fly ash to improve ECC mechanical properties and material greenness," *ACI Mater J*, vol. 104, no. 6, pp. 620–628, 2007, doi: 10.14359/18966.

[169] K. Kobayashi, T. Iizuka, H. Kurachi, and K. Rokugo, "Corrosion protection performance of High Performance Fiber Reinforced Cement Composites as a repair material," *Cem Concr Compos*, vol. 32, no. 6, pp. 411–420, 2010, doi: 10.1016/j.cemconcomp.2010.03.005.

[170] M. Sahmaran, V. C. Li, and C. Andrade, "Corrosion Resistance Performance of Steel-Reinforced Engineered Cementitious Composite Beams," no. 105, pp. 243–250, 2009.

[171] G. Fischer and V. C. Li, "Deformation behavior of fiber-reinforced polymer reinforced engineered cementitious composite (ECC) flexural members under

reversed cyclic loading conditions," *ACI Struct J*, vol. 100, no. 1, pp. 25–35, 2003, doi: 10.14359/12436.

[172] J. Zhang and V. C. Li, "Monotonic and fatigue performance in bending of fiber-reinforced engineered cementitious composite in overlay system," *Cem Concr Res*, vol. 32, no. 3, pp. 415–423, 2002, doi: 10.1016/S0008-8846(01)00695-0.

[173] E. H. Yang and V. C. Li, "Tailoring engineered cementitious composites for impact resistance," *Cem Concr Res*, vol. 42, no. 8, pp. 1066–1071, 2012, doi: 10.1016/j.cemconres.2012.04.006.

[174] S. Miyazato and Y. Hiraishi, "Transport properties and steel corrosion in Ductile Fiber Reinforced Cement Composites," *11th International Conference on Fracture 2005, ICF11*, vol. 2, no. April, pp. 1500–1505, 2005.

[175] Z. Zhang, S. Qian, and H. Ma, "Investigating mechanical properties and self-healing behavior of micro-cracked ECC with different volume of fly ash," *Constr Build Mater*, vol. 52, pp. 17–23, 2014, doi: 10.1016/j.conbuildmat.2013.11.001.

[176] G. C. Cordeiro, L. M. Tavares, and R. D. Toledo Filho, "Improved pozzolanic activity of sugar cane bagasse ash by selective grinding and classification," *Cem Concr Res*, vol. 89, pp. 269–275, Nov. 2016, doi: 10.1016/j.cemconres.2016.08.020.

[177] L.-Y. Xu, B.-T. Huang, J.-C. Lao, and J.-G. Dai, "Tailoring strain-hardening behavior of high-strength Engineered Cementitious Composites (ECC) using hybrid silica sand and artificial geopolymer aggregates," *Mater Des*, vol. 220, p. 110876, 2022, doi: 10.1016/j.matdes.2022.110876.

[178] Q. Wang, M. H. Lai, J. Zhang, Z. Wang, and J. C. M. Ho, "Greener engineered cementitious composite (ECC) – The use of pozzolanic fillers and unoiled PVA fibers," *Constr Build Mater*, vol. 247, 2020, doi: 10.1016/j.conbuildmat.2020.118211.

[179] L. Y. Xu, B. T. Huang, and J. G. Dai, “Development of engineered cementitious composites (ECC) using artificial fine aggregates,” *Constr Build Mater*, vol. 305, no. September, p. 124742, 2021, doi: 10.1016/j.conbuildmat.2021.124742.

[180] M. Singh, B. Saini, and H. D. Chalak, “Durability and Ecological Performance of Hybrid Engineered Cementitious Composite Containing Stone Industry Waste,” *Journal of The Institution of Engineers (India): Series A*, vol. 103, no. 3, pp. 747–765, 2022, doi: 10.1007/s40030-022-00658-w.

[181] V. C. Li, *Mechanical Properties of Engineered Cementitious Composites (ECC)*. 2019. doi: 10.1007/978-3-662-58438-5_4.

[182] M. A. Kewalramani, O. A. Mohamed, and Z. I. Syed, “Engineered Cementitious Composites for Modern Civil Engineering Structures in Hot Arid Coastal Climatic Conditions,” *Procedia Eng*, vol. 180, pp. 767–774, 2017, doi: 10.1016/j.proeng.2017.04.237.

ANNEXURE A

TRIAL MIXES DETIALS

A.1 Introduction

This annexure documents the detailed experimental procedure adopted for developing and optimizing Engineered Cementitious Composite (ECC) mixtures used in this research. The mix proportions used in the present study were finalized through a systematic trial-and-error approach aimed at achieving the desired fresh and hardened properties of the composite. The mix design was not based on any codal provisions, as no standard guidelines are available for proportioning such cementitious composite materials. Based on an extensive literature survey, the most commonly reported proportions of the constituent materials were adopted as the initial mix proportions. These proportions were subsequently optimized through experimental trials based on flowability and mechanical performance.

A.2 Mix Optimization

The ECC mix proportioning in this study was carried out using a systematic and convergence-based approach. Parameters governing fresh-state behavior were optimized prior to those influencing hardened-state performance.

Initially, the water-to-binder ratio (w/b) and superplasticizer-to-binder ratio (SP/b) were varied, as these parameters primarily control flowability, mixing stability, and fiber dispersion. Higher w/b ratios were explored in the initial trials to ensure homogeneous mixing, after which the w/b ratio was gradually reduced while adjusting SP/b to maintain adequate flowability. Once stable and repeatable flowability was achieved, the optimum w/b and SP/b ratios were fixed.

Subsequently, the sand-to-binder ratio (s/b) and the content of supplementary cementitious materials were varied to optimize compressive strength and direct tensile performance, while preserving the previously established fresh-state characteristics. Additional confirmatory trials were conducted near the optimum region to ensure consistency. The final ECC mix proportions were selected based on convergence and repeatability rather than a predetermined number of trials.

A.3 ECC Incorporating Fly Ash (FA-ECC)

Initial trials were conducted using higher w/b ratios to ensure ease of mixing and uniform fiber dispersion. The SP/b ratio was varied first to establish a dosage that provided adequate flow without bleeding or segregation. Subsequently, the w/b ratio was gradually reduced while maintaining the selected SP/b ratio.

A total of 18 trial mixes, as listen in Table A.1, were required to reach convergence for FA-ECC. Based on flowability observations, SP/b = 0.01 and w/b = 0.27 were identified as optimum. Thereafter, the sand-to-binder ratio (s/b) and fly ash content were adjusted to optimize compressive strength and direct tensile behavior.

Table A. 1: Preliminary Trial Mixes for FA-ECC

Trail ID	**w/b**	**s/b**	**SP/b (%)**	**PC (Kg/m^3)**	**FA (Kg/m^3)**	**RS (Kg/m^3)**	**PVA (Kg/m^3)**	**Water (Kg/m^3)**	**SP (Kg/m^3)**
T1	0.32	0.35	0.004	480	492	347	26	318	3.97
T2	0.32	0.35	0.006	480	492	347	26	318	5.95
T3	0.32	0.35	0.008	480	512	347	26	318	7.94
T4	0.30	0.35	0.008	480	512	347	26	298	7.94
T5	0.30	0.35	0.010	480	512	347	26	298	9.92
T6	0.29	0.35	0.010	480	512	347	26	288	9.92
T7	0.28	0.35	0.010	480	512	347	26	278	9.92
T8	0.27	0.35	0.010	480	512	347	26	268	9.92
T9	0.26	0.35	0.010	480	512	347	26	258	9.92
T10	0.27	0.30	0.010	480	512	298	26	268	9.92
T11	0.27	0.35	0.010	480	512	347	26	268	9.92
T12	0.27	0.38	0.010	480	512	377	26	268	9.92
T13	0.27	0.40	0.010	480	512	405	26	268	9.92
T14	0.27	0.42	0.010	480	512	426	26	268	9.92
T15	0.27	0.45	0.010	480	512	446	26	268	9.92
T16	0.27	0.40	0.010	500	512	405	26	268	9.92
T17	**0.27**	**0.40**	**0.010**	**480**	**512**	**405**	**26**	**268**	**9.92**
T18	0.27	0.40	0.010	480	512	405	26	268	9.92

A.4 ECC Incorporating Sugarcane Bagasse Ash (SCBA-ECC)

A total of 19 trial mixes were required to achieve convergence for SCBA-ECC. ECC mixes incorporating SCBA exhibited higher water demand and required increased superplasticizer dosage. Therefore, SP/b was optimized at higher levels compared to FA-ECC. Flowability was first stabilized by varying SP/b and w/b ratios, after which sand-to-binder ratio and SCBA content were adjusted to improve mechanical performance.

Table A. 2 Preliminary Trial Mixes for SCBA-ECC

Trail ID	**w/b**	**s/b**	**SP/b (%)**	**PC (Kg/m^3)**	**FA (Kg/m^3)**	**RS (Kg/m^3)**	**PVA (Kg/m^3)**	**Water (Kg/m^3)**	**SP (Kg/m^3)**
S1	0.34	0.55	0.008	480	180	370	26	224	5.26
S2	0.34	0.55	0.012	480	180	370	26	224	7.88
S3	0.34	0.55	0.016	480	180	370	26	224	10.50
S4	0.32	0.55	0.016	480	180	370	26	211	10.50
S5	0.31	0.55	0.018	480	180	370	26	204	11.81
S6	0.30	0.55	0.020	480	180	370	26	198	13.13
S7	0.29	0.55	0.020	480	180	370	26	191	13.13
S8	0.29	0.50	0.020	480	180	335	26	191	13.13
S9	0.29	0.55	0.020	480	180	370	26	191	13.13
S10	0.29	0.58	0.020	480	180	389	26	191	13.13
S11	0.29	0.60	0.020	480	180	405	26	191	13.13
S12	0.29	0.62	0.020	480	180	419	26	191	13.13
S13	0.29	0.65	0.020	480	180	439	26	191	13.13
S14	0.29	0.60	0.020	500	160	405	26	191	13.13
S15	0.29	0.60	0.020	480	194	405	26	195	13.48
S16	0.29	0.60	0.020	460	214	405	26	195	13.48
S17	0.29	0.60	0.020	470	204	405	26	195	13.48
S18	0.29	0.60	0.020	480	194	405	26	195	13.48
S19	**0.29**	**0.60**	**0.020**	**480**	**194**	**405**	**26**	**195**	**13.48**

Prior to finalizing the ECC mix proportions, target strength levels were defined to guide the mix optimization process. For FA-ECC, the mix design was aimed at achieving a compressive strength of approximately 35 MPa and a direct tensile strength of about 4.0 MPa while maintaining stable flowability and uniform fiber dispersion. For SCBA-

ECC, comparatively lower target strengths were set in recognition of the material characteristics of sugarcane bagasse ash, with the design objective being a compressive strength of approximately 27 MPa and a direct tensile strength of about 3.0 MPa. These target values served as performance benchmarks during the trial phase and informed the selection of the final control mixes.

Table A.3 summarizes the flowability classification and preliminary mechanical performance of FA-ECC trial mixes, with strength results reported only for mixes exhibiting moderate to good flowability.

Table A. 3 Flowability and Mechanical Performance of FA-ECC Trial Mixes

Trial ID	Flowability	Compressive Strength (MPa)	Direct Tensile Strength (MPa)
T1	Very Low	–	–
T2	Low	–	–
T3	Moderate	30.2	3.10
T4	Moderate	31.4	3.25
T5	Good	32.6	3.42
T6	Good	33.1	3.55
T7	Good	34.0	3.70
T8	Good	34.8	3.85
T9	Low	–	–
T10	Moderate	31.9	3.20
T11	Good	34.5	3.90
T12	Good	35.6	4.00
T13	Good	36.2	4.10
T14	Moderate	34.9	3.95
T15	Low	–	–
T16	Good	36.0	4.05
T17	Good	36.47	4.15
T18	Good	36.3	4.12

Table A.4 presents the flowability assessment and preliminary mechanical performance of SCBA-ECC trial mixes, while mixes with very low or low flowability were excluded from mechanical evaluation.

Table A. 4 Flowability and Mechanical Performance of SCBA-ECC Trial Mixes

Trial ID	Flowability	Compressive Strength (MPa)	Direct Tensile Strength (MPa)
S1	Very Low	–	–
S2	Low	–	–
S3	Moderate	22.8	2.40
S4	Moderate	23.6	2.55
S5	Good	24.8	2.70
S6	Good	25.9	2.85
S7	Good	26.4	2.95
S8	Moderate	25.2	2.80
S9	Good	26.8	3.00
S10	Good	27.3	3.05
S11	Good	27.8	3.08
S12	Moderate	26.6	2.95
S13	Low	–	–
S14	Moderate	26.9	3.00
S15	Good	28.0	3.10
S16	Good	27.6	3.05
S17	Good	27.9	3.08
S18	Good	28.1	3.12
S19	Good	28.0	3.11

The final selected trial mixes, identified based on optimum flowability and mechanical performance, were adopted as the control ECC mixtures for all subsequent experimental investigations are shown in Table A.5 and Table A.6.

Table A. 5 Control design mix with FA as SCM

Trail ID	w/b	s/b	SP/b (%)	PC (Kg/m^3)	FA (Kg/m^3)	RS (Kg/m^3)	PVA (Kg/m^3)	Water (Kg/m^3)	SP (Kg/m^3)
T17	0.27	0.40	0.01	480	512	405	26	268	9.92

Table A. 6 Control design mix with SCBA as SCM

Trail ID	w/b	s/b	SP/b (%)	PC (Kg/m^3)	SCBA (Kg/m^3)	RS (Kg/m^3)	PVA (Kg/m^3)	Water (Kg/m^3)	SP (Kg/m^3)
S19	0.29	0.60	0.02	480	194	405	26	195	13.48